CFD investigation on inlet flow distortion in a centrifugal compressor

Eidgenössische Technische Hochschule Zürich
Swiss Federal Institute of Technology Zurich

Labor für Strömungsmaschinen
Turbomachinery Laboratory

Swiss Federal Institute of Technology, ETH, Zurich

Turbomachinery Laboratory

Prof. Dr. R. S. Abhari

CFD Investigation on

Inlet Flow Distortion in a Centrifugal Compressor

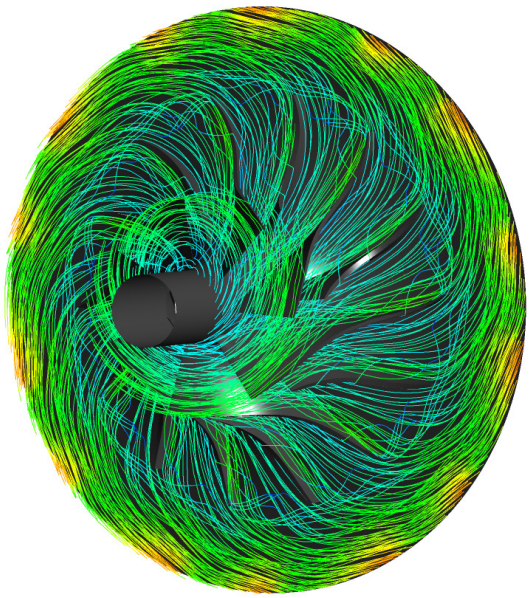

Master's Thesis 06/07
Armin Zemp

Supervisor:
Dipl. Ing. Albert Kammerer

I. Proposal

In turbomachinery, rotating components are subject to vibration. This in particular applies to rotating blades with vibration being one of the main contributors to failure during operation. Blade vibration is caused by a complex interaction between the fluid and the structure. Forced response originates from unsteady fluid structures as conditioned at compressor inlet by pipe bendings, struts or inlet guide vanes. With respect to this the proposed project addresses the problem of flow distortion at compressor inlet.
The centrifugal compressor test facility RIGI at LSM is modified such that blade vibration measurements with strain gauges can be carried out. Major requirements of the test facility encompass the utilization of a suitable inlet flow distortion mechanism with the capability to generate specific flow patterns. This depends on the design of distortion elements used and their installation upstream of the impeller.

According to the described problem the master project addresses the following problems:

1. Simulation and validation of the CFD model on the basis of steady state computational fluid dynamics

2. Implementation of the FRAP- measured inlet flow field with different distortion patterns as inlet boundary condition for the computational model

3. Qualitative description of flow patterns within the impeller

4. Time resolved CFD to get unsteady pressure distribution on impeller blades

Supervisor and Contact:

Dipl. Ing. Albert Kammerer
Institut für Energietechnik
Labor für Strömungsmaschinen
ETH Zentrum, ML J32
Sonneggstrasse 3
CH- 8092 Zürich
Phone: 044/632 26 94
Email: kammerer@lsm.iet.mavt.ethz.ch

II. Abstract

In turbomachinery rotating components are subject to vibration. This in particular applies to rotating blades being one of the main contributors to failure during operation. Forced response of the blades originates from unsteady fluid structures as conditioned in the inlet section by duct bends, struts or inlet guide vanes. Most of the pressure- increasing turbomachines in use are of the radial flow type. The development of turbomachines using centrifugal effects for increasing fluid pressure have been in use for more than a century. The development of centrifugal compressors continued into the 1950's. The enquiry for advanced military helicopters powered by small gas turbine engines in the 1960's caused a rapid development of the centrifugal compressor. In industry especially in automotive applications the inlet section due to the reduced amount of space contains often bends. These bent ducts create a non- uniform inlet flow field entering the impeller eye of a centrifugal compressor. Such non- uniformities may have disadvantageous effects on impeller performance and can excite the impeller blades. Cumpsty (Cumpsty, 2004) presents an investigation of a multistage axial compressor and remarked that the performance can be seriously affected by inlet distortion. The turbomachinery laboratory of ETH Zurich runs a centrifugal compressor test rig. To create inlet distortion in the compressor rig screens with metal grid baffles are installed in the inlet section. Different baffle geometries and grids of variable porosities are used to generate different distortion patterns. The amplitude of the distortion is controlled by the porosity of the applied grids. To quantify the flow properties entering the impeller eye the data acquisition in the inlet flow field is done with the so called fast response aerodynamic probe (FRAP) measurement technique. An extended traversing system allows to move the probe in a plane perpendicular to the main flow direction. The measured inlet flow field is applied as inlet boundary condition for the numerical investigation of the centrifugal compressor.

A detailed validation of the CFD model on the base of steady state computations over the entire compressor map showed good consistence with the test rig performance. The qualitative description of the flow patterns within the impeller provides information about the fluid dynamics taking place for several operating points. A main focus lies on the development of the shroud gap vortex. The investigation shows the trend to increased total pressure loss due to the tip leakage vortex with increased mass flow rate at constant blade speed. In contrast the total pressure loss due to the tip leakage vortex in the inter blade channel decreases with increased impeller speed at constant mass flow rate due to the fact that the amount of main blade leakage flow passing in front of the splitter blade leading edge increases. The time resolved CFD investigation provides information about the unsteady pressure distribution on the main blade surface. The spectral analysis of the time resolved blade pressure distribution at several operating points with different distortion screen geometries shows the temporal evolution of the dynamic load on the blade caused by the inlet distortion. The transformation of the unsteady blade pressure into the frequency domain provides information about the frequency and the amplitude of the excitation over the whole blade surface. The comparison of different inlet boundary conditions such as turbulence intensity profile measured with FRAP probes versus constant turbulence intensity level, or idealized total pressure profile at the inlet of the CFD model versus measured total pressure profile containing all rudiments of upstream installations (struts for the slip ring support for example), shows the insensitivity of the model concerning the unsteady pressure distribution on the main blade surface.

III. Acknowledgement

I would like to thank Prof. Dr. R. S. Abhari for the possibility to make the present work at Turbomachinery Laboratory at ETH Zurich. The present work is part of real research of Mr. Kammerers Ph.D.- Thesis at the institute and allowed to have a detailed insight in current research activities at the Turbomachinery Laboratory. The master's thesis together with the foregoing semester thesis caused great fascination for centrifugal compressors.

I also would like to express my sincere thanks to my supervisor Dipl. Ing. Albert Kammerer. His exemplary way of assistance and his friendly nature were the base to render possible such a salutary time at the institute. His expert knowledge in the centrifugal compressor area and his cooperativeness combined with a scientific way of solving disparate problems allowed me to learn a lot not only on radial compressors but also on scientific methodology.

IV. Table of Contents

1. Introduction

1.1 General Background

The centrifugal or radial compressor finds the most widespread use of any compressor type. At one extreme there are machines producing pressure ratios of more than 8:1 from one stage. These impellers used for aviation appliances have titanium alloy impellers. At the other end of the range there are very low cost devices in domestic appliances fabricated out of sheet metal where the overriding concern is to keep the cost low. Research and development activity has concentrated on those areas where the performance is high.

1.2 Centrifugal Compressors

The development of turbomachines using centrifugal effects for increasing fluid pressure have been in use for more than a century. The earliest machines using this principle were hydraulic pumps, followed later by ventilating fans and blowers.

The development of centrifugal compressors continued into the 1950's but it had become clear that for the larger engines required for aircraft propulsion the axial flow compressor was preferred. Not only due to the smaller frontal area (and therefore smaller drag) needed for an axial flow compressor but also due to the higher efficiency for the same duty (about 3% to 4%). But at very low air mass flow rates the efficiency of axial compressors drops dramatically. The blading is small and difficult to fabricate. Especially the narrow range of tolerance in such small machines is difficult to keep.

The enquiry for advanced military helicopters powered by small gas turbine engines in the 1960's caused a rapid development of the centrifugal compressor.

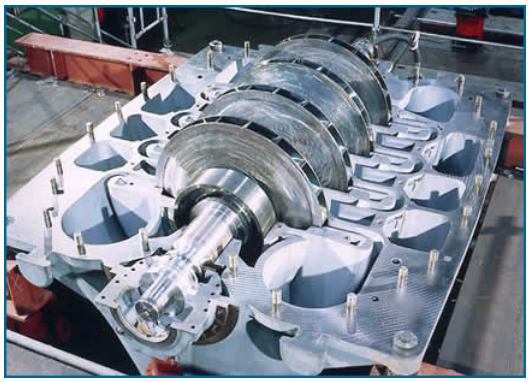

Fig. 1.2.0.1: Multi Stage Centrifugal Compressor (ABB)

1.3 Internal Flows

It is often the fluid motion which set the performance of devices such as propulsion systems and their components, fluid machinery, ducts and channels. There are often large changes in direction and in velocity. For example, deflections of over 90° are common in fluid machinery. Deflection of the non- uniform flows might create three dimensional motions normal to the mean flow direction. Additionally, there is often strong swirl, with consequent phenomena that are different than for flow without swirl. For example, static pressure rise can be associated almost entirely with the circumferential swirl velocity component. The motions are often unsteady. Unsteadiness is necessary for work exchange in turbomachines. Waves, oscillations and self- excited unsteadiness not only affect system behavior, but can sometimes be a limiting factor for operational regimes.

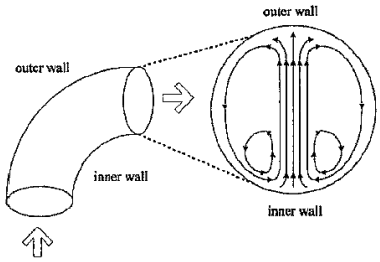

Fig. 1.3.0.1: Flow Field after 90° Bend (Engeda et al., 2003)

2. Objectives and Approach

2.1 Objectives

The present work focuses on inlet flow distortion in centrifugal compressors. The excitation of the impeller blades due to the harmonic load generated by the inlet distortion in the flow in front of the impeller blades is subject of research and part of Mr. Albert Kammerers PhD- Thesis. The present work contains the numerical simulation of the centrifugal impeller and the tracking of the distortion convecting through the compressor. The FRAP measurement results of the foregoing semester thesis are used as boundary condition at the inlet of the computational domain.
A main focus lies on the unsteady pressure distribution on the main blade surface due to the fact that the distortion convecting through the device may excite the impeller blades if the excitation is in resonance with the blades.

2.2 Approach

A series of steady state computations at operating points over the whole compressor map allow a detailed validation of the performance of the numerical model. In a second step unsteady CFD simulations provide time resolved results of the distortion convecting through the impeller. The unsteady pressure distribution on the surface of the blades is used for a spectral analysis.

3. Theoretical Background

3.1 Definitions

Most of the pressure- increasing turbomachines in use are of the radial- flow type and vary from fans that produce pressure rises equivalent to a few millimeters of water to pumps producing heads of many hundreds of metres of water. The term pump is used when referring to machines that increase the pressure of a flowing liquid. The term fan is used for machines imparting only a small increase in pressure to a flowing gas. In this case the pressure rise is usually so small that the gas can be considered as being incompressible.

A compressor gives a substantial rise in pressure to a flowing gas. For purposes of definitions, the boundary between fans and compressors is often taken as that where the density ratio across the machine is 1.05. Sometimes, but more rarely, the term blower is used instead of fan.

A centrifugal compressor or pump consists essentially of a rotating impeller followed by a diffuser. Figure 3.1.0.1 shows the various elements of a centrifugal compressor. Fluid is drawn in through the inlet casing into the eye of the impeller. The function of the impeller is to increase the energy level of the fluid by whirling it outwards, thereby increasing the angular momentum of the fluid. Both the static pressure and the velocity are increased within the impeller. The purpose of the diffuser is to convert the kinetic energy of the fluid leaving the impeller into pressure energy. This process can be accomplished by free diffusion in the annular space surrounding the impeller or by incorporating a row of fixed diffuser vanes which allows the diffuser to be made very much smaller.

Outside the diffuser is a scroll or volute whose function is to collect the flow from the diffuser and deliver it to the outlet pipe. In low- speed compressors and pump applications where simplicity and low cost count for more than efficiency, the volute follows immediately after the impeller.

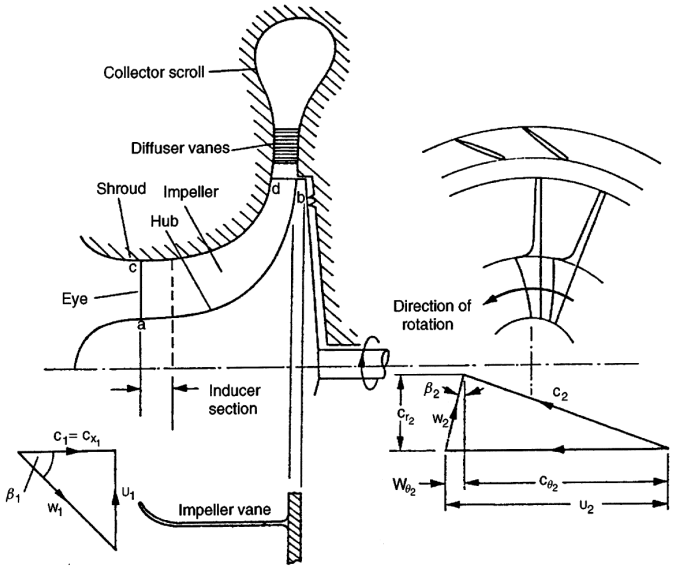

Fig. 3.1.0.1 Centrifugal Compressor Stage (Dixon, 1998)

3.2 Non- dimensional Parameters

With the assumption of a polytropic process, $\frac{vdp}{dh} = const$, and neglecting inlet guide vanes, return channel or scroll the following parameters are used tho characterize a centrifugal compressor system:

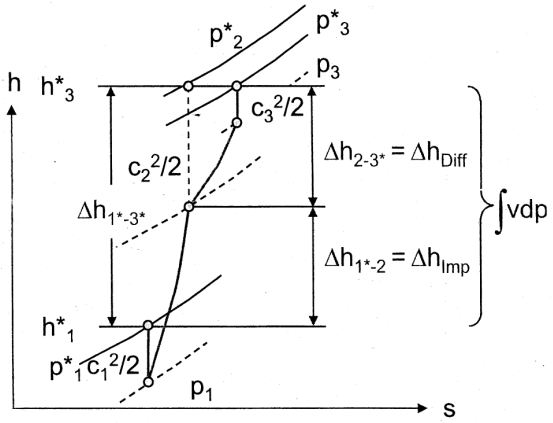

Fig. 3.2.0.1 Enthalpy- Entropy Diagram (Abhari, WS 05/06)

3.2.1 Work Input Coefficient

$$\lambda = \frac{\frac{P}{\dot{m}}}{u_2^2} = \frac{\Delta h_{01-03}}{u_2^2} = \frac{\Delta h_0}{u_2^2}$$

Equation 3.2.1.1

3.2.2 Polytropic Head Coefficient

$$\psi_p = \frac{\int_{01}^{03} vdp}{u_2^2}$$

Equation 3.2.2.1

with $\int_{01}^{03} vdp = RT_{01}\left(\frac{n}{n-1}\right)\left\{\left(\frac{p_{03}}{p_{01}}\right)^{\left(\frac{n-1}{n}\right)} - 1\right\}$ and $\left(\frac{n-1}{n}\right) = \frac{\ln\left(\frac{p_{03}}{p_{01}}\right)}{\ln\left(\frac{T_{03}}{T_{01}}\right)}$

3.2.3 Polytropic Efficiency

$$\eta_p = \frac{\int_{01}^{03} vdp}{\Delta h_{01-03}} = \frac{\psi_p}{\lambda} = \frac{\kappa - 1}{\kappa}\frac{\ln\left(\frac{p_{03}}{p_{01}}\right)}{\ln\left(\frac{T_{03}}{T_{01}}\right)}$$

Equation 3.2.3.1

3.2.4 Flow Coefficient

$$\varphi = \frac{\dot{m}}{\rho_{01} D_2^2 u_2 \frac{\pi}{4}} = \frac{\dot{V}}{D_2^2 u_2 \frac{\pi}{4}}$$

Equation 3.2.4.1

3.2.5 Mach Number

$$Ma = \frac{w}{a} = \frac{w_{local}}{\sqrt{\kappa R T_{local}}}$$

Equation 3.2.5.1

This is the most useful aerodynamic parameter in compressible flows. It is named after the nineteenth- century austrian physicist Ernst Mach but was first used by Professor Ackeret at the ETH Zurich.

3.2.6 Stage Mach Number

$$Mu_2 = \frac{u_2}{a_2} = \frac{u_2}{\sqrt{\kappa R T_{01}}}$$

Equation 3.2.6.1

This definition is used as a non- dimensional speed. Values above 1 do not imply that the flow is choked! The significance of the stage Mach number can best be appreciated in combination with the definition of the work input coefficient assuming a perfect gas:

$$\Delta h_0 = \lambda u_2^2 = c_p (T_{03} - T_{01}) \qquad \rightarrow \frac{T_{03}}{T_{01}} = 1 + \frac{\lambda u_2^2}{c_p T_{01}}$$

Equation 3.2.6.2

with $c_p = \frac{\kappa}{\kappa - 1} R$ and $a_1 = \sqrt{\kappa R T_{01}}$. The temperature ratio is $\frac{T_{03}}{T_{01}} = 1 + (\kappa - 1)\lambda Mu_2^2$ and the pressure ratio is $\pi_0 = \frac{p_{03}}{p_{01}} = \{1 + (\kappa - 1)\lambda Mu_2^2\}^{\eta_p \frac{\kappa}{\kappa - 1}}$ with $\frac{n}{n-1} = \eta_p \frac{\kappa}{\kappa - 1}$. The stage Mach number is therefore a useful non- dimensional parameter that relates the work input coefficient to the pressure and temperature rise across the stage.

3.2.7 Turbine Euler Equation

With the Turbine Euler Equation the work input coefficient can be given as a function of velocity components:

$$\Delta h_0 = u_2 c_{\Theta 2} - u_1 c_{\Theta 1}$$

Equation 3.2.7.1

and with $c_{\Theta 1} = 0$ (no inlet swirl)

$$\lambda = \frac{\Delta h_0}{u_2^2} = \frac{u_2 c_{\Theta 2} - u_1 c_{\Theta 1}}{u_2^2} = \frac{c_{\Theta 2}}{u_2}$$

Equation 3.2.7.2

An alternative form of the Euler equation sheds considerable light on the power and the pressure rise in a compressor stage:

$$c_{r2}^2 = c_2^2 - c_{\Theta 2}^2 = w_2^2 - (u_2 - c_{\Theta 2})^2 \qquad \rightarrow u_2 c_{\Theta 2} = \frac{1}{2}(c_2^2 + u_2^2 - w_2^2)$$

Equation 3.2.7.3

Then the Euler equation can also be expressed as:

$$\Delta h_0 = u_2 c_{\Theta 2} - u_1 c_{\Theta 1} = \frac{1}{2}(c_2^2 + u_2^2 - w_2^2) - \frac{1}{2}(c_1^2 + u_1^2 - w_1^2)$$

Equation 3.2.7.4

or

$$\Delta h_0 = \frac{u_2^2 - u_1^2}{2} - \frac{w_2^2 - w_1^2}{2} + \frac{c_2^2 - c_1^2}{2}$$

Equation 3.2.7.5

In a typical radial compressor stage the centrifugal effect accounts for about one half of the work input. Since the centrifugal effect is free of losses radial stages have higher pressure rise than axial ones and still attain relatively high efficiencies despite their very complicated flow paths. The second term in the equation addresses the diffusion in the impeller. This effect accounts for about 20% of the work input. The last term in the equation shows the diffusion in the non rotating part and accounts for about 30% of the work input.

3.3 Theoretical Analysis of a Centrifugal Compressor

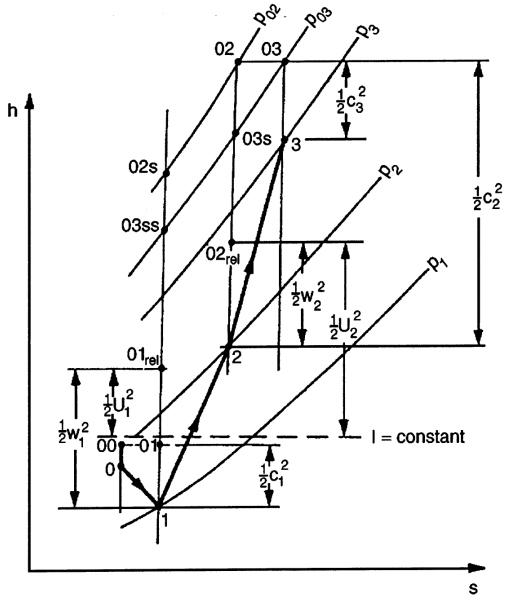

Fig. 3.3.0.1 Enthalpy- Entropy Diagram for Complete Centrifugal Compressor Stage (Dixon, 1998)

The flow through a compressor stage is a highly complicated, three- dimensional motion and a full analysis presents many problems of the highest order of difficulty. However, we can obtain approximate solutions quite readily by simplifying the flow model. We adopt the so- called one-dimensional approach which assumes that the fluid conditions are uniform over certain flow cross- sections. These cross- sections are conveniently taken immediately before and after the impeller as well as at inlet and exit of the entire machine. Where inlet vanes are used to give prerotation to the fluid entering the impeller, the one- dimensional treatment is no longer valid and an extension of the analysis is then required.

3.3.1 Inlet Casing

The fluid is accelerated from velocity c_0 to velocity c_1 and the static pressure falls from p_0 to p_1. Since the stagnation enthalpy is constant in steady, adiabatic flow without shaft work then $h_{00} = h_{01}$ or,

$$h_0 + \frac{1}{2}c_0^2 = h_1 + \frac{1}{2}c_1^2$$

Equation 3.3.1.1

3.3.2 Impeller

The general three- dimensional motion has components of velocity c_r, c_Θ and c_x respectively in the radial, tangential and axial directions and

$$c^2 = c_r^2 + c_\Theta^2 + c_x^2$$

Equation 3.3.2.1

Thus, the rothalpy is

$$I = h + \frac{1}{2}(c_r^2 + c_\Theta^2 + c_x^2 - 2Uc_\Theta)$$

Equation 3.3.2.2

Adding and subtracting $\frac{1}{2}U^2$ this becomes

$$I = h + \frac{1}{2}\{(U - c_\Theta)^2 + c_r^2 + c_x^2 - U^2\}$$

Equation 3.3.2.3

From the velocity triangle, $U - c_\Theta = w_\Theta$, and together with $w^2 = c_r^2 + w_\Theta^2 + c_x^2$:

$$I = h + \frac{1}{2}(w^2 - U^2)$$

Equation 3.3.2.4

or

$$I = h_{0,rel} - \frac{1}{2}U^2$$

Equation 3.3.2.5

since

$$h_{0,rel} = h + \frac{1}{2}w^2$$

Equation 3.3.2.6

Since $I_1 = I_2$ across the impeller,

$$h_2 - h_1 = \frac{1}{2}(U_2^2 - U_1^2) + \frac{1}{2}(w_1^2 - w_2^2)$$

Equation 3.3.2.7

The above expression provides the reason why the static enthalpy rise in a centrifugal compressor is so large compared with a single stage axial compressor. On the right hand side of the above expression, the second term $\frac{1}{2}(w_2^2 - w_1^2)$ is the contribution from the diffusion of relative velocity.
The first term, $\frac{1}{2}(U_2^2 - U_1^2)$, is the contribution due to the centrifugal action which is zero if the streamlines remain at the same radii before and after the impeller.
In centrifugal compressors and pumps, the absolute flow normally has no whirl component or angular momentum and $c_\Theta = 0$. This is the normal situation where the flow is free to enter axially. For such a flow the specific work done on the fluid is written as

$$\Delta W = U_2 c_{\Theta 2} = h_{02} - h_{01}$$

Equation 3.3.2.8

In high pressure ratio compressors it may be necessary to impart prerotation to the flow entering the impeller as a means of reducing a high relative inlet velocity. The effects of high relative velocity at the impeller inlet are experienced as Mach number effects in compressors and cavitation effects in pumps. The usual method of establishing prerotation requires the installation of a row of inlet guide vanes upstream of the impeller.

3.3.3 Conservation of Rothalpy

A cornerstone of the analysis of steady, relative flows in rotating systems has, for many years, been the immutable nature of the fluid mechanical property rothalpy.
The conditions under which the rothalpy of a fluid is conserved in the flow through impellers and rotors have been closely scrutinized by several researchers. Lyman (Lyman, 1993) reviewed the equations and physics governing the constancy of rothalpy in turbomachine fluid flows and found that an increase in rothalpy was possible for steady, viscous flow without heat transfer or body forces. He proved mathematically that the rothalpy increase was generated mainly by the fluid friction acting on the stationary shroud of the compressor considered. From his analysis, and put in the simplest terms, he deduced that:

$$h_{02} - h_{01} = (Uc_\Theta)_2 - (Uc_\Theta)_1 + \frac{W_f}{\dot{m}}$$

Equation 3.3.3.1

where $W_f = \dot{m}(I_2 - I_1)$ is the power loss due to fluid friction on the stationary shroud.

Lyman did not give any numerical values in support of his analysis. In the discussion of Lyman's paper, Moore disclosed that earlier viscous flow calculations of the flow in centrifugal flow compressors (Moore et al., 1984) of the power loss in a centrifugal compressor had shown a rothalpy production amounting to 1.2 per cent of the total work input. This was due to the shear work done at the impeller shroud and it was acknowledged to be of the same order of magnitude as the work done overcoming disc friction on the back face of the impeller. Often disc friction is ignored in preliminary design calculations. A later, careful, order- of- magnitude investigation by Bosman and Jadayel (Bosman et al., 1996) showed that the change in rothalpy through a centrifugal compressor impeller would be negligible under typical operating conditions. They also believed that it was not possible to accurately calculate the change in rothalpy because the effects due to inexact turbulence modelling and truncation error in computation would far exceed those due to non- conservation of rothalpy.

3.3.4 Diffuser

The fluid is decelerated adiabatically and the static pressure rising. The volute and outlet diffuser involve some further deceleration. As the stagnation enthalpy in steady adiabatic flow without shaft work is constant, $h_{02} = h_{03}$ or $h_2 + \frac{1}{2}c_2^2 = h_3 + \frac{1}{2}c_3^2$.

3.3.5 Inlet Velocity Limitations

The inlet eye is an important critical region in centrifugal pumps and compressors requiring careful consideration at the design stage. If the relative velocity of the inlet flow is too large in pumps, cavitation may result with consequent blade erosion or even reduced performance. In compressors large relative velocities can cause an increase in the impeller total pressure losses. In high-speed centrifugal compressors Mach number effects may become important with high relative velocities in the inlet. By suitable sizing of the eye the maximum relative velocity, or some related parameter, can be minimized to give the optimum inlet flow conditions.

3.4 Performance of Centrifugal Compressors

The performance of compressible flow machines is usually described in terms of the groups of variables presented in chapter 3.2. These characteristics are dependent on other variables such as the conditions of pressure and temperature at the compressor inlet and physical properties of the working fluid. To study the performance of a compressor completely, it is necessary to plot the total pressure coefficient $\pi = \frac{p_{03}}{p_{01}}$ against the mass flow parameter $\frac{\dot{m}\sqrt{T_{01}}}{p_{01}}$ for fixed speed intervals of $\frac{N}{\sqrt{T_{01}}}$. Figure 3.4.0.1 shows an idealized fixed speed characteristic. Consider a valve placed in the delivery line of a compressor running at constant speed. First, it is supposed that the valve is fully closed. Then the pressure ratio will have some value as indicated by Point A. This pressure ratio is available from vanes moving the air about in the impeller.

Now, it is supposed that the valve is opened and airflow begins. The diffuser contributes to the pressure rise, the pressure ratio increases, and at Point B, the maximum pressure occurs. But the compressor efficiency at this pressure ratio will be below the maximum efficiency. Point C indicates the further increase in mass flow,

but the pressure has dropped slightly from the maximum possible value. This is the design mass flow rate pressure ratio. Further increases in mass flow will increase the slope of the curve until point D. Point D indicates that the pressure rise is zero. However, as mentioned this is an idealized characteristic.

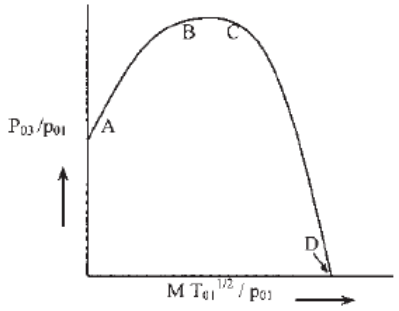

Fig. 3.4.0.1: Fixed Speed Characteristic (Dixon, 1998)

3.4.1 Determing the Pressure Ratio

Considering a centrifugal compressor having zero inlet swirl, compressing a perfect gas. With the usual notation the energy transfer is

$$\Delta W = \frac{W_c}{\dot{m}} = h_{02} - h_{01} = U_2 c_{\Theta 2}$$

Equation 3.4.1.1

The overall or total to total efficiency η_c is

$$\eta_c = \frac{h_{03,\,s} - h_{01}}{h_{03} - h_{01}} = \frac{c_p T_{01}\left(\frac{T_{03,\,s}}{T_{01}} - 1\right)}{h_{02} - h_{01}} = c_p T_{01} \frac{\left(\frac{T_{03,\,s}}{T_{01}} - 1\right)}{U_2 c_{\Theta 2}}$$

Equation 3.4.1.2

Now the overall pressure ratio is

$$\frac{p_{03}}{p_{01}} = \left(\frac{T_{03,\,s}}{T_{01}}\right)^{\frac{\kappa}{\kappa - 1}}$$

Equation 3.4.1.3

In all compressors the basic flow process is one of diffusion. Boundary layers are prone to separate and the flow is extremely complex. With separated wakes in the flow, unsteady flow downstream of the impeller can occur. It must be stressed that a broad understanding of the flow processes within a centrifugal compressor is still a vital requirement for the further progress of new design methods. A characteristic of all high performance compressors is that as the design pressure ratio has increased, so the range of mass flow between surge and choking has diminished. In the case of the centrifugal compressor, choking can occur when the mach number entering the diffuser passages is just in excess of unity. This is a severe problem which is aggravated by shock- induced separation of the boundary layers on the vanes which worsens the problem of flow blockage.

3.4.2 Effect of Backswept Vanes

Came (Came, 1978), Whitfield and Baines (Whitfield et al., 1990) have commented upon the trend towards the use of higher pressure ratios from single- stage compressors leading to more highly stressed impellers. The increasing use of back swept vanes and higher blade tip speeds result in higher direct stress in the impeller and bending stress in the non- radial vanes.

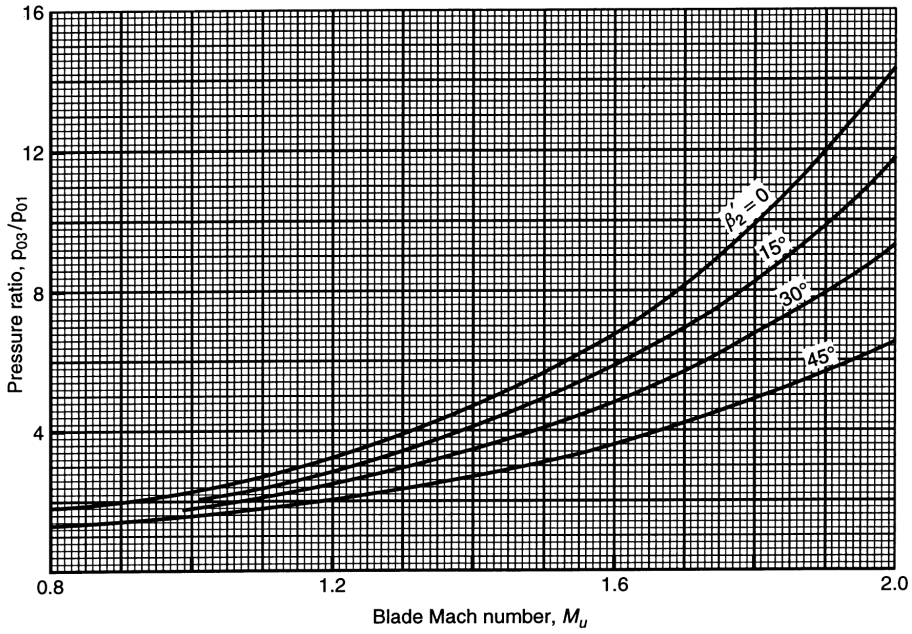

Fig. 3.4.2.1 Pressure Ratio vs Stage Mach Number for Different Backsweep Angles (Dixon, 1998)

The effect of using back swept impeller vanes on the pressure ratio is shown in figure 3.4.2.1 for a range of blade mach number. It is evident that the use of back sweep of the vanes at a given blade speed causes a loss in pressure ratio. In order to maintain a given pressure ratio it would be necessary to increase the design speed which, it has been noted already, increases the blade stresses. With high blade tip speeds the absolute flow leaving the impeller may have a mach number well in excess of unity. As this mach number can be related to the mach number at entry to the diffuser vanes, it is of some advantage to be able to calculate the former.

According to Whitfield and Baines (Withfield et al., 1990) the two most important aerodynamic parameters at impeller exit are the magnitude and direction of the absolute mach number M_2. If M_2 has a too high value, the process of efficient flow deceleration within the diffuser itself is made more difficult leading to high friction losses as well as the increased possibility of shock losses. If the flow angle α_2 is large the flow path in the vaneless diffuser will be excessively long resulting in high friction losses and possible stall and flow instability. Several researchers, e.g. Rodgers and Sapiro (Rodgers et al., 1972) have shown that the optimum flow angle is in the range $60° < \alpha_2 < 70°$. Backswept vanes give a reduction of the impeller discharge Mach number at any given tip speed. A designer making the change from radial vanes to back swept vanes will incur a reduction in the design pressure ratio if the vane tip speed remains the same. To recover the original pressure ratio the designer is forced to increase the blade tip speed which increases the discharge Mach number. Fortunately, it turns out that this increase in M_2 is rather less than the reduction obtained by the use of backsweep.

3.5 The Diffuser System

Centrifugal compressors and pumps are, in general, fitted with either a vaneless or a vaned diffuser to transform the kinetic energy at impeller outlet into static pressure.

3.5.1 Vaneless Diffusers

The simplest concept of diffusion in a radial flow machine is one where the swirl velocity is reduced by an increase in radius (conservation of angular momentum) and the radial velocity component is controlled by the radial flow area. From continuity, since $\dot{m} = \rho A c_r = 2\pi r b \rho c_r$, where b is the width of passage, then

$$c_r = \frac{r_2 b_2 \rho_2 c_{r2}}{r b \rho}$$

Equation 3.5.1.1

Assuming the flow is frictionless in the diffuser, the angular momentum is constant and $c_\Theta = c_{\Theta 2}\frac{r_2}{r}$. Now the tangential velocity component c_Θ is usually very much larger than the radial velocity component c_r. Therefore, the ratio of inlet to outlet diffuser velocities $\frac{c_2}{c_3}$ is approximately $\frac{r_3}{r_2}$. Clearly, to obtain useful reductions in velocity, vaneless diffusers must be large. This may not be a disadvantage in industrial applications where weight and size may be of secondary importance compared with the cost of a vaned diffuser. A factor in favour of vaneless diffusers is the wide operating range obtainable, vaned diffusers being more sensitive to flow variation because of incidence effects.

For a parallel- walled radial diffuser in incompressible flow, the continuity of mass flow equation requires that rc_1 is constant. Assuming that rc_Θ remains constant, then the absolute flow angle α_2 is also constant as the fluid is diffused outwards. Under these conditions the flow path is a logarithmic spiral.

3.5.2 Vaned Diffusers

In the vaned diffuser the vanes are used to remove the swirl of the fluid at a higher rate than is possible by a simple increase in radius, thereby reducing the length of flow path and diameter. The vaned diffuser is advantageous where small size is important.

The flow follows an approximately logarithmic spiral path to the vanes after which it is constrained by the diffuser channels. For rapid diffusion the axis of the channel is straight and tangential to the spiral as shown. The passages are generally designed on the basis of simple channel theory with an equivalent angle of divergence of between 8° and 12° to control separation.

In many applications of the centrifugal compressor, size is important and the outside diameter must be minimized. With a vaned diffuser the channel length can be crucial when considering the final size of the compressor. Clements and Artt (Clements et al., 1988) considered this and performed a series of experiments aimed at determining the optimum diffuser channel length to width ratio, L/W. They found that, on the compressor they tested, increasing L/W beyond 3.7 did not produce any improvement in the performance, the pressure gradient at that point having reached zero.

Another significant result found by them was that the pressure gradient in the diffuser channel when L/W > 2.13 was not greater than that which could be obtained in a vaneless diffuser. Hence, removing completely that portion of the diffuser after this point would yield the same pressure recovery as with the full diffuser.

The number of diffuser vanes can also have a direct bearing on the efficiency and surge margin of the compressor. It is now widely accepted that surge occurs at higher flow rates when vaned diffusers are used than when a simple vaneless diffuser design is adopted. Came and Herbert (Came et al., 1980) quoted an example where a reduction of the number of diffuser vanes from 29 to 13 caused a significant improvement in the surge margin. Generally, it is accepted that it is better to have fewer diffuser vanes than impeller vanes in order to achieve a wide range of surge- free flow. With several adjacent diffuser passages sharing the gas from one impeller passage, the uneven velocity distribution from that passage results in alternate diffuser passages being either starved or choked. This is an unstable situation leading to flow reversal in the passages and to surge of the compressor. When the number of diffuser passages is less than the number of impeller passages a more uniform total flow results.

3.6 Stall

Stalling of a stage will be defined as the aerodynamic stall, or the breakaway of the flow from the suction side of the blade airfoil. A multistage compressor may operate stably in the unsurged region with one or more of the stages stalled, and the rest of the stages unstalled. Stall, in general, is characterized by reverse flow near the blade tip, which disrupts the velocity distribution and hence adversely affects the performance of the succeeding stages.

Referring to the cascade of fig. 3.6.0.1, it is supposed that some non- uniformity in the approaching flow or in a blade profile causes blade B to stall. The air now flows onto blade A at an increased angle of incidence due to blockage of channel AB. The blade A then stalls, but the flow on blade C is now at a lower incidence, and blade C may unstall. Therefore the stall may pass along the cascade in the direction of lift on the blades. Rotating stall may lead to vibrations resulting in fatigue failure in other parts of the system.

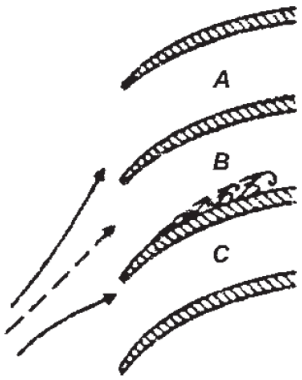

Fig. 3.6.0.1 Mechanism of Stall Propagation (Gorla et al., 2003)

3.7 Surging

Surging is marked by a complete breakdown of the continuous steady flow throughout the whole compressor, resulting in large fluctuations of flow with time and also in subsequent mechanical damage to the compressor. The phenomenon of surging should not be confused with the stalling of a compressor stage. Figure 3.7.0.1 shows typical overall pressure ratios and efficiencies of a centrifugal compressor stage. The pressure ratio for a given speed, unlike the temperature ratio, is strongly dependent on mass flow rate, since the machine is usually at its peak value for a narrow range of mass flows. When the compressor is running at a particular speed and the discharge is gradually reduced, the pressure ratio will first increase, peaks at a maximum value, and then decreased. The pressure ratio is maximized when the isentropic efficiency has the maximum value. When the discharge is further reduced, the pressure ratio drops due to fall in the isentropic efficiency. If the downstream pressure does not drop quickly there will be backflow accompanied by further decrease in mass flow. In the mean time, if the downstream pressure drops below the compressor outlet pressure, there will be increase in mass flow. This phenomenon of sudden drop in delivery pressure accompanied by pulsating flow is called surging. The point on the curve where surging starts is called the surge point. When the discharge pipe of the compressor is completely choked (mass flow is zero) the pressure ratio will have some value due to the centrifugal head produced by the impeller. Between the zero mass flow and the surge point mass flow, the operation of the compressor will be unstable. The line joining the surge points at different speeds gives the surge line.

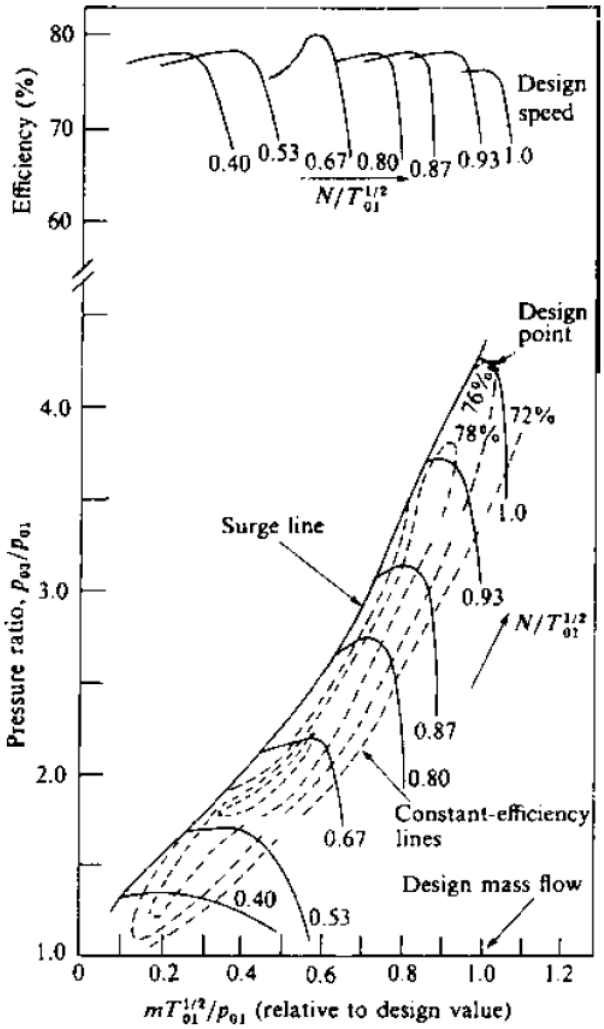

Fig. 3.7.0.1 Centrifugal Compressor Characteristic (Gorla et al., 2003)

3.8 Choking

When the velocity of fluid in a passage reaches the speed of sound at any cross section, the flow becomes choked (air ceases to flow). In the case of inlet flow passages, mass flow is constant. The choking behavior of rotating passages differs from that of the stationary passages, and therefore it is necessary to make separate analysis for impeller and diffuser, assuming one dimensional, adiabatic flow, and that the fluid is a perfect gas.

3.9 Internal Flow Fundamentals

3.9.1 Boundary Layer in a Bend

When a flow that is parallel but non- uniform in velocity or density is made to follow a curved path, the result is a three- dimensional motion with velocity components normal to the overall flow direction. Cross- flow of this type is associated with the generation of a streamwise component of vorticity and commonly referred to as secondary flow. The name derives from the view that one can identify a primary flow direction along a passage or bend and hence also specify the departures from this primary direction. Although the term secondary is in common use, it can be a misnomer because the cross- flow velocities are often a substantial fraction of the primary velocity.

The flow in a boundary layer on the bottom of a curved passage such as a rectangular bend furnishes an illustration of the type of motions to be addressed. Generation of secondary flow can be viewed in terms of the differential convection of boundary layer vorticity through the bend. The flow outside of the boundary layer can be considered as a two- dimensional irrotational stream.

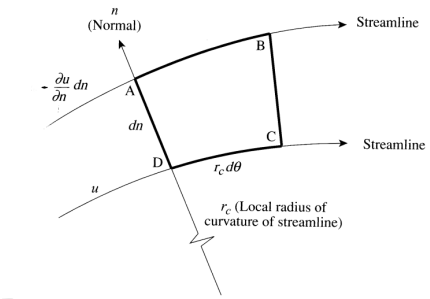

Fig. 3.9.1.1 Elementary Contour of Two Streamlines (Greitzer et al., 2004)

Figure 3.9.1.1 shows an elementary contour formed by two streamlines and two normals between the streamlines in a two- dimensional flow. From evaluation of the circulation around this contour, the component of vorticity perpendicular to the page $\omega_\perp$ can be written in terms of the rate of variation of velocity in the normal direction and the local streamline radius of curvature as

$$\omega_\perp = \frac{\partial u}{\partial n} + \frac{u}{r_c}$$

Equation 3.9.1.2

For a flow which is irrotational outside of the boundary layer, $\omega_\perp$, states that particles on the outside of a bend have a lower velocity than particles on the inside. Particles on the outside of the bend travel a longer distance than those on the inside. If boundary layer vortex lines are convected with a velocity proportional to the local free- stream velocity, vortex lines initially normal to the flow will be tipped into the streamwise direction as they traverse the bend with a resulting cross- flow. In a plane perpendicular to the free stream one can see the boundary layer fluid migrating towards the inside of the bend.

3.9.2 Inlet Flow Structure and its Effect on the Compressor Performance

The performance of centrifugal compressors can be seriously degraded by inlet flow distortions that result from an unsatisfactory inlet configuration. The distortion can be in static pressure or stagnation temperature, but the most common distortion is stagnation pressure. Such distortions often occur naturally because of the unsatisfactory nature of the inlet or because of operational effects. Very often the distortion is transient and it is generally recognized that the distortion will have little or no effect unless it persists for at least one revolution of the impeller. The distortion pattern is normally nonuniform in the circumferential and the radial sense. Circumferential distortion seems to be the most serious.
Ariga et al. (Ariga et al., 1982) investigated experimentally the influence of inlet distortion on the performance of a low- speed centrifugal compressor with vaneless diffuser, mainly in the impeller with artificially created radial and circumferential distortion generators by locating multiple layers of honeycomb at upstream of impeller and compared the result with the case of no distortion. According to his results, the distorted inlet profile degrades the impeller efficiency significantly by changing the incidence angle, especially in case of tip distortion. He observed the tendency that the performance degenerating effect due to the distortion grows as the rotational speed and the flow rate increases. The highest pressure and the lowest stable flow are achieved with inlets that have no distortion. Circumferential distortions create the largest loss of pressure ratio and flow angle. Circumferential distortions can be generated by non- axisymmetric obstacles such as struts or a bending duct.

3.10 Vibration and Noise

Blade vibration and noise are conveniently considered together for two reasons. Both are unsteady processes and each can be a serious nuisance. Of the two the problem of blade vibration is likely to be far more worrying to the designer because high levels of vibration can lead to part or all of the blades breaking off. Enormous amounts of downstream damage are then likely to occur possibly causing total destruction of the compressor. Noise is a less serious threat to the compressor itself and only in exceptional cases is the level of pressure fluctuation high enough to cause mechanical damage.

3.10.1 Vibration

The vibrations of blades in compressors and turbines have many features in common and in axial turbines vibration was a problem before the first axial compressor was built. Campbell's (Campbell, 1924) work on axial turbines carries over to today's compressors and is remembered in the Campbell diagram. The vulnerability of turbomachines to vibration, particularly axial machines, is not surprising in view of the use of long slender blades, the large gas loads, the proximity of moving and stationary components and the small amount of mechanical damping.

There are two quite different types of vibration to be considered. Forced vibration and flutter. The former, which is easier to understand and to obviate, arises from the movement of the rotor through disturbances which are usually stationary, for example wakes or potential field of an upstream stator, the wake of some upstream element such as a strut or the inlet distortion. It can also arise from the excitation produced by passing through rotating stall cells. Forced vibration becomes a problem when the excitation frequency coincides with a natural frequency of the blades. Flutter, on the other hand, is a self- excited oscillation or instability at or close to the natural frequency of the mechanical system which does not require any disturbance of finite amplitude to excite it.

3.10.2 Forced Vibration

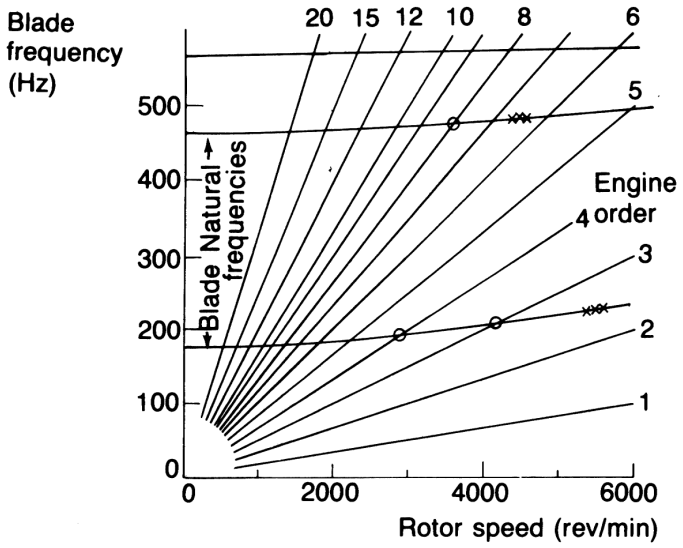

Fig. 3.10.2.1 Campbell Diagram for a Rotor Blade (circles indicate for forced resonances, crosses show either rotational stall or flutter) (Cumpsty, 2004)

The Campbell diagram (see fig. 3.10.2.1) is a convenient way to view the possible coincidence of blade natural frequency with excitation of the rotor blades by non- uniformities of the flow. Some of the engine orders are more important than others. The lowest engine orders tend to produce quite high excitation because the flow around the annulus is never truly uniform. There are several reasons for this. The inlet flow has non- uniform stagnation pressure because of ingested distortion or intake boundary layer effects or has static pressure distortion due to such effects as upstream bends. Inlet distortion tends to produce excitations at the low engine orders, the precise excitation being obtained from a Fourier analysis of the circumferential pattern. Struts upstream of downstream excite the blades at engine orders corresponding to their number and harmonics thereof. Upstream obstructions cause excitation by their potential flow effect and by their wakes. Downstream bodies can only affect the rotor by the potential flow effect. The potential flow effect decreases approximately exponentially with distance in the flow direction. The effect of the wake decreases more slowly than the potential effect and downstream of an obstruction the wake is usually more important.

In a radial compressor the vanes in a vaned diffuser are a powerful source of excitation of the impeller and one of the principal reasons for mounting the vanes some way out from the impeller is to reduce the strength of the excitation of the impeller by the static pressure field of the vanes.
The force and moment imparted to a blade as it experiences a non- uniform flow can be calculated in the case of inviscid two- dimensional flow. To be useful, such calculations need there to be an accurate input of the flow disturbance. To know whether the excitation will be a problem in turn requires an estimate of the mechanical damping.

3.11 The Rigi Test Rig at Turbomachinery Laboratory

The Turbomachinery Laboratory of ETH Zurich runs a centrifugal compressor test rig named after a famous mountain near Lucerne. In the past and today the test facility provides a solid basis to undertake research in the field of impeller aerodynamics, system instabilities, aerodynamic probe development and application of LDA measurement techniques. Currently the test facility is being redesigned aiming to extend its research capabilities into the field of forced response of radial compressors.

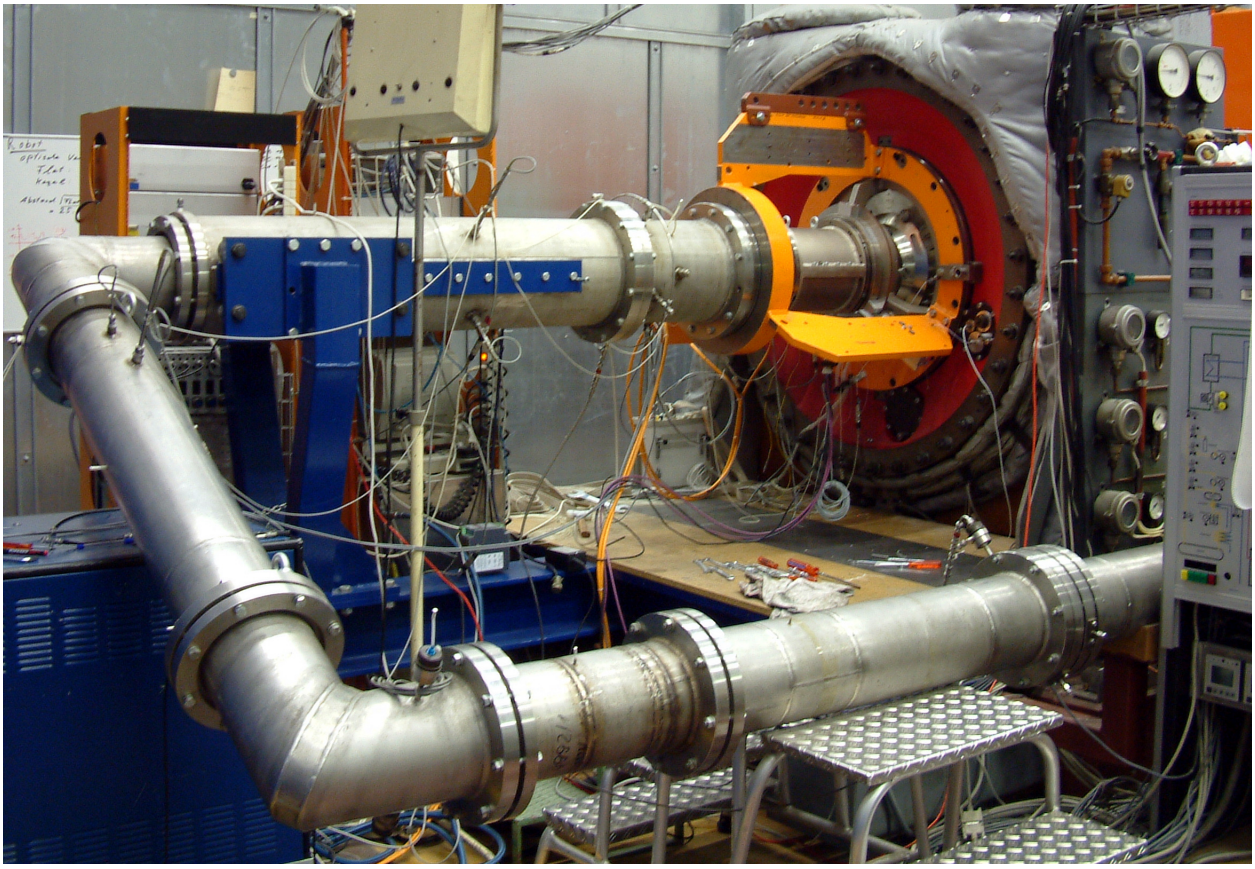

Fig. 3.11.0.1: RIGI Test Rig at Turbomachinery Laboratory ETH Zurich

3.11.1 Test Rig Features

RIGI is a closed loop facility. As such within the test section the pressure is adjusted independently from ambient conditions. During operation pressure and temperature at the inlet of the impeller are controlled for constant values. Herein the facility can be evacuated to 0.25 bar or pressurized to a maximum value of 4 bar. The maximum deliverable power to the rotating components is limited by the gearbox to 370kW and is provided by an electrical DC motor. RIGI allows maximum rotational speeds of 22000rpm. The mass flow is controlled through an orifice. Downstream of the impeller a water cooled heat exchanger reduces the fluid temperature to the required impeller inlet temperature.

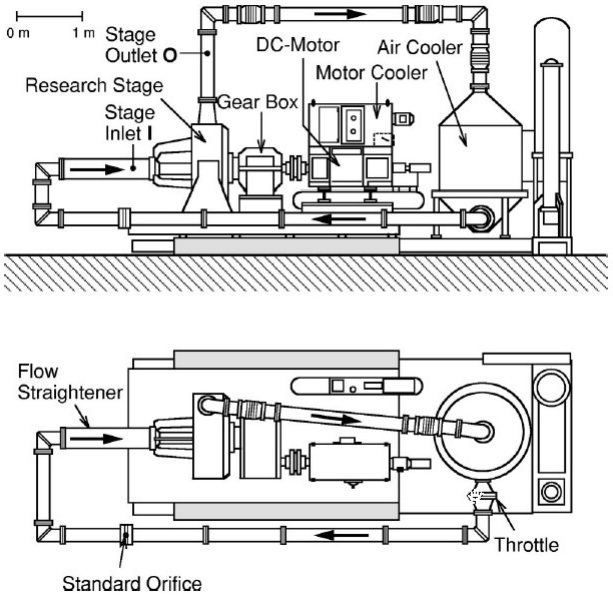

Fig. 3.11.1.1 Schematic of RIGI Test Rig Closed Loop

A number of impeller configurations have been investigated in the test facility with typical outer diameters of 280mm and pressure ratios around 2. In a recent research project an impeller was installed measuring 400mm on the outer diameter generating a maximum pressure ratio in the excess of 3. The diffuser section makes allowance to modify the diffuser configuration.

The impeller used in the measurements has an outer diameter of 400mm containing 7 main blades and 7 splitter blades. The impeller used for the forced vibration analysis has the same number but very thin blades. In the map in figure 3.11.1.2 the performance of both impeller blades is compared.

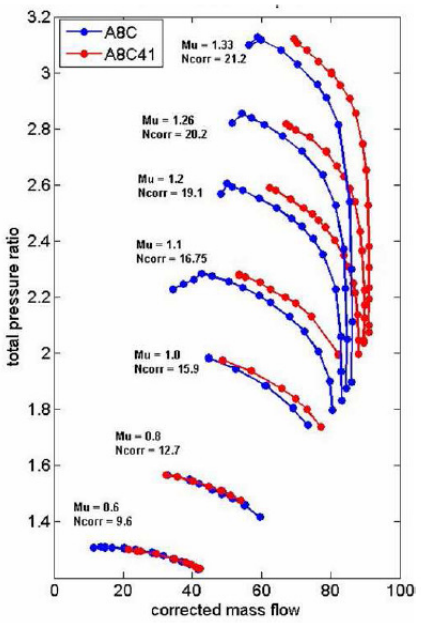

Fig. 3.11.1.2 Performance Map for A8C and A8C41 Impeller (A. Kammerer)

The A8C41 impeller is used for the forced vibration investigations. The blue line in figure 3.11.1.2 is the performance of the impeller used in the inlet flow field measurements. As mentioned the thin bladed impeller used for vibration analysis is populated with several strain gages. The inlet distortion may excite the blades of the impeller. A characteristic plot for the vibration analysis is the Campbell diagram:

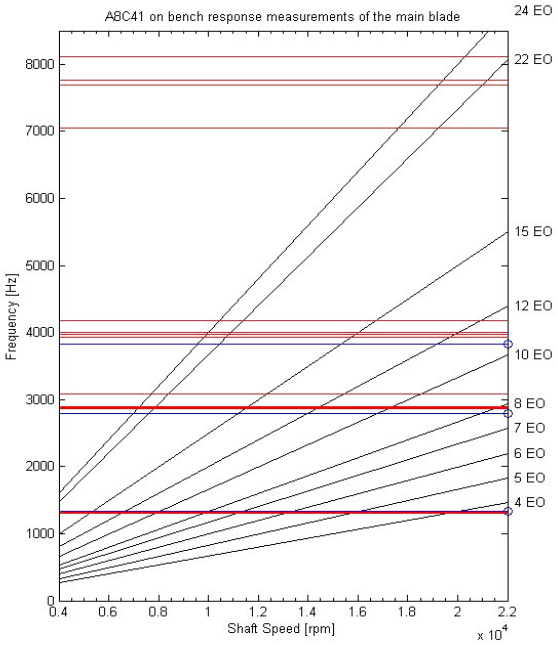

Fig. 3.11.1.3 Campbell Diagram for A8C41 Impeller (A. Kammerer)

The eigenfrequencies of the impeller are plotted against the shaft speed. Where the line of the engine order cross the line of the eigenfrequency the blades get into forced resonance. In the measurements the distortion screens to excite the second, third, fourth and fifth engine order are available.

3.12 Measurement Techniques

During operation two separate acquisition systems record data from sensors installed in the facility. On the one hand performance data is acquired in order to monitor and to control the operating conditions of the facility and on the other hand data is acquired from a set of fast response measurement techniques i.e. pressure transducers, the fast aerodynamic probe FRAP or the LDA system. In order to perform on impeller measurements, RIGI is currently being extended by Mr. Albert Kammerer by a rotating transmission system. This will allow to perform strain gauge and pressure sensor measurements on the impeller surface.

3.13 Measurement Setup

The flow properties are measured with a fast response aerodynamic probe (FRAP). To traverse an area of the inlet flow cross section a traversing system with the possibility to move the probe in radial as well as in the circumferential direction is needed. The simplest way of realizing it is to simply put the existing system on a ring rotating in circumferential direction driven by an additional electrical motor. The following photograph shows the huge gear and down right the gear of the motor. Top left the tower of the traversing system is visible. Also the probe stem of the FRAP probe can be seen looking very closely.

Fig. 3.13.0.1 Third Axis of Traversing System

To ensure the same inlet flow conditions as they will be in Albert Kammerers investigations the whole apparatus therefore is installed. Figure 3.13.0.2 shows a sectional view of the inlet section of the RIGI test rig.

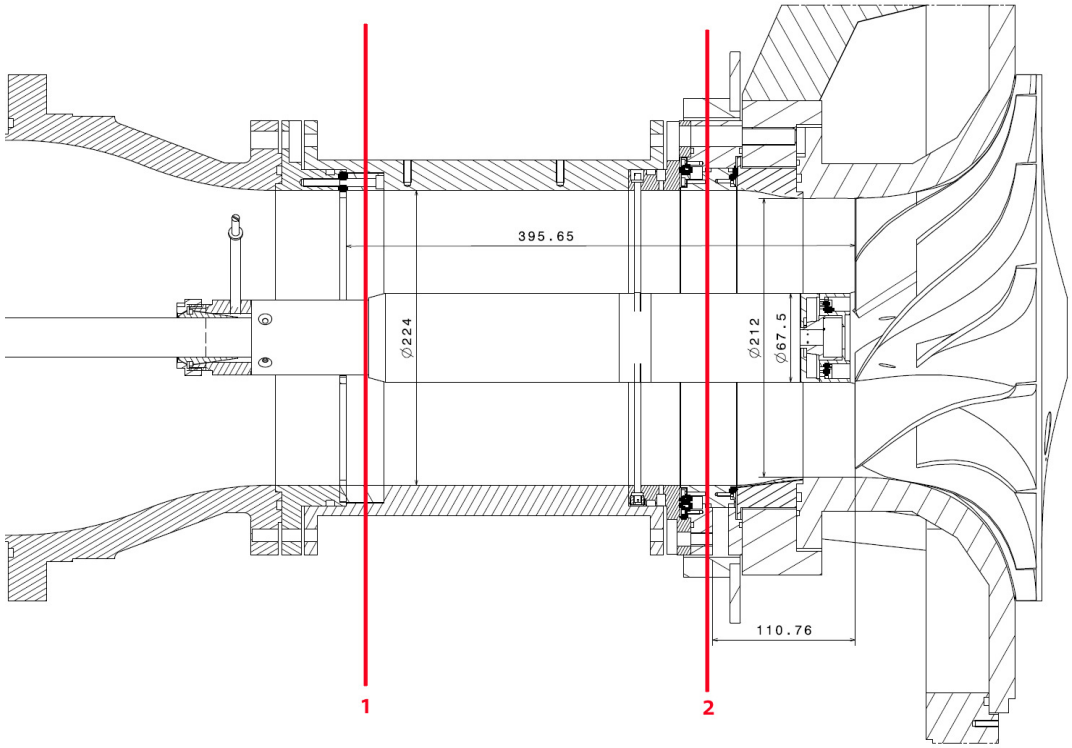

Fig. 3.13.0.2: Sectional View of Test Rig Inlet (A. Kammerer)

Plain 1 represents the location where the distortion will be generated and at position 2 the FRAP probe measures the inlet flow field. The tube in the center of the inlet channel is used for data transmission in Albert Kammerers experiments using a slip ring.

3.13.1 Distortion Screens

The distortion is generated by screens with different baffle geometries and different metal mains. The aim is to control the amplitude of the introduced distortions. The distortion as it passes through the impeller eye will excite the impeller blades. The layout of the baffles depends on the engine order to be excited. The engineering drawings show the screen layout for the engine orders two, four and five:

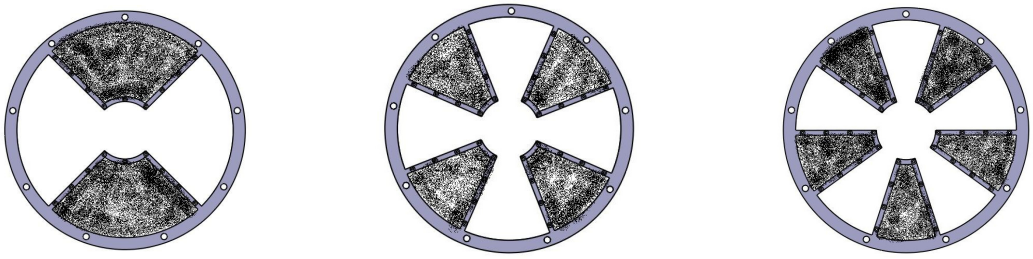

The parameters of the metal mains set the amplitude of the velocity variation over the circumference. The frame of the screens as well as the calculation of the grid properties was done by Albert Kammerer. With the required relationship the velocity variation depending on the grid parameters and the flow rate can be predicted.

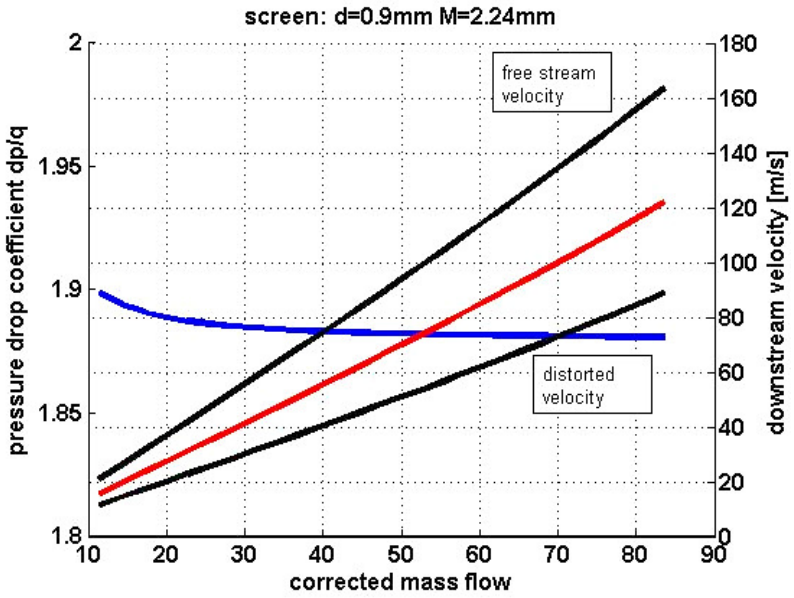

Fig. 3.13.1.1: Characteristics for Specified Grid Geometry (A. Kammerer)

The uniform flow field upstream the distortion screen redistributes due to the blockage effect of the distortion grid. The line named free stream velocity describes the value of the velocity passing the screen without blockage. Thus the free stream velocity is higher than the velocity of the uniform flow upstream the screen. In contrast to the undistorted flow the velocity of the portion passing the grid is lower.

If one knows the corrected mass flow rate the velocity of the flow after the grid and the velocity of the flow through the undistorted section of the screen can be reed off. The blue curve indicates the pressure drop coefficient.

3.14 Computational Fluid Dynamics

Computational Fluid Dynamics (CFD) is a computer- based tool for simulating the behavior of systems involving fluid flow, heat transfer and other related physical processes. It works by solving the equations of fluid flow in a special form over a region of interest, with specified known conditions on the boundary of that region.

3.14.1 History of CFD

Computers have been used to solve fluid flow problems for many years. Numerous programs have been written to solve either specific problems, or specific classes of problems. From the mid-1970's, the complex mathematics required to generalise the algorithms began to be understood, and general purpose CFD solvers were developed. These began to appear in the early 1980's and required what were then very powerful computers, as well as an in- depth knowledge of fluid dynamics, and large amounts of time to set up simulations. Consequently, CFD was a tool used almost exclusively in research. Recent advances in computing power, together with powerful graphics and interactive 3D- manipulation of models have made the process of creating a CFD model and analysing results much less labour intensive, reducing time and, hence, cost. Advanced solvers contain algorithms which enable robust solutions of the flow field in a reasonable time. As a result of these factors, Computational Fluid Dynamics is now an established industrial design tool, helping to reduce design timescales and improve processes throughout the engineering world. CFD provides a cost- effective and accurate alternative to scale model testing, with variations on the simulation being performed quickly, offering obvious advantages.

3.14.2 Mathematics of CFD

The set of equations which describe the processes of momentum, heat and mass transfer are known as the Navier- Stokes equations. These partial differential equations were derived in the early nineteenth century and have no known general analytical solution but can be discretised and solved numerically. Equations describing other processes, such as combustion, can also be solved in conjunction with the Navier- Stokes equations. Often, an approximating model is used to derive these additional equations, turbulence models being a particularly important example. There are a number of different solution methods which are used in CFD codes. The most common is known as the finite volume technique. In this technique, the region of interest is divided into small subregions, called control volumes. The equations are discretised and solved iteratively for each control volume. As a result, an approximation of the value of each variable at specific points throughout the domain can be obtained. In this way, one derives a full picture of the behaviour of the flow.

3.14.3 CFD Methodology

CFD may be used to determine the performance of a component at the design stage, or it can be used to analyse difficulties with an existing component and lead to its improved design. For example, the pressure drop through a component may be considered excessive:

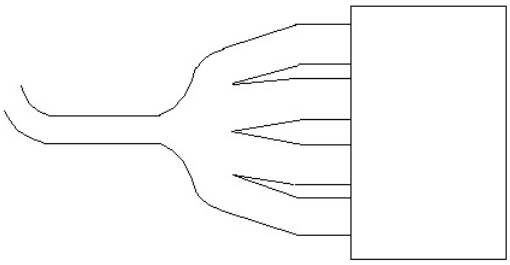

Fig. 3.14.3.1 Example Component (ANSYS, 2007)

The first step is to identify the region of interest:

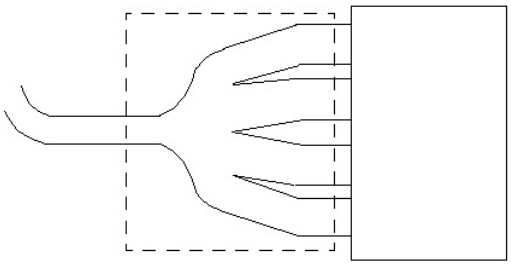

Fig. 3.14.3.2 Region of Interest (ANSYS, 2007)

The geometry of the region of interest is then defined and the mesh is created. After importing the mesh into the pre- processor, other elements of the simulation including the boundary conditions (inlets, outlets, etc.) and fluid properties are defined:

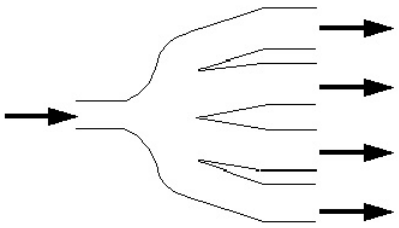

Fig. 3.14.3.3 Region of Interst with applied Boundary Conditions (ANSYS, 2007)

The flow solver is run to produce a file of results which contain the variation of velocity, pressure and any other variables throughout the region of interest. The results can be visualised and can provide an understanding of the behaviour of the fluid throughout the region of interest:

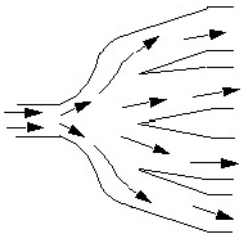

Fig. 3.14.3.4 Flow Field through Region of Interest (ANSYS, 2007)

This may lead to design modifications which can be tested by changing the geometry of the CFD model and seeing the effect. The process of performing a single CFD simulation is split into four components:

1. Geometry / Mesh
2. Physics Definition
3. Solver
4. Post- Processor

Geometry / Mesh:

This interactive process is the first pre- processing stage. The objective is to produce a mesh for input to the physics pre- processor. Before a mesh can be produced, a closed geometric solid is required. The geometry and mesh can be created in CAD2Mesh or any of the other geometry/mesh creation tools. The basic steps involve:

1. Defining the geometry of the region of interest
2. Creating regions of fluid flow, solid regions and surface boundary names
3. Setting properties for the mesh

Physics Definition:

This interactive process is the second pre- processing stage and is used to create input required by the Solver. The mesh files are loaded into the physics pre- processor. The physical models that are to be included in the simulation are selected. Fluid properties and boundary conditions are specified.

Solver:

The Solver produces the required results in a non- interactive/batch process. The problem is solved as follows:

1. The partial differential equations are integrated over all the control volumes in the region of interest. This is equivalent to applying a basic conservation law (e.g. for mass or momentum) to each control volume

2. These integral equations are converted to a system of algebraic equations by generating a set of approximations for the terms in the integral equations

3. The algebraic equations are solved iteratively

An iterative approach is required because of the non- linear nature of the equations, and as the solution approaches the exact solution, it is said to converge. For each iteration, an error, or residual, is reported as a measure of the overall conservation of the flow properties. How close the final solution is to the exact solution depends on a number of factors, including the size and shape of the control volumes and the size of the final residuals. Complex physical processes, such as combustion and turbulence, are often modeled using empirical relationships. The approximations inherent in these models also contribute to differences between the CFD solution and the real flow. The solution process requires no user interaction and is, therefore, usually carried out as a batch process. The solver produces a results file which is then passed to the post- processor.

Post- Processor:

The post- processor is the component used to analyse, visualise and present the results interactively. Post- processing includes anything from obtaining point values to complex animated sequences. Examples of some important features of post- processors are:

- Visualisation of the geometry and control volumes
- Vector plots showing the direction and magnitude of the flow
- Visualisation of the variation of scalar variables (variables which have only magnitude, not direction, such as temperature, pressure, ...) through the domain
- Quantitative numerical calculations
- Animation Charts showing graphical plots of variables
- Hardcopy output

3.14.4 Governing Equations

The software in use for the present work is the commercial ANSYS CFX 10.0 SP1 software containing the pre-processor, the solver and a post- processing tool. The governing equations are implemented in the code as they are described on the following pages.

Transport Equations:

The instantaneous equations of mass, momentum and energy conservation can be written as follows in a stationary frame of reference:

Continuity:

$$\frac{\partial \rho}{\partial t} + \nabla\bullet(\rho\vec{U}) = 0$$

Equation 3.14.4.1

Momentum Equations:

$$\frac{\partial(\rho\vec{U})}{\partial t} + \nabla\bullet(\overrightarrow{\rho U} \otimes \vec{U}) = -\nabla p + \nabla\bullet\tau + \vec{S}_M$$

Equation 3.14.4.2

where the stress tensor, τ, is related to the strain rate by

$$\tau = \mu\left(\nabla\vec{U} + (\nabla\vec{U})^T - \frac{2}{3}\delta\nabla\bullet\vec{U}\right)$$

Equation 3.14.4.3

Total Energy Equation:

$$\frac{\partial(\rho h_0)}{\partial t} - \frac{\partial p}{\partial t} + \nabla\bullet(\rho\vec{U}h_0) = \nabla\bullet(\lambda\nabla T) + \nabla\bullet(\vec{U}\bullet\tau) + \vec{U}\bullet\vec{S}_M + \vec{S}_E$$

Equation 3.14.4.4

where h_0 is the total Enthalpy. The term $\nabla\bullet(\vec{U}\bullet\tau)$ represents the work due to viscous stresses and is called the viscous work term. The term $\vec{U}\bullet\vec{S}_M$ represents the work due to external momentum sources and is currently neglected.

Equations of State:

The flow solver calculates pressure and static enthalpy. Finding density requires that we select the thermal equation of state and finding temperature requires that we select the constitutive relation. The selection of these two relationships is not necessarily independent and is also a modelling choice. The thermal equation of state is described as a function of both temperature and pressure:

$$\rho = \rho(p, T)$$

Equation 3.14.4.5

The specific heat capacity, c_p, may also be described as a function of temperature and pressure:

$$c_p = c_p(p, T)$$

Equation 3.14.4.6

For an ideal gas, the density is defined by the ideal gas law and, in this case, c_p can be a function of only temperature:

$$c_p = c_p(T)$$

Equation 3.14.4.7

Ideal Gas Equation of State:

For an ideal gas, the relationship is described by the ideal gas law:

$$\rho = \frac{w(p + p_{ref})}{R_0 T}$$

Equation 3.14.4.8

where w is the molecular weight of the gas and R_0 is the universal gas constant.

3.14.5 Turbulence Models

Turbulence consists of fluctuations in the flow field in time and space. It is a complex process, mainly because it is three dimensional, unsteady and consists of many scales. It can have a significant effect on the characteristics of the flow. Turbulence occurs when the inertia forces in the fluid become significant compared to viscous forces, and is characterised by a high Reynolds Number. In principle, the Navier- Stokes equations describe both laminar and turbulent flows without the need for additional information. However, turbulent flows at realistic Reynolds numbers span a large range of turbulent length and time scales, and would generally involve length scales much smaller than the smallest finite volume mesh, which can be practically used in a numerical analysis. The Direct Numerical Simulation (DNS) of these flows would require computing power which is many orders of magnitude higher than available in the foreseeable future.

To enable the effects of turbulence to be predicted, a large amount of CFD research has concentrated on methods which make use of turbulence models. Turbulence models have been specifically developed to account for the effects of turbulence without recourse to a prohibitively fine mesh and Direct Numerical Simulation. Most turbulence models are statistical turbulence model. The two exceptions to this are the Large Eddy Simulation model and the Detached Eddy Simulation model.

Statistical Turbulence Models and the Closure Problem:

When looking at time scales much larger than the time scales of turbulent fluctuations, turbulent flow could be said to exhibit average characteristics, with an additional time- varying, fluctuating component. For example, a velocity component may be divided into an average component and a time varying component. In general, turbulence models seek to modify the original unsteady Navier- Stokes equations by the introduction of averaged and fluctuating quantities to produce the Reynolds Averaged Navier- Stokes (RANS) equations. These equations represent the mean flow quantities only, while modelling turbulence effects without a need for the resolution of the turbulent fluctuations. All scales of the turbulence field are being modelled. Turbulence models based on the RANS equations are known as Statistical Turbulence Models due to the statistical averaging procedure employed to obtain the equations. Simulation of the RANS equations greatly reduces the computational effort compared to a Direct Numerical Simulation and is generally adopted for practical engineering calculations. However, the averaging procedure introduces additional unknown terms containing products of the fluctuating quantities, which act like additional stresses in the fluid. These terms, called 'turbulent' or 'Reynolds' stresses, are difficult to determine directly and so become further unknowns. The Reynolds (turbulent) stresses need to be modelled by additional equations of known quantities in order to achieve "closure." Closure implies that there is a sufficient number of equations for all the unknowns, including the Reynolds- Stress tensor resulting from the averaging procedure. The equations used to close the system define the type of turbulence model.

Reynolds Averaged Navier Stokes (RANS) Equations:

As described above, turbulence models seek to solve a modified set of transport equations by introducing averaged and fluctuating components. For example, a velocity $\vec{U}$ may be divided into an average component and a time varying component:

$$U(t) = \overline{U} + u'(t)$$

Equation 3.14.5.1

The averaged component is given by:

$$\overline{U} = \frac{1}{\Delta t}\int_{t}^{(t+\Delta t)} U(t)dt$$

Equation 3.14.5.2

where Δt is a time scale that is large relative to the turbulent fluctuations, but small relative to the time scale to which the equations are solved.

Substituting the time averaged quantities into the original transport equations results in the Reynolds- averaged equations given below:

Continuity:

$$\frac{\partial \rho}{\partial t} + \nabla \bullet (\rho \vec{U}) = 0$$

Equation 3.14.5.3

Momentum:

$$\frac{\partial (\rho \vec{U})}{\partial t} + \nabla \bullet (\rho \vec{U} \otimes \vec{U}) = \nabla \bullet (\tau - \rho \overline{u' \otimes u'}) + \vec{S}_M$$

Equation 3.14.5.4

Scalar Transport:

$$\frac{\partial (\rho \phi)}{\partial t} + \nabla \bullet (\rho \vec{U} \phi) = \nabla \bullet (\Gamma \nabla \phi - \rho \overline{u' \phi}) + \vec{S}_E$$

Equation 3.14.5.5

with ϕ as a non reacting scalar.

The continuity equation has not been altered but the momentum and scalar transport equations contain turbulent flux terms additional to the molecular diffusive fluxes. These are the Reynolds stress, $\rho \overline{u' \otimes u'}$, and the Reynolds flux, $\rho \overline{u' \phi}$. These terms arise from the non- linear convective term in the un- averaged equations. They reflect the fact that convective transport due to turbulent velocity fluctuations will act to enhance mixing over and above that caused by thermal fluctuations at the molecular level. At high Reynolds numbers, turbulent velocity fluctuations occur over a length scale much larger than the mean free path of thermal fluctuations, so that the turbulent fluxes are much larger than the molecular fluxes.

The Reynolds- averaged energy equation is:

$$\frac{\partial (\rho h_0)}{\partial t} + \nabla \bullet (\rho \vec{U} h_0 + \rho \overline{u' h} - \lambda \nabla T) = \frac{\partial p}{\partial t}$$

Equation 3.14.5.6

where the mean total enthalpy is given by:

$$h_0 = h + \frac{1}{2} U^2 + k$$

Equation 3.14.5.7

In addition to the mean flow kinetic energy, the total enthalpy now contains a contribution from the turbulent kinetic energy, k, given by:

$$k = \frac{1}{2} \overline{u'^2}$$

Equation 3.14.5.8

Turbulence models close the Reynolds- averaged equations by providing models for the computation of the Reynolds stresses and Reynolds fluxes.

Eddy Viscosity Turbulence Models:

One proposal suggests that turbulence consists of small eddies which are continuously forming and dissipating, and in which the Reynolds stresses are assumed to be proportional to mean velocity gradients. This defines an 'eddy viscosity model.' The eddy viscosity hypothesis assumes that the Reynolds stresses can be related to the mean velocity gradients and Eddy (turbulent) Viscosity by the gradient diffusion hypothesis, in a manner analogous to the relationship between the stress and strain tensors in laminar Newtonian flow:

$$-\rho\overline{u' \otimes u'} = -\frac{2}{3}\rho k\delta - \frac{2}{3}\mu_t \nabla\bullet\vec{U}\delta + \mu_t(\nabla\vec{U} + (\nabla\vec{U})^T)$$

Equation 3.14.5.9

here, μ_t is the Eddy Viscosity or Turbulent Viscosity. This has to be prescribed. Analogous to the eddy viscosity hypothesis is the eddy diffusivity hypothesis, which states that the Reynolds fluxes of a scalar are linearly related to the mean scalar gradient:

$$-\rho\overline{u'\phi} = \Gamma_t \nabla\phi$$

Equation 3.14.5.10

here, Γ_t is the Eddy Diffusivity and has to be prescribed. The Eddy Diffusivity can be written as:

$$\Gamma_t = \frac{\mu_t}{Pr_t}$$

Equation 3.14.5.11

where Pr_t is the turbulent Prandtl number. Eddy diffusivities are then prescribed using the turbulent Prandtl number.

The above equations can only express the turbulent fluctuation terms of functions of the mean variables if the turbulent viscosity is known. Both the $k-\varepsilon$ and $k-\omega$ two- equation turbulence models provide this variable. Subject to these hypotheses, the Reynolds averaged momentum and scalar transport equations become:

$$\frac{\partial(\rho\vec{U})}{\partial t} + \nabla\bullet(\rho\vec{U}\otimes\vec{U}) = \vec{B} - \nabla p' + \nabla\bullet(\mu_{eff}(\nabla\vec{U} + (\nabla U)^T))$$

Equation 3.14.5.12

$$\frac{\partial(\rho\phi)}{\partial t} + \nabla\bullet(\rho\vec{U}\phi - \Gamma_{eff}\nabla\phi) = \vec{S}$$

Equation 3.14.5.13

where $\vec{B}$ is the sum of the body forces, μ_{eff} is the effective viscosity and Γ_{eff} is the effective diffusivity, defined by:

$$\mu_{eff} = \mu + \mu_t$$

Equation 3.14.5.14

and:

$$\Gamma_{eff} = \Gamma + \Gamma_t$$

Equation 3.14.5.15

p' is a modified pressure, defined by:

$$p' = p + \frac{2}{3}\rho k + \nabla\bullet\vec{U}\left(\frac{2}{3}\mu_{eff} - \zeta\right)$$

Equation 3.14.5.16

where ζ is the bulk viscosity.

The Reynolds averaged energy equation becomes:

$$\frac{\partial(\rho h_0)}{\partial t} - \frac{\partial p}{\partial t} + \nabla\bullet(\rho\vec{U}h_0) = \nabla\bullet\left(\lambda\nabla T + \frac{\mu_t}{Pr_t}\nabla h\right) + \vec{S}_E$$

Equation 3.14.5.17

It has to be remarked that although the transformation of the molecular diffusion term may be inexact if enthalpy depends on variables other than temperature, the turbulent diffusion term is correct, subject to the eddy diffusivity hypothesis. Moreover, as turbulent diffusion is usually much larger than molecular diffusion, small errors in the latter can be ignored.

Two Equation Turbulence Models:

Two- equation turbulence models are very widely used, as they offer a good compromise between numerical effort and computational accuracy. Two- equation models are much more sophisticated than the zero equation models. Both the velocity and length scale are solved using separate transport equations (hence the term 'two- equation'). The $k-\varepsilon$ and $k-\omega$ two- equation models use the gradient diffusion hypothesis to relate the Reynolds stresses to the mean velocity gradients and the turbulent viscosity. The turbulent viscosity is modelled as the product of a turbulent velocity and turbulent length scale. In two- equation models, the turbulence velocity scale is computed from the turbulent kinetic energy, which is provided from the solution of its transport equation. The turbulent length scale is estimated from two properties of the turbulence field, usually the turbulent kinetic energy and its dissipation rate. The dissipation rate of the turbulent kinetic energy is provided from the solution of its transport equation.

In all the solved cases in the present work, the $k-\varepsilon$ two- equation model is used due to the fact that the other turbulence models (namely $k-\omega$ and SST) did not result in a stable convergence history.

The $k-\varepsilon$ Turbulence Model:

k is the turbulence kinetic energy and is defined as the variance of the fluctuations in velocity. It has dimensions of (L^2T^{-2}). ε is the turbulence eddy dissipation (the rate at which the velocity fluctuations dissipate), and has dimensions of k per unit time (L^2T^{-3}). The $k-\varepsilon$ model introduces two new variables into the system of equations.

The continuity equation is then:

$$\frac{\partial \rho}{\partial t} + \nabla\bullet(\rho\vec{U}) = 0$$

Equation 3.14.5.18

and the momentum equation becomes:

$$\frac{\partial(\rho\vec{U})}{\partial t} + \nabla\bullet(\rho\vec{U}\otimes\vec{U}) - \nabla\bullet(\mu_{eff}\nabla\vec{U}) = \nabla p' + \nabla\bullet(\mu_{eff}\nabla\vec{U})^T + \vec{B}$$

Equation 3.14.5.19

where $\vec{B}$ is the sum of body forces, μ_{eff} is the effective viscosity accounting for turbulence and p' is the modified pressure given by:

$$p' = p + \frac{2}{3}\rho k$$

Equation 3.14.5.20

The $k-\varepsilon$ model is based on the eddy viscosity concept, so that:

$$\mu_{eff} = \mu + \mu_t$$

Equation 3.14.5.21

where μ_t is the turbulence viscosity. The $k-\varepsilon$ model assumes that the turbulence viscosity is linked to the turbulence kinetic energy and dissipation via the relation:

$$\mu_t = C_\mu \rho \frac{k^2}{\varepsilon}$$

Equation 3.14.5.22

where C_μ is a constant.

The values of k and ε come directly from the differential transport equations for the turbulence kinetic energy and turbulence dissipation rate:

$$\frac{\partial(\rho k)}{\partial t} + \nabla\bullet(\rho\vec{U}k) = \nabla\bullet\left[\left(\mu + \frac{\mu_t}{\sigma_k}\right)\nabla k\right] + P_k - \rho\varepsilon$$

Equation 3.14.5.23

$$\frac{\partial(\rho\varepsilon)}{\partial t} + \nabla\bullet(\rho\vec{U}\varepsilon) = \nabla\bullet\left[\left(\mu + \frac{\mu_t}{\sigma_\varepsilon}\right)\nabla\varepsilon\right] + \frac{\varepsilon}{k}(C_{\varepsilon 1}P_k - C_{\varepsilon 2}\rho\varepsilon)$$

Equation 3.14.5.24

where $C_{\varepsilon 1}$, $C_{\varepsilon 2}$, σ_k and σ_ε are constants.

P_k is the turbulence production due to viscous and buoyancy forces, which is modelled using:

$$P_k = \mu_t \nabla\vec{U} \bullet (\nabla\vec{U} + \nabla\vec{U}^T) - \frac{2}{3}\nabla\bullet\vec{U}(3\mu_t\nabla\bullet\vec{U} + \rho k) + P_{k0}$$

Equation 3.14.5.25

Modelling Flow Near the Wall:

The wall distance is used in various functions that control the transition between near- wall and free- stream models. The wall- function approach in the commercial code used for the present work, ANSYS CFX, is an extension of the method of Launder and Spalding (Launder et al., 1974). In the log- law region, the near wall tangential velocity is related to the wall- shear- stress, τ_ω, by means of a logarithmic relation. In the wall- function approach, the viscosity affected sublayer region is bridged by employing empirical formulas to provide near-wall boundary conditions for the mean flow and turbulence transport equations. These formulas connect the wall conditions (e.g., the wall- shear- stress) to the dependent variables at the near- wall mesh node which is presumed to lie in the fully- turbulent region of the boundary layer. The logarithmic relation for the near wall velocity is given by:

$$u^+ = \frac{U_t}{u_\tau} = \frac{1}{\kappa}\ln(y^+) + C$$

Equation 3.14.5.26

where:

$$y^+ = \frac{\rho\Delta y u_\tau}{\mu}$$

Equation 3.14.5.27

and:

$$u_\tau = \left(\frac{\tau_\omega}{\rho}\right)^{1/2}$$

Equation 3.14.5.28

u^+ is the near wall velocity, u_τ is the friction velocity, U_t is the known velocity tangent to the wall at a distance of Δy from the wall, y^+ is the dimensionless distance from the wall, τ_ω is the wall shear stress, κ is the von Karman constant and C is a log- layer constant depending on wall roughness.

The equation for the near wall velocity u^+ has the problem that it becomes singular at separation points where the tangential velocity approaches zero. In the logarithmic region, an alternative velocity scale, u^* can be used instead of u^+:

$$u^* = C_\mu^{1/4} k^{1/2}$$

Equation 3.14.5.29

This scale has the useful property that it does not go to zero if U_t goes to zero. In turbulent flow k is never completely zero. Based on this definition, the following explicit equation for u_τ can be obtained:

$$u_\tau = \frac{U_t}{\frac{1}{\kappa}\ln(y^*) + C}$$

Equation 3.14.5.30

The absolute value of the wall shear stress is then obtained from:

$$\tau_{\omega} = \rho u^* u_{\tau}$$

Equation 3.14.5.31

where:

$$y^* = \frac{\rho u^* \Delta y}{\mu}$$

Equation 3.14.5.32

One of the major drawbacks of the wall- function approach is that the predictions depend on the location of the point nearest to the wall and are sensitive to the near- wall meshing; refining the mesh does not necessarily give a unique solution of increasing accuracy (Grotjans et al., 1998). The problem of inconsistencies in the wall- function, in the case of fine meshes, can be overcome with the use of the Scalable Wall Function formulation developed by CFX. It can be applied on arbitrarily fine meshes and allows to perform a consistent mesh refinement independent of the Reynolds number of the application. The basic idea behind the scalable wall- function approach is to limit the y^* value used in the logarithmic formulation by a lower value of $y^* = max(y^*, 11.06)$. 11.06 is the intersection between the logarithmic and the linear near wall profile. The computed y^* is therefore not allowed to fall below this limit. Therefore, all mesh points are outside the viscous sublayer and all fine mesh inconsistencies are avoided.

Numerical Discretisation:

Analytical solutions to the Navier Stokes equations exist for only the simplest of flows under ideal conditions. To obtain solutions for real flows, a numerical approach must be adopted whereby the equations are replaced by algebraic approximations which may be solved using a numerical method.
Segregated solvers employ a solution strategy where the momentum equations are first solved, using a guessed pressure, and an equation for a pressure correction is obtained. Because of the ‘guess- and- correct' nature of the linear system, a large number of iterations are typically required in addition to the need for judiciously selecting relaxation parameters for the variables. ANSYS CFX uses a coupled solver, which solves the hydrodynamic equations as a single system. This solution approach uses a fully implicit discretisation of the equations at any given time step. For steady state problems, the time- step behaves like an ‘acceleration parameter', to guide the approximate solutions in a physically based manner to a steady- state solution. This reduces the number of iterations required for convergence to a steady state, or to calculate the solution for each time step in a time dependent analysis.
All numerical approximation schemes are prone to a degree of error. Some errors are a result of truncation of additional terms in series expansions. Others are a result of the order of the differencing scheme used for the approximation.

Numerical Diffusion:

Numerical diffusion is usually exhibited by difference equations where the advection term has been approximated using an odd- order scheme which is first order accurate. The effect of this over a whole flow domain is that the features of the flow are smeared out. This phenomenon is sometimes called ‘gradient smearing.' The effect varies according to the alignment of the mesh with the flow direction. It is therefore relatively straightforward to achieve highly accurate solutions to simple flow problems, such as flow in a duct where alignment of the mesh with the predominant flow is relatively simple. However, for situations in which the flow is predominantly not aligned with the mesh, numerical diffusion effects limit the accuracy of the solution.

Numerical Dispersion:

Numerical dispersion is usually exhibited by discretised equations whose advection term has been approximated using schemes that are even- order accurate. Dispersion results in oscillations or ‘wiggles' in the solution particularly where there are steep flow gradients (e.g., across a shock).

4. Results

4.1 Stationary CFD

The stationary CFD investigation of the centrifugal compressor provides a basis to validate the numerical model via comparison with the measured performance of the test rig. In addition to the performance of the machine (pressure ratio versus mass flow), the total pressure distribution and the absolute flow angle profile from hub to shroud in the diffuser section of the compressor provides the possibility for a detailed validation of the model. The simulation over a broad range of operating points allows a characterization of the flow through the impeller.

4.1.1 Grid

The grid used for the CFD investigation consists of one main blade and one splitter blade representing the seventh part of the entire impeller. The grid is from ABB Turbo Systems made by Dr. Matthias Schleer and can essentially be divided in four subdomains shown in the figure below:

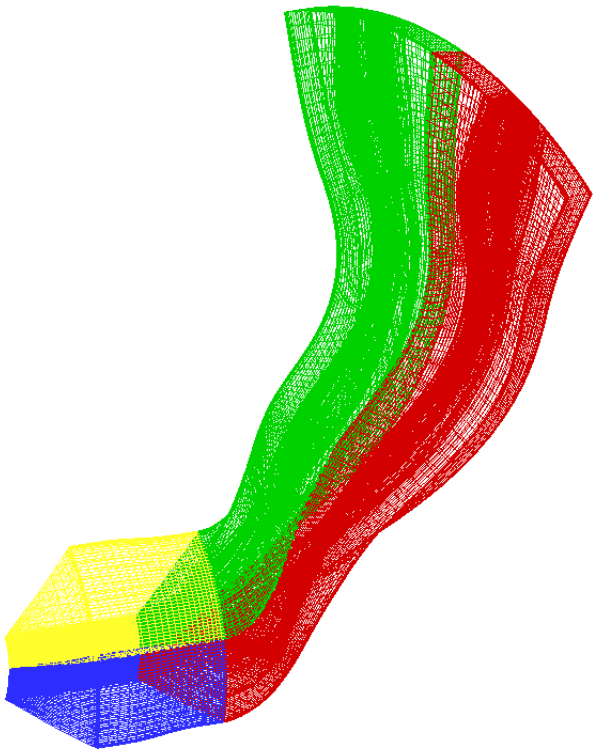

Fig. 4.1.1.1: CFD Grid (Seventh Part of Impeller)

The illustrated part of the grid consists of 571‘600 nodes building 509‘184 elements (hexahedra) and corresponds to the geometry of the A8C41 impeller used for the strain gage measurements of Albert Kammerer. The y^+ values are in the required range for the solver used in the present work.

The number and distribution of nodes and associated elements leads to the required grid quality showed in the following illustration:

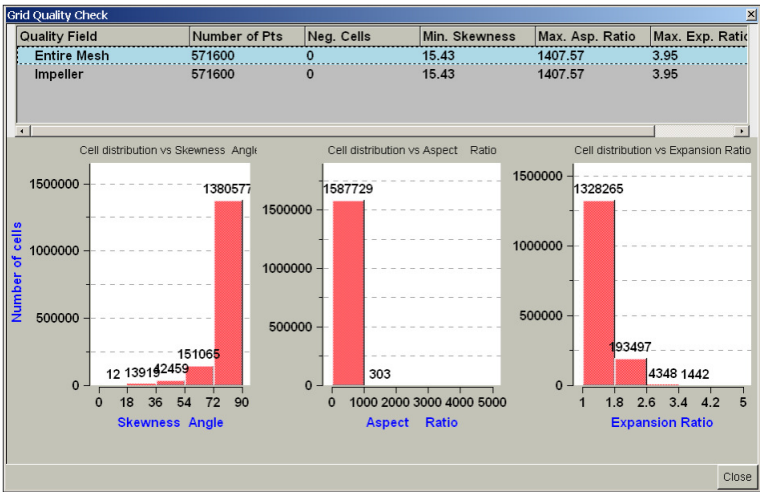

Fig. 4.1.1.2: Grid Quality Check (ANSYS ICEM CFD, Dr. M. Schleer)

Skewness:

This histogram is based upon calculations of the maximum skewness of a hexahedral or quadrilateral element. The skewness is defined differently for volume and surface elements. For a volume element, it is obtained by taking all pairs of adjacent faces and computing the normals.

Aspect ratio:

For hexahedral and quadrilateral elements, the aspect ratio is defined as the ratio of the distances between diagonally opposite vertices (shorter diagonal/longer diagonal). For tetrahedral elements, MED calculates the ratio between the radii of an inscribed sphere to a circumscribed sphere for each element. For triangular elements, this operation is done using circles.

4.1.2 Boundary Conditions

The common setup for the boundary conditions leading to a stable convergence of the solution is to set the total pressure and total temperature at the inlet of the model and the static pressure at the outlet. Both the total pressure and total temperature are available from performance measurements of the test rig at the corresponding operating point and are held constant by the system during the measurement campaign.

The outlet static pressure is adjusted to match the measured mass flow due to the fact that the outlet static pressure is not measured at the same location in the test rig compared to the location of the outlet in the computational domain.

An additional remark concerns the diffuser part of the centrifugal compressor. As illustrated, the model consists of four subdomains. The diffuser is not implemented as separate domain. To make allowance to zero wall velocity of the diffuser part a velocity contrary to the rotational direction of the impeller is impressed on each node modelling the diffuser wall.

Boundary Conditions for the stationary CFD investigation:

Inlet:	constant total pressure and total temperature (performance measurement)
Outlet:	static pressure (average static pressure, varied until mass flow matches measurement)
Shroud:	counter rotating wall, no slip, adiabatic
Impeller:	constant rotational speed, no slip, adiabatic
Fluid Boundaries:	periodic interfaces (rotational)

4.1.3 Turbulence Model and Solver Setup

The software used for the CFD investigation is the commercial ANSYS CFX software. The ANSYS Solver is a coupled solver which solves the hydrodynamic equations as a single system. This solution approach uses a fully implicit discretisation of the equations at any time step. For stationary problems the time step behaves like an acceleration parameter to guide the approximate solutions in a physically based manner to a steady state solution.

Several turbulence models (namely $k-\varepsilon$, $k-\omega$ and SST) have been applied to compare the stability of the solver process. Only the $k-\varepsilon$ turbulence model resulted in a stable solution of the set of equations. Both the $k-\omega$ and SST turbulence model showed bad convergence compared to the $k-\varepsilon$ model and strong recirculation (up to 15% of the outlet area) at the outlet of the domain. An explanation of the stable solution with the $k-\varepsilon$ model might be the diffusive characteristic of this turbulence model. For a detailed description of the $k-\varepsilon$ turbulence model the reader is referred to chapter 3.14.5.

For the steady state investigations a constant turbulence intensity of 5% which is a reasonable value for nominal turbulence through a circular inlet is applied as inlet boundary condition. Comparison of the effect of different turbulence intensities (1%, 5%, 10% and 15%) at the inlet on the resulting solution showed negligible importance for the stationary CFD investigation.

4.1.4 Convergence Quantification

Solver Residual:

The residual is a measure of the local imbalance of each conservative control volume equation. It is the most important measure of convergence as it relates directly to whether the equations have been solved. The residual is calculated using only the spatial flux terms and essentially represents a discrete conservation balance. The following residual plot representatively shows the convergence history of the stationary simulations:

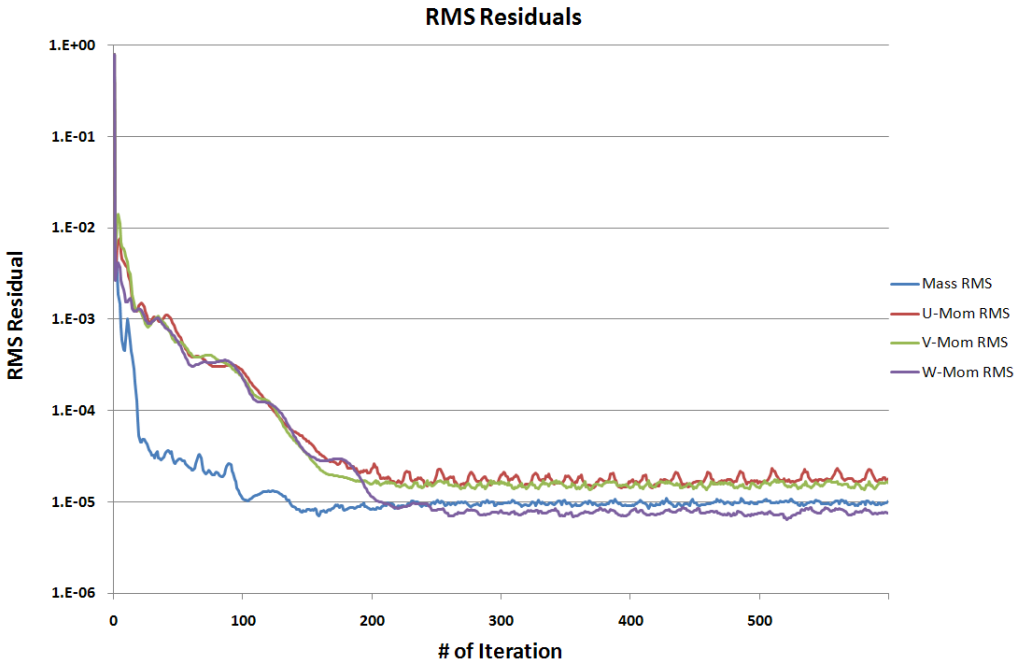

Fig. 4.1.4.1: RMS Residuals

According to the CFX Solver Guidelines a decrease of the RMS residuals of the main kinematic properties of at least three orders of magnitudes is required.

A second information about the solution process is the value and location of the maximum residual. This information provides the place in the computational domain where the set of equation causes numerical instabilities. The plot of the maximum residuals of the main kinematic properties below indicates what one expects. The values of the maximum residuals are, as a matter of course, higher compared to the root mean square values. A decrease of the maximum residuals of the order of about three orders of magnitudes implies acceptable convergence.

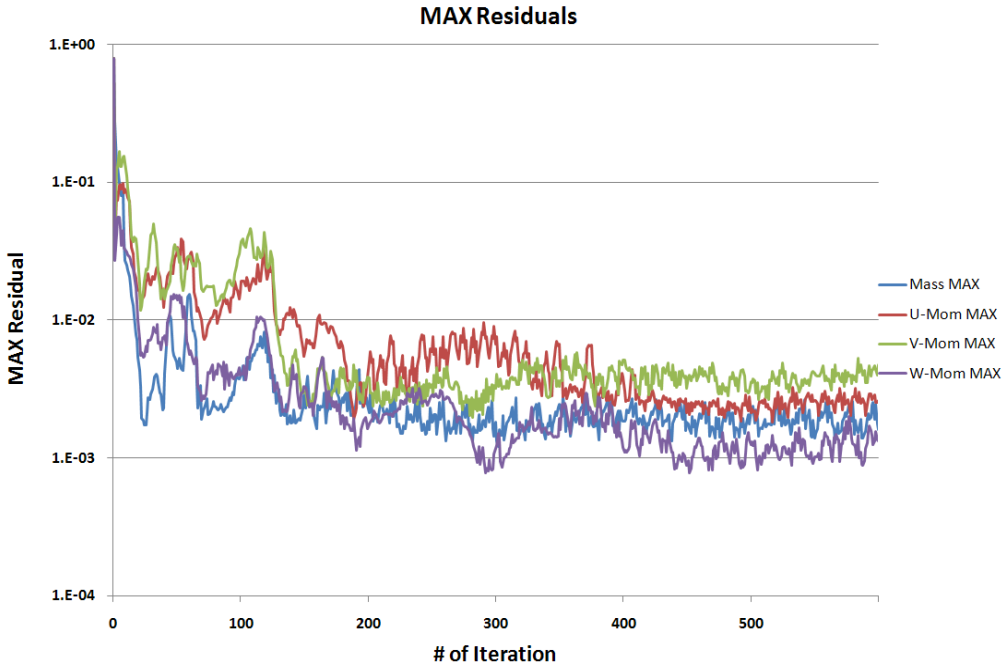

Fig. 4.1.4.2: Maximum Residuals

The location of the maximum residuals is illustrated below. It is, unsurprisingly, at the exit of the domain in the diffuser part of the model:

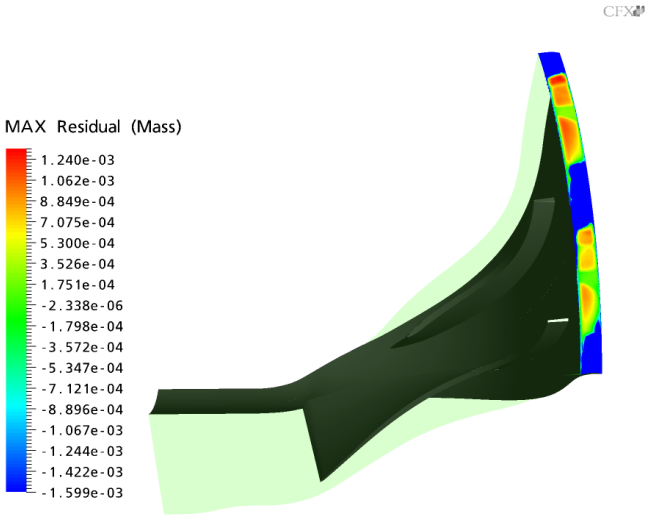

Fig. 4.1.4.3: Location of MAX residual

It is not a surprise due to the fact that the boundary surface is part of a rotating domain. Therefore the whole set of equations is solved in the relative frame of reference leading to extremely small angles between the relative flow direction and the surface of the domain boundary:

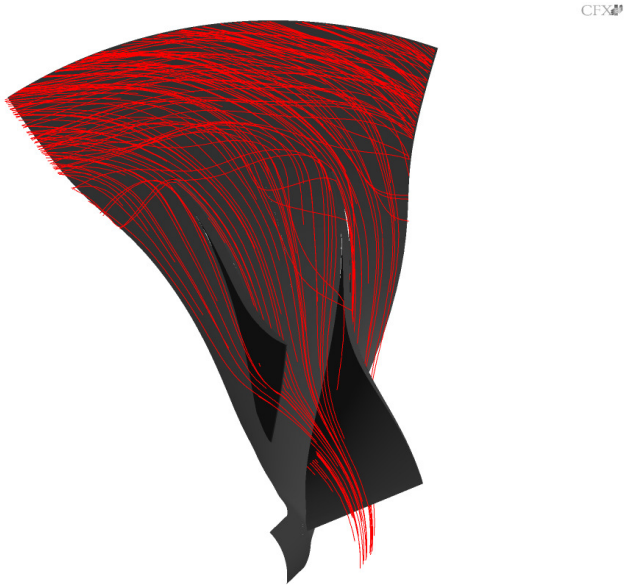

Fig. 4.1.4.4: Streamlines in Relative Frame of Reference (50% Span)

To avoid numerical instabilities at the outlet of the impeller an additional domain would be helpful. With such a domain the diffuser section of the compressor is then modeled and implemented in the stationary frame of reference to avoid small angles causing numerical uncertainty.

Mass Imbalance:

A very important information about convergence of the numerical solution is the mass imbalance between inlet and outlet of the domain. In industrial environment a mass imbalance of more than 0.1% is inacceptable. The mass imbalance of the stationary solutions in the present work is representatively illustrated below and is of the order of 10^{-6}:

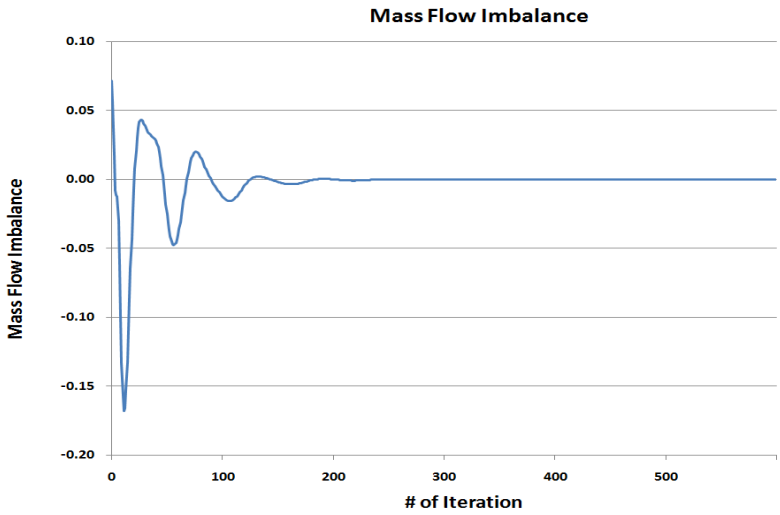

Fig. 4.1.4.5: Mass Flow Imbalance

4.1.5 Validation

A common method to illustrate the performance of a compressor is the well known compressor map. Plotting the pressure ratio versus mass flow for both the test rig and the computational model allows a validation of the CFD results:

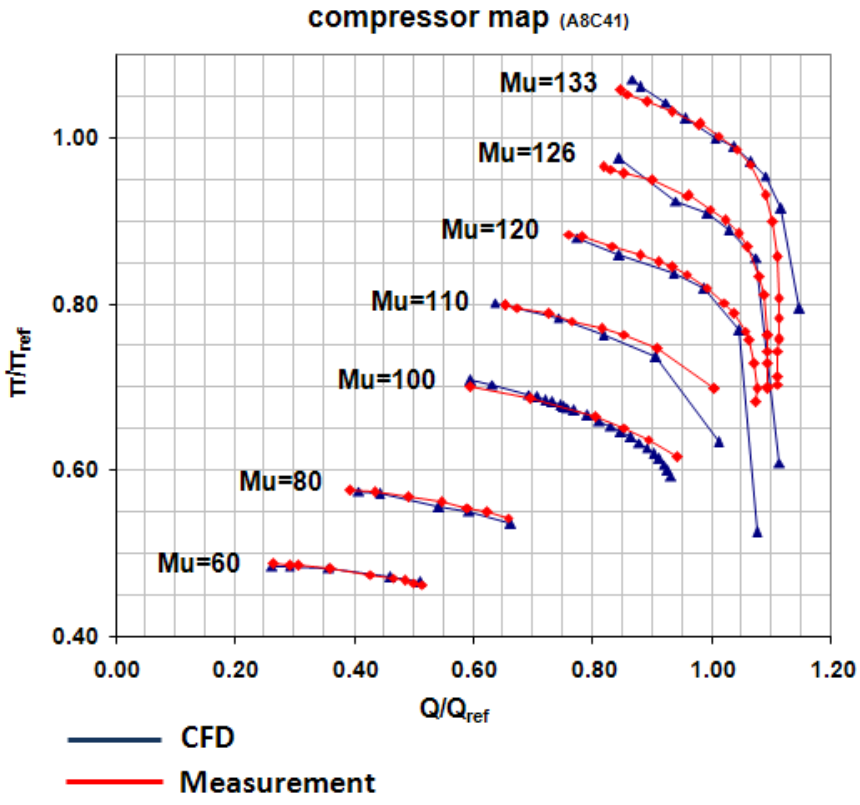

Fig. 4.1.5.1: Compressor Map

The compressor map above shows a good match of the numerical results compared to the measurements over the whole operating range. The values along the resistance line are to handle with care due to the fact that the CFD model doesn't reproduce the whole system.

A short explanation might be necessary concerning the pressure ratio π in the compressor map. The schematic below explains where the different pressures are measured in the rig and where the computational domain ends:

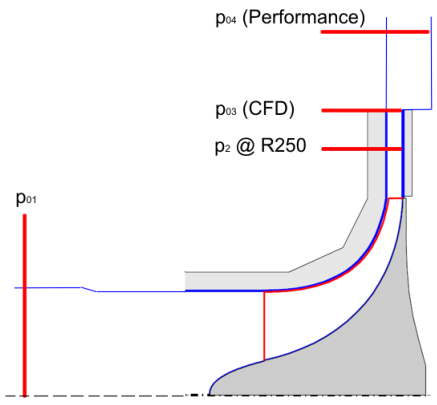

Fig. 4.1.5.2: Schematic of RIGI Test Rig

It is obvious that the total pressure ratios of test rig and CFD model can not be compared because of the different location of the exit total pressures p_{03} (CFD) and p_{04} (performance measurement of the rig). To get a proper pressure ratio to compare the two systems the values of static pressure, p_2, at radius 250mm, are used to build the pressure ratios π both for the measurements and the CFD results.
The total pressure ratio of the performance measurement of the test rig is scaled as follows:

$$\left(\frac{p_{04}}{p_{01}}\right) \cdot \left(\frac{p_2}{p_{04}}\right) = \left(\frac{p_2}{p_{01}}\right)_{measurement}$$

Equation 4.1.5.3

The same procedure is applied to the total pressure ratio of the CFD model:

$$\left(\frac{p_{03}}{p_{01}}\right) \cdot \left(\frac{p_2}{p_{03}}\right) = \left(\frac{p_2}{p_{01}}\right)_{CFD}$$

Equation 4.1.5.4

The measurement of static wall pressure p_2 was done by Matthias Schleer. Values are available for several stage Mach numbers but not for Mu=1.26 and Mu=1.33. By plotting the pressure correction coefficient $\left(\frac{p_2}{p_{0,\,exit}}\right)$ for both the measurements and the CFD results an estimate can be done for Mu=1.26 and Mu=1.33:

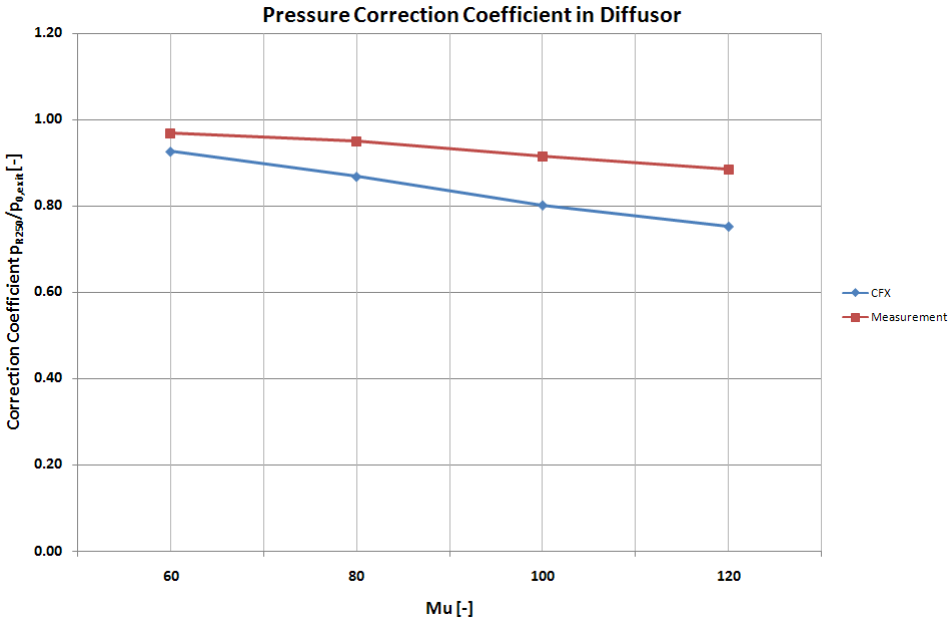

Fig. 4.1.5.5: Pressure Correction Coefficient

Due to the almost linear trend the values for Mu=1.26 and Mu=1.33 are extrapolated and assumed to be a good approximation.
The reference operating point is set at a corrected mass flow of Q=82.5 at Mu=1.33. The corresponding pressure ratio π_{ref} is 2.85.

Hub to Shroud Profiles:

The accomplishment of FRAP measurements in the diffuser section of the test rig at radius 210mm allows a comparison of the hub to shroud profiles for both the total pressure and absolute flow angle α_2 and offers a detailed validation of the numerical results. The operating points which are used to compare the profiles are indicated in the map below:

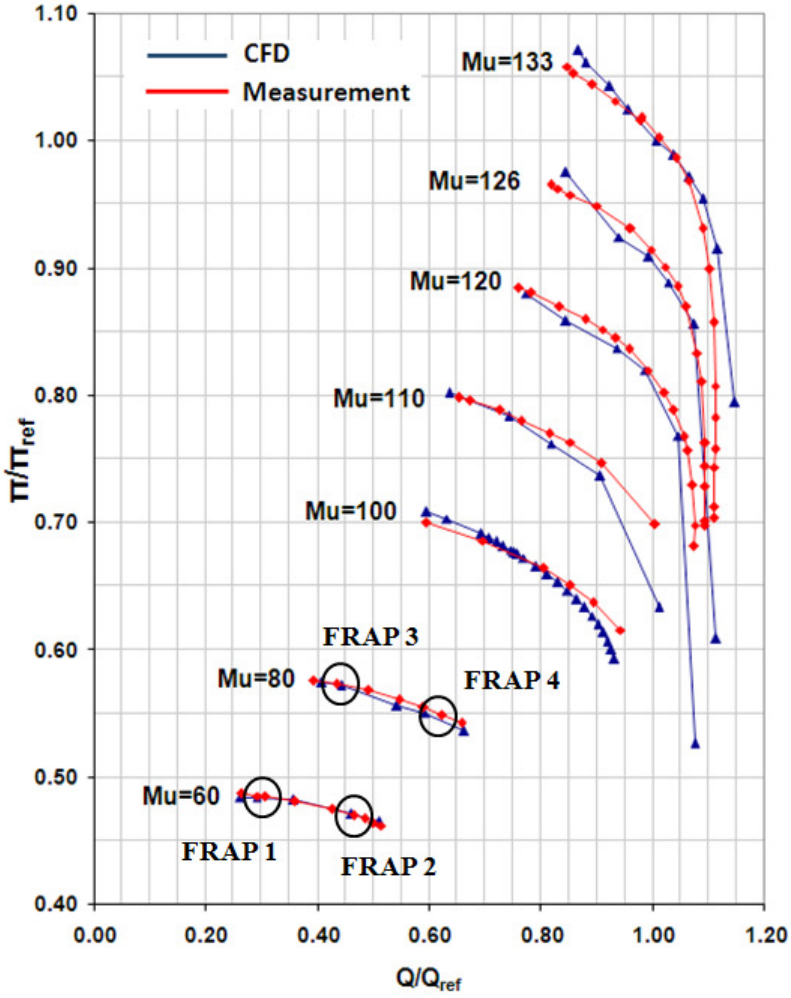

Fig. 4.1.5.6: Compressor Map: FRAP measurement points in Diffuser

The attentive reader might ask why there are no points to compare the profiles above a stage Mach number of Mu= 0.8. The reason is the missing probe calibration to evaluate the measured data at Mach numbers of about 0.8 at the measurement location. Furthermore the measurements have to be handled carefully at an operating point with a stage Mach number of Mu=1.0. The highly fluctuating flow conditions and temperatures of about 90°C which influence accuracy of the measurement.

The absolute total pressure ratio profiles for the indicated operating points confirm the consistence in performance of the numerical model with the test rig:

FRAP 1: Mu=0.6, Q/Q_{ref}=0.27

FRAP 3: Mu=0.8, Q/Q_{ref}=0.40

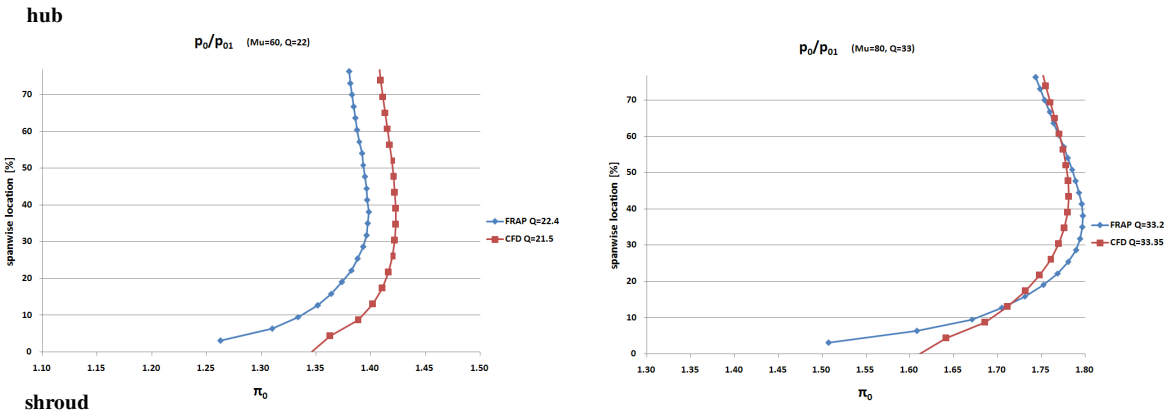

FRAP 2: Mu=0.6, Q/Q_{ref}=0.50

FRAP 4: Mu=0.8, Q/Q_{ref}=0.58

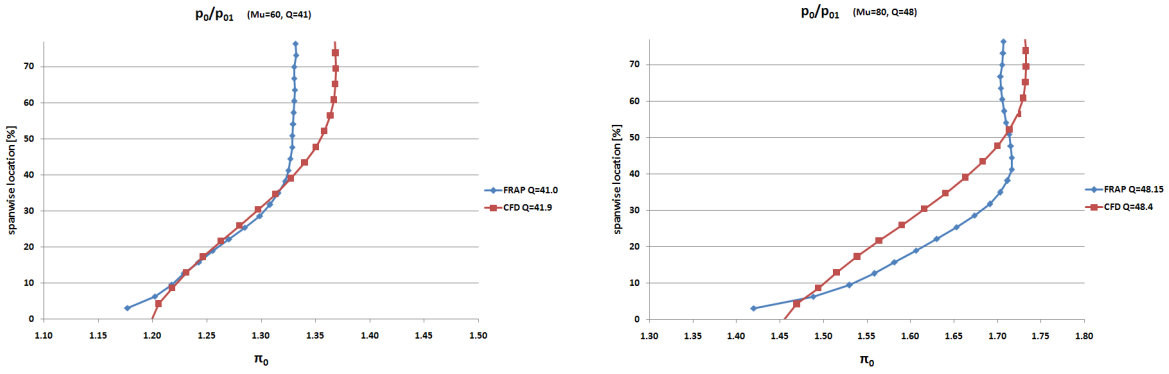

Fig. 4.1.5.7: Total Pressure Profiles at R=210mm

For the absolute flow angle comparison the definition of the angle α_2 is explained below:

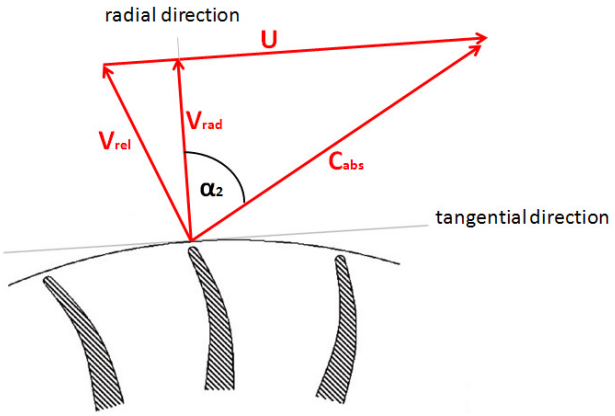

Fig. 4.1.5.8: Definition of Absolute Flow Angle at Exit

FRAP 1: Mu=0.6, Q/Q_{ref}=0.27

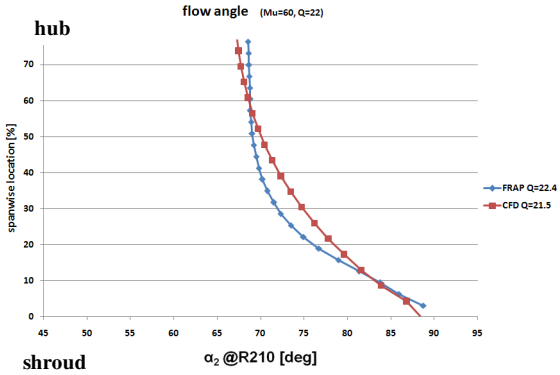

FRAP 3: Mu=0.8, Q/Q_{ref}=0.40

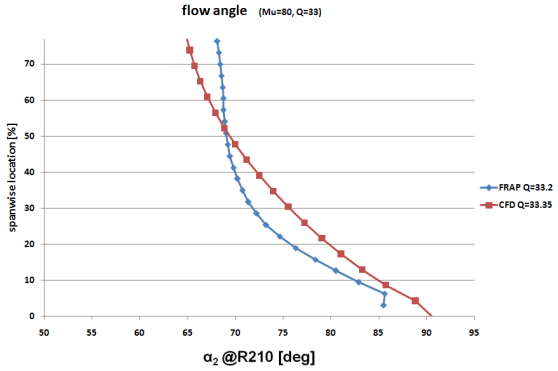

FRAP 2: Mu=0.6, Q/Q_{ref}=0.50

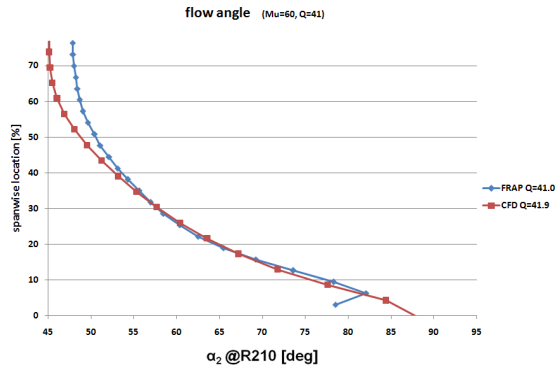

FRAP 4: Mu=0.8, Q/Q_{ref}=0.58

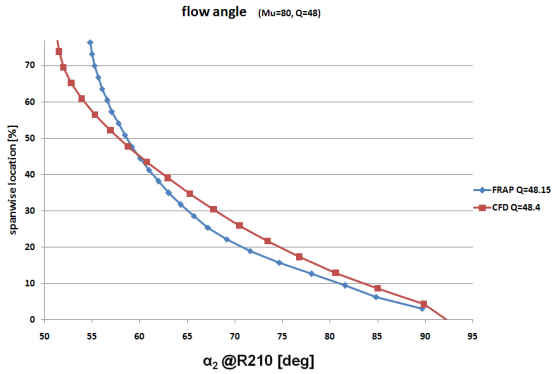

Fig. 4.1.5.9: Absolute Flow Angle Profiles at R=210mm

The profiles, both the total pressure profile as well as the absolute flow angle distribution, show good consistence of the CFD results compared to the measurements. The relative deviation of the total pressure profile of the order of 2% corresponds to the difference in performance (compressor map).

For both the stage Mach numbers Mu=0.6 and Mu=0.8 the total pressure ratio profiles at radius R=210mm over one pitch (main blade to main blade) are compared with FRAP measurements:

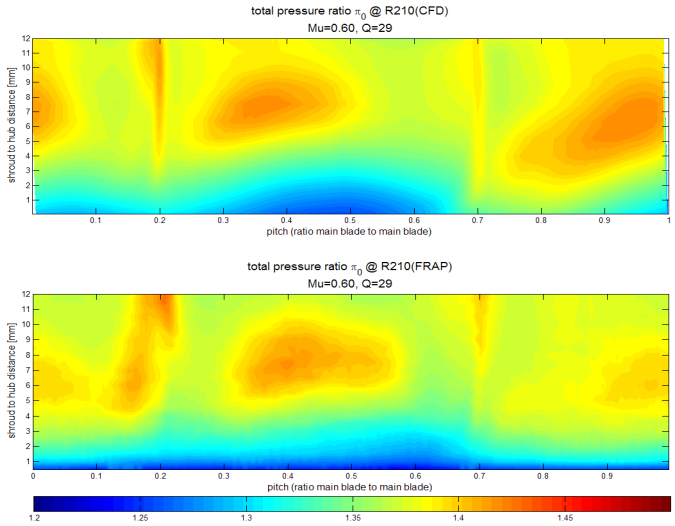

Fig. 4.1.5.10: Total Pressure Ratio at R=210mm (Mu=0.6, Q=29)

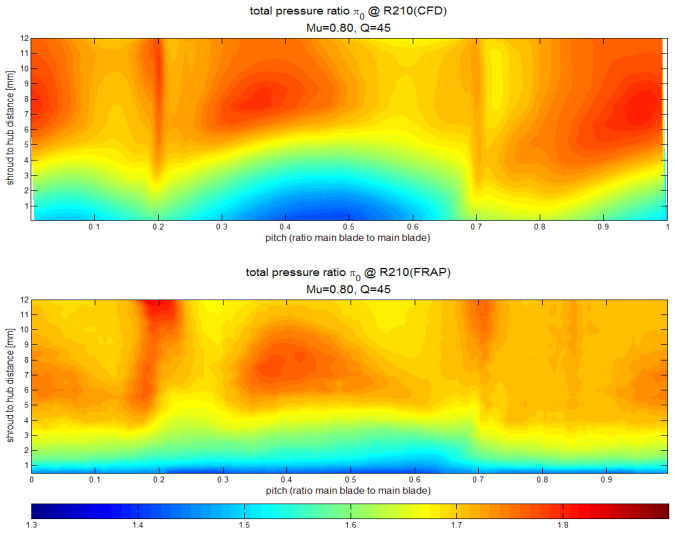

Fig. 4.1.5.11: Total Pressure Ratio at R=210mm (Mu=0.8, Q=45)

The contours show the total pressure ratio on a plane at constant radius in the diffuser part of the compressor. On the left the main blade jet is clearly visible. The jet region of the splitter blade can be identified at the right. The low total pressure ratios at the bottom of the contours show the boundary layer at the shroud.

The total pressure ratios show good consistence between CFD model and FRAP measurement. A major difference in both CFD profiles compared to the measured values is the vortical structure caused by the tip leakage fluid flow. The regions with very low total pressure (blue zones) develop stronger in the CFD contour compared to the FRAP data. On the one hand it might be that the numerical solution overpredicts the total pressure loss in the tip leakage vortex. On the other hand it is possible that the FRAP measurement underpredicts the total pressure loss in such highly fluctuating regions due to the strong variation in the fluid flow angle.

The detailed validation of the CFD results on the basis of steady state computations is required for the application of the model in transient investigations where measurement data is not available to compare the performance with the test rig behavior.

4.1.6 Flow through Impeller

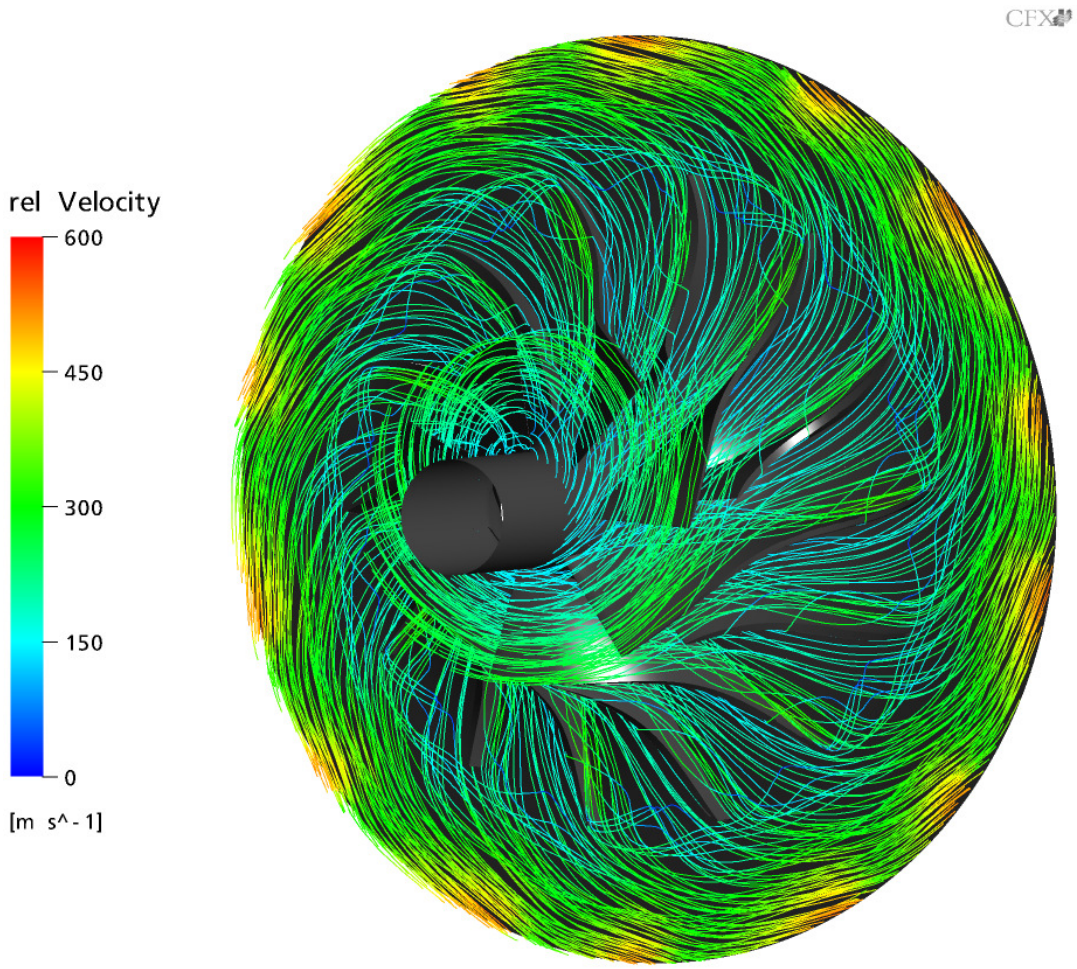

Fig. 4.1.6.1: Streamlines through Impeller (Velocity in rel. Frame of Reference)

The intention of this chapter is to characterize the flow through the centrifugal impeller and to compare several parameters at different operating points. As representatively illustrated in the figure above the flow through a centrifugal compressor is highly complex and it is therefore difficult to present an all- embracing characterization of the fluid dynamic phenomena taking place in such a device. In a first part the focus of the description concentrates on the compressor blade as it is one of the principal items of the impeller. In a second part the flow field is visualized by absolute and relative Mach numbers. A separate view addresses the tip leakage vortex.

Pressure Distribution on Main Blade Surface:

The figures below show the variation of the blade pressure distribution for both the pressure and suction side at a constant mass flow but for different impeller speeds. The pressures are nondimensionalized by the inlet static pressure p_1 :

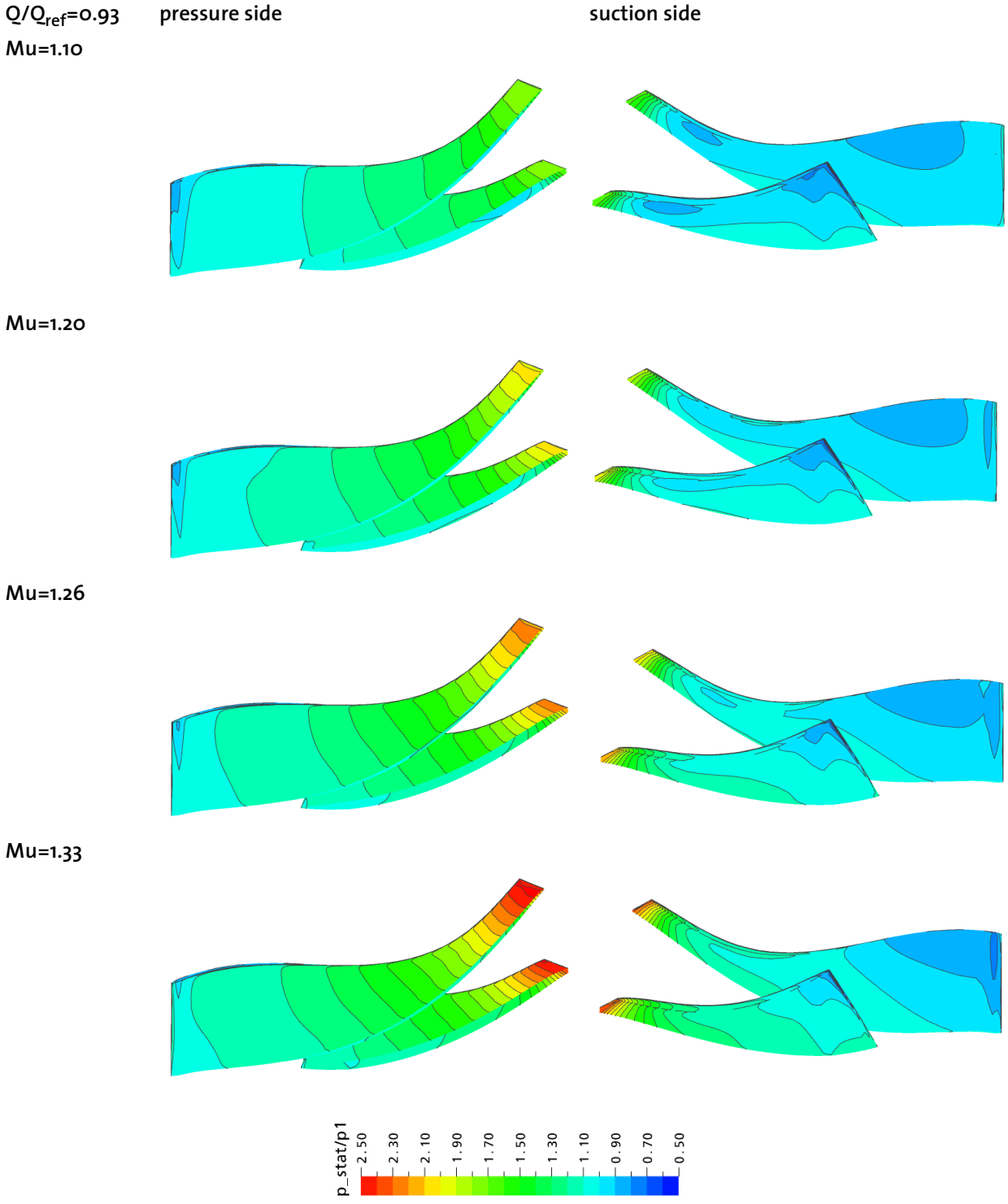

Fig. 4.1.6.2: Pressure Distribution on Impeller Blade

The comparison shows the effect of incidence at the leading edge of the blades. By increasing the blade speed at a constant mass flow the incidence increases. Therefore the region of low static pressure coefficient visible on the suction side of the mainblade travels towards leading edge. The loading increases with rising blade speed. To get a more detailed picture of the static pressure coefficient the values at mid height of the main blade from leading to trailing edge are compared in the following plot:

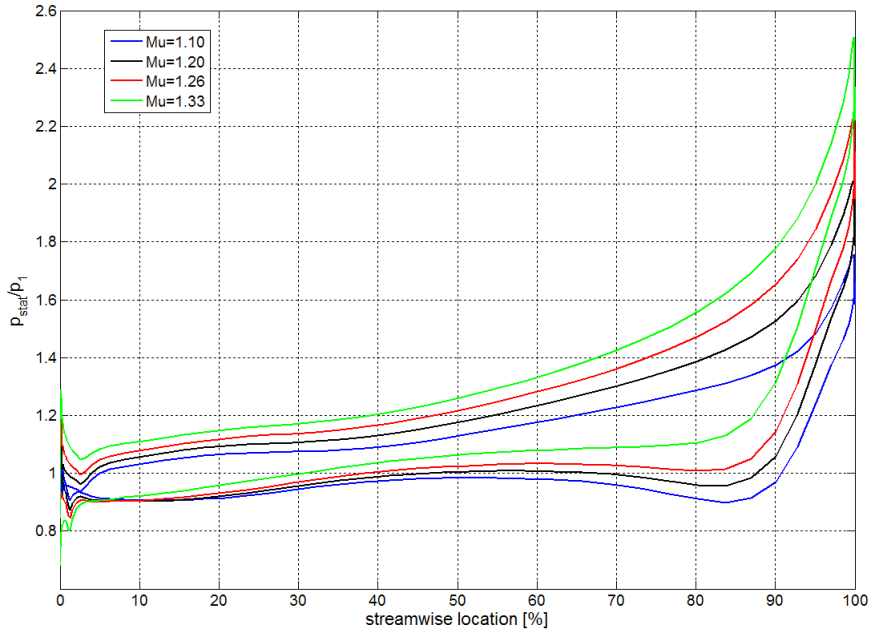

Fig. 4.1.6.3: Static Pressure Coefficient at 50% Span of Mainblade (Q/Q_{ref}=0.93)

In order to prove the statement that the loading increases with higher blade speed the loading coefficient $C_n = \frac{(p_{PS} - p_{SS})}{\rho \cdot w^2_{mean}}$ according to Schleer (Schleer et al., 2003) is plotted, again at mid height on the main blade from leading to trailing edge:

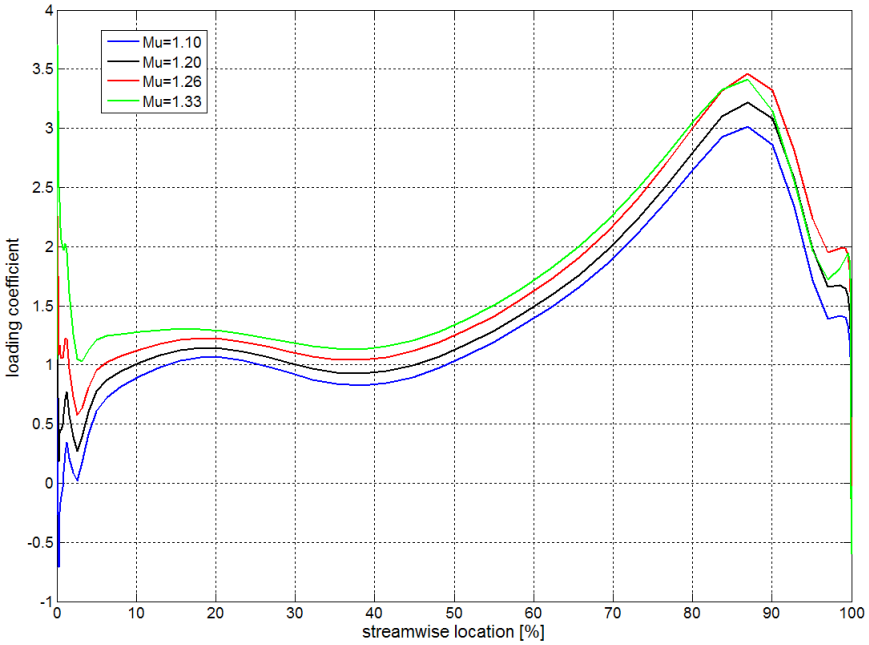

Fig. 4.1.6.4: Blade Loading Coefficient at 50% Span of Mainblade (Q/Q_{ref}=0.93)

An other approach to characterize the pressure distribution is to compare operating points along constant speed lines in the compressor map:

Mu=0.60:

Pressure Distribution:

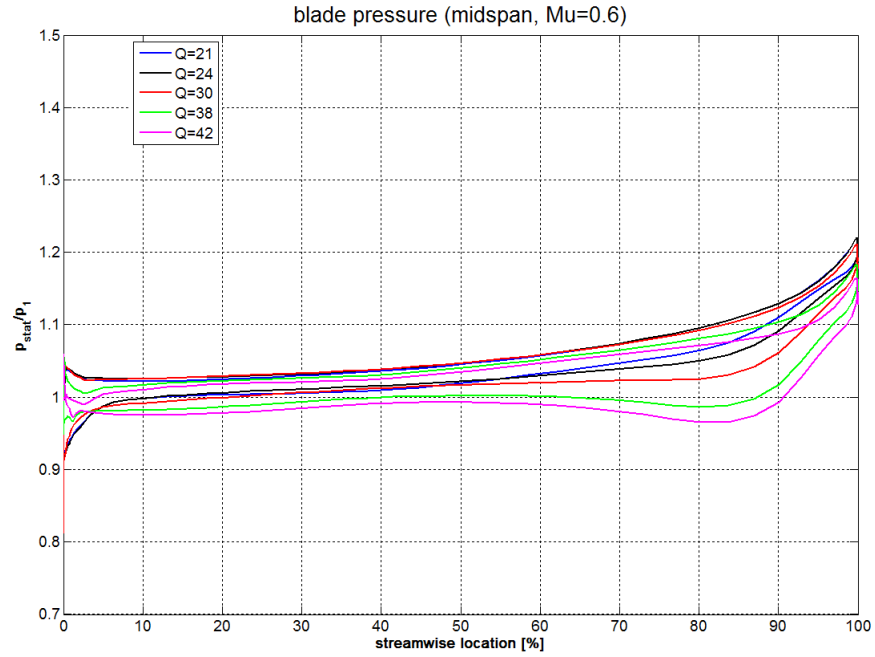

Fig. 4.1.6.5: Pressure Distribution on Mainblade at 50% Span (Mu=0.60)

Loading:

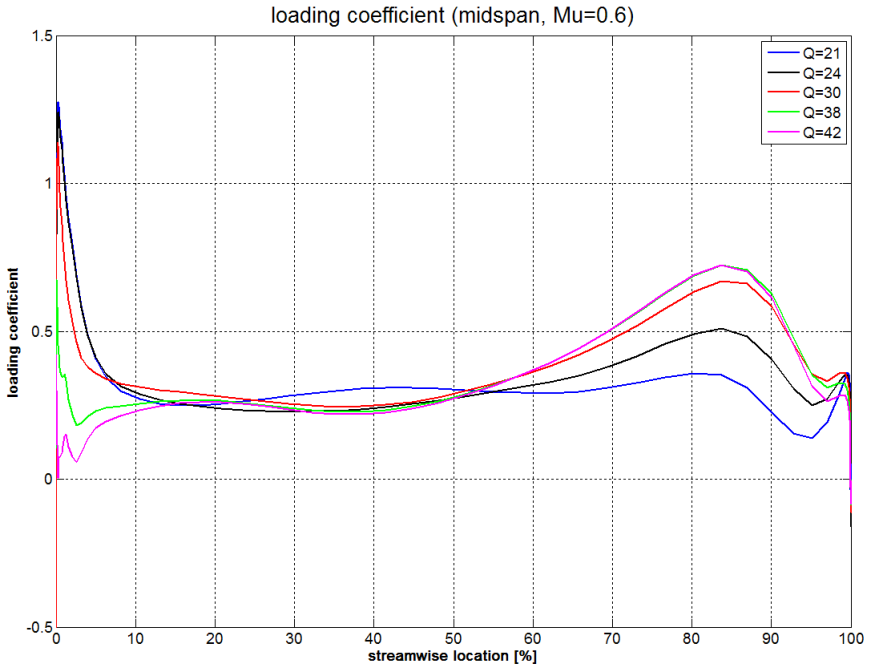

Fig. 4.1.6.6: Loading Coefficient on Mainblade at 50% Span (Mu=0.60)

Mu=0.80:

Pressure Distribution:

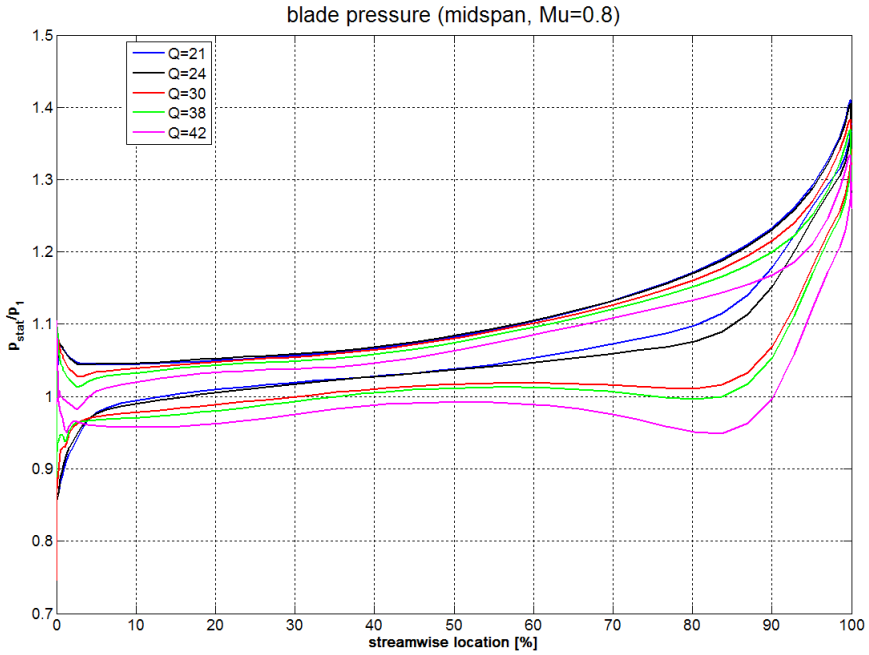

Fig. 4.1.6.7: Pressure Distribution on Mainblade at 50% Span

Loading:

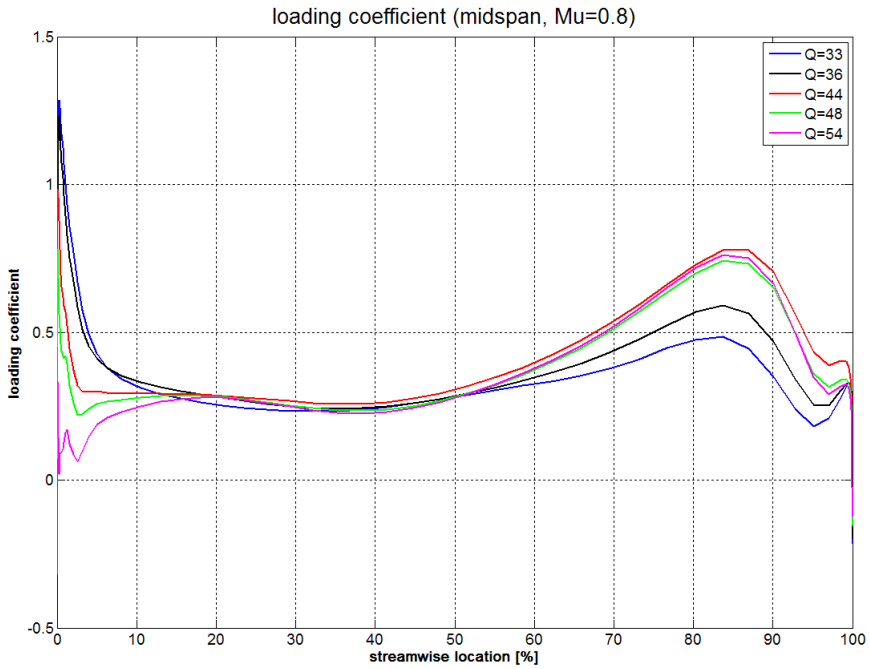

Fig. 4.1.6.8: Loading Coefficient on Mainblade at 50% Span (Mu=0.80)

Mu=1.20:

Pressure Distribution:

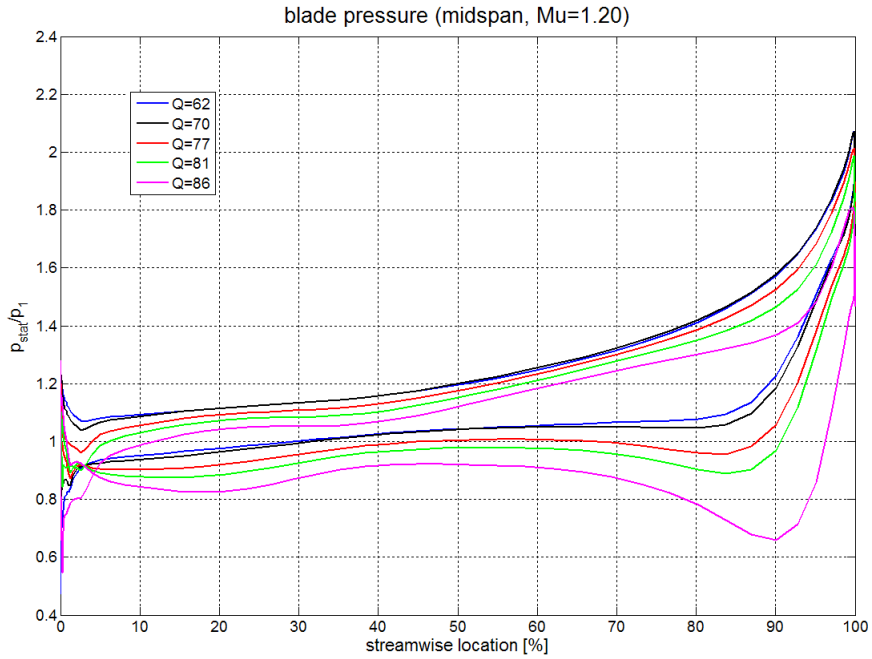

Fig. 4.1.6.9: Pressure Distribution on Mainblade at 50% Span (Mu=1.20)

Loading:

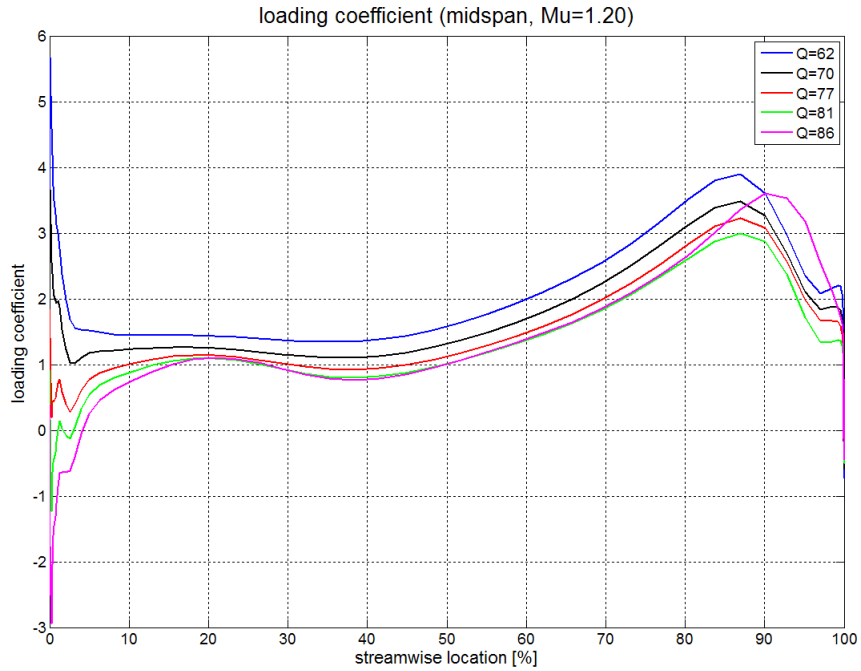

Fig. 4.1.6.10: Loading Coefficient on Mainblade at 50% Span (Mu=1.20)

For all the tree speed lines the pressure coefficient drops with increasing mass flow, especially on the suction side of the mainblade in the rear part. The loading coefficient therefore increases for higher mass flow rates.

If we now plot the inlet flow angle and compare the value with the metal angle of the mainblade one can see that for most of the corrected mass flow range there is negative incidence, excepting corrected mass flow rates below about Q=64, which reduces the risk of separation on the suction side:

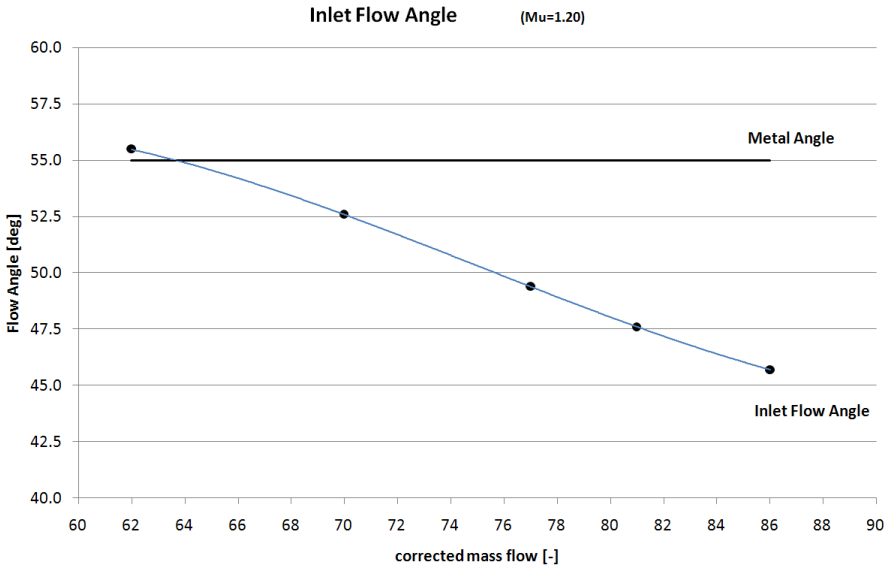

Fig. 4.1.6.11: Absolute Inlet Flow Angle (Mu=1.20)

An important information for the currently planned measurements of the time resolved blade pressure with pressure transducers on the mainblade of the impeller in the RIGI test rig is the pressure gradient. The decision for the positioning of the transducers might be affected by the local pressure gradient on the blade surface. The following curves representatively show the pressure gradient in streamwise direction on the mainblade surface at 50% span from leading to trailing edge for a stage Mach number of Mu=1.00 and a mass flow rate of Q/Q_{ref}=0.75:

pressure side:

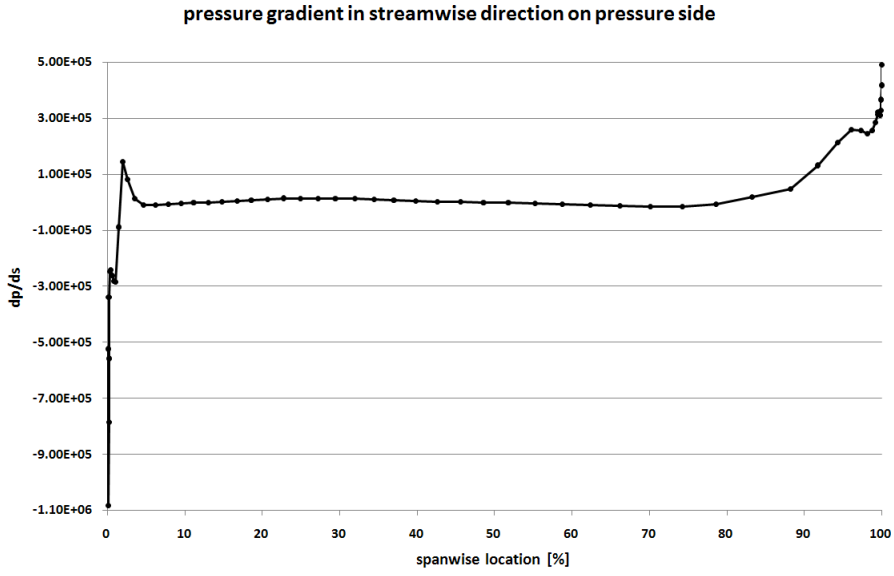

Fig. 4.1.6.12: Pressure Gradient on Pressure Side of Mainblade at 50% Span

suction side:

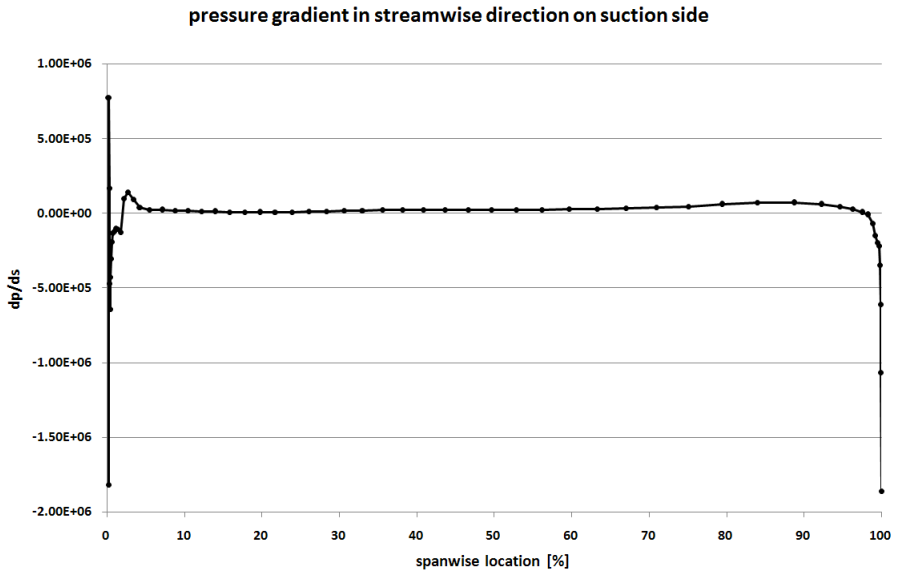

Fig. 4.1.6.13: Pressure Gradient on Suction Side of Mainblade at 50% Span

The run of the curves show that one is almost free concerning the choice of location for the pressure probes along the blade surface (except regions near the leading and trailing edge) due to the nearly constant gradient $\frac{\partial p}{\partial s}$ in streamwise direction.

Mach Numbers:

In order to get a general description of the flow conditions through the impeller the Mach numbers, both the absolute and relative, are plotted on a surface at constant 50% span. In the diffuser section a plane at constant radius of R=210mm is displayed to indicate the Mach numbers to determine the required calibration range for the probes for intended FRAP measurements in the near future in the diffuser section.

Mu=0.60, Q/Q_{ref}=0.36:

Ma_{abs}:

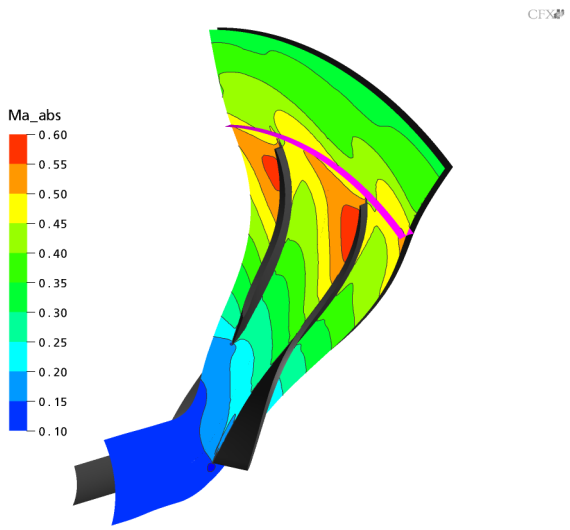

Fig. 4.1.6.14: Absolute Ma (Mu=0.60, Q/Q_{ref}=0.36)

Ma_{rel}:

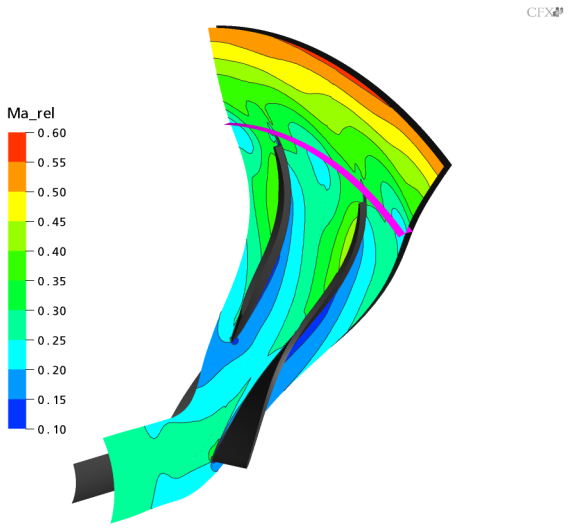

Fig. 4.1.6.15: Relative Ma (Mu=0.60, Q/Q_{ref}=0.36)

Mu=0.80, Q/Q_{ref}=0.53:

Ma_{abs}:

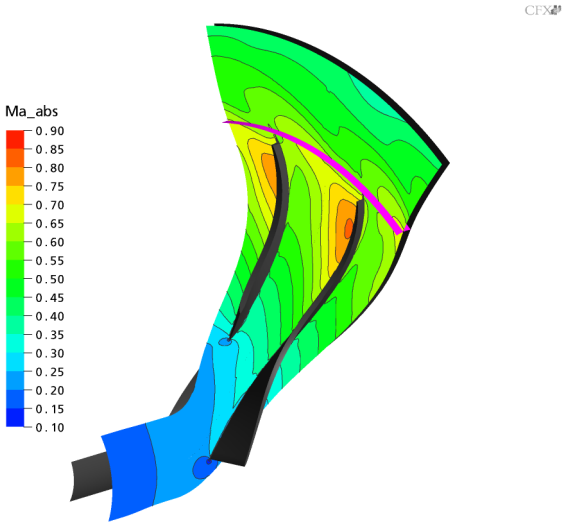

Fig. 4.1.6.16: Absolute Ma (Mu=0.80, Q/Q_{ref}=0.53)

Ma_{rel}:

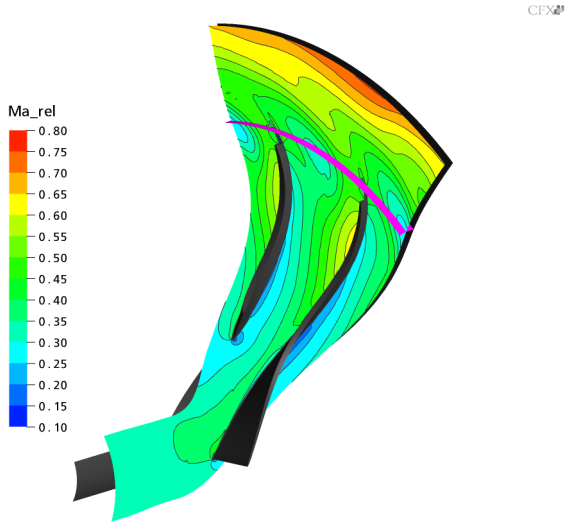

Fig. 4.1.6.17: Relative Ma (Mu=0.80, Q/Q_{ref}=0.53)

Mu=1.00, Q/Q_{ref}=0.79:

Ma_{abs}:

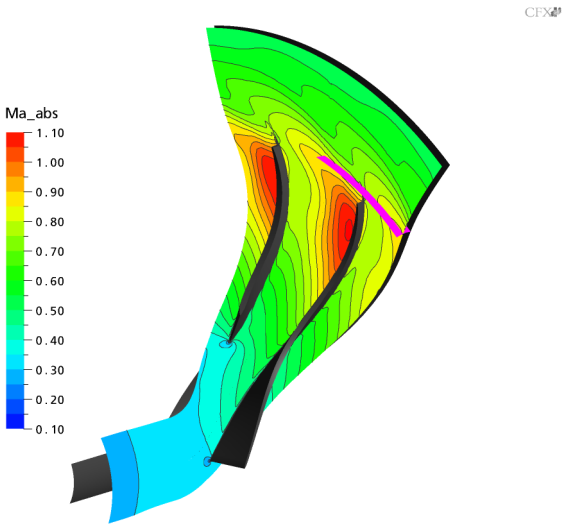

Fig. 4.1.6.18: Absolute Ma (Mu=1.00, Q/Q_{ref}=0.79)

Ma_{rel}:

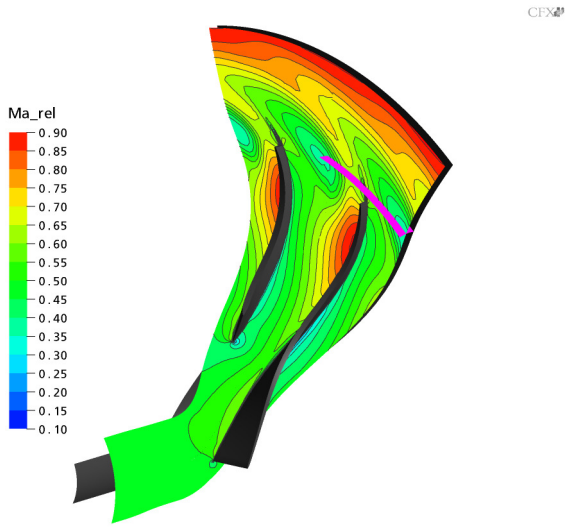

Fig. 4.1.6.19: Relative Ma (Mu=1.00, Q/Q_{ref}=0.79)

Mu=1.10, Q/Q_{ref}=0.93:

Ma_{abs}:

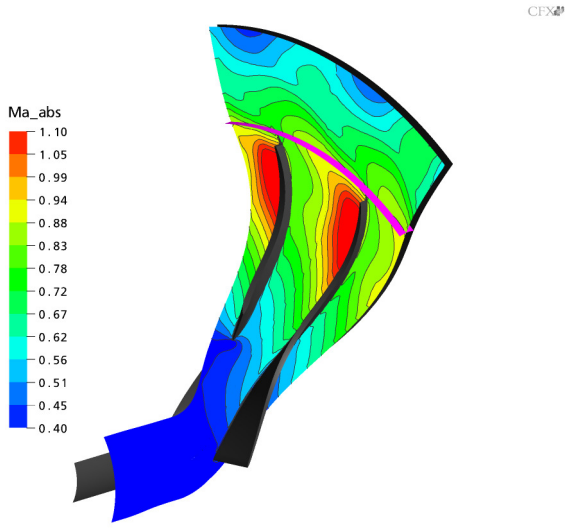

Fig. 4.1.6.20: Absolute Ma (Mu=1.10, Q/Q_{ref}=0.93)

Ma_{rel}:

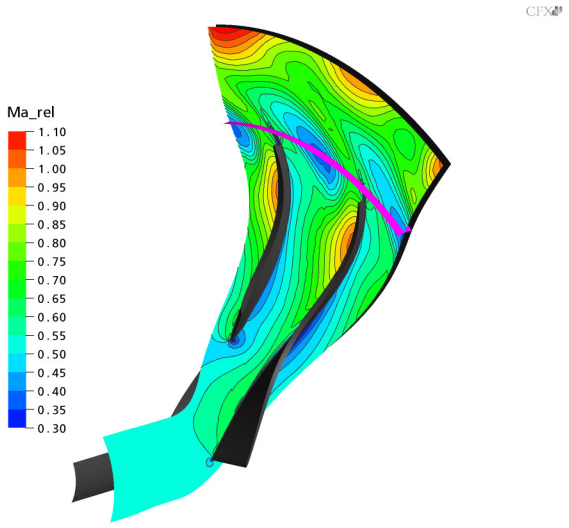

Fig. 4.1.6.21: Relative Ma (Mu=1.10, Q/Q_{ref}=0.93)

The table below shows the mass averaged quantities at the R210 surface:

	$\overline{Ma_{abs}}$	$\overline{T_0}$	$\overline{\alpha_2}$
Mu=1.10, Q/Q_{ref}=0.93	0.835	401.62 K	46.08°
Mu=1.00, Q/Q_{ref}=0.79	0.791	364.14 K	44.65°
Mu=0.80, Q/Q_{ref}=0.53	0.597	350.68 K	44.03°
Mu=0.60, Q/Q_{ref}=0.36	0.448	328.06 K	42.34°

Due to the fact that the calibration facility for the FRAP probes is limited to a Mach number calibration of 0.7 measurements in the diffuser section can only be done up to a stage Mach number of about Mu=0.90. The temperature limit of the probes lies in the region of about 390K to 400K and is therefore not the limiting factor.

A noticeable feature visible in all plots for the Mach number in the relative frame of reference is a zone of lower relative Mach number at the exit of the blading. The origin of this feature can be found by tracking the tip leakage vortex.

Tip Leakage Vortex:

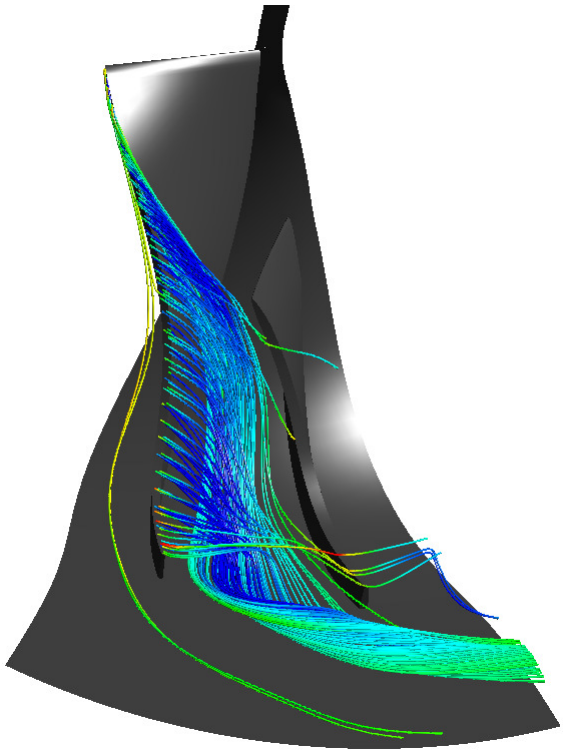

Fig. 4.1.6.22: Tip Gap Vortex (Streamlines, Mu=1.33, Q/Q_{ref}=1.0)

Corresponding to Schleer (Schleer, 2006) the tip leakage vortex has a dominating effect on the formation of secondary flows in the diffuser. Instead of the classical jet- wake pattern the proposed 3- zone flow model holds for the investigated impeller with a tip clearance ratio $CR = \frac{t}{b_2}$ of about 4.1%.

A series of illustrations characterizes in a qualitative point of view the modification of the vortical structure for a stage Mach number of Mu=1.33 at different mass flow rates:

Q/Q_{ref}=0.87 Q/Q_{ref}=0.95 Q/Q_{ref}=1.03

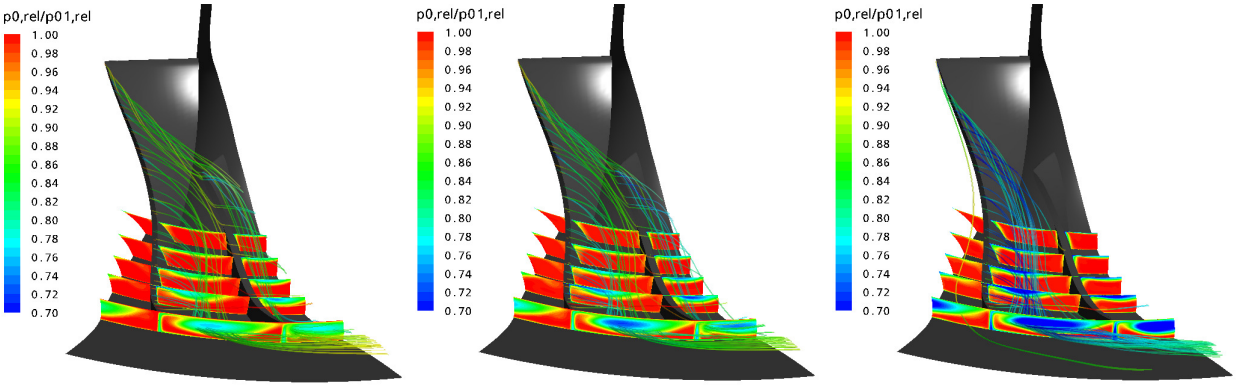

Fig. 4.1.6.23: Tip Gap Vortex (Streamlines, relative Total Pressure Ratio, Mu=1.33)

The location of the tip leakage vortex core does not change significantly by varying the mass flow rate but the relative total pressure loss gets stronger with increased mass flow and the amount of flow passing in front of the leading edge of the splitter blade decreases strongly for higher mass flow rates.

To underline the statement of stronger vortical structure with increasing mass flow, profiles at the exit of the impeller show relative total pressure ratio for the operating points illustrated previously:

Q/Q_{ref}=0.87

Q/Q_{ref}=0.95

Q/Q_{ref}=1.03

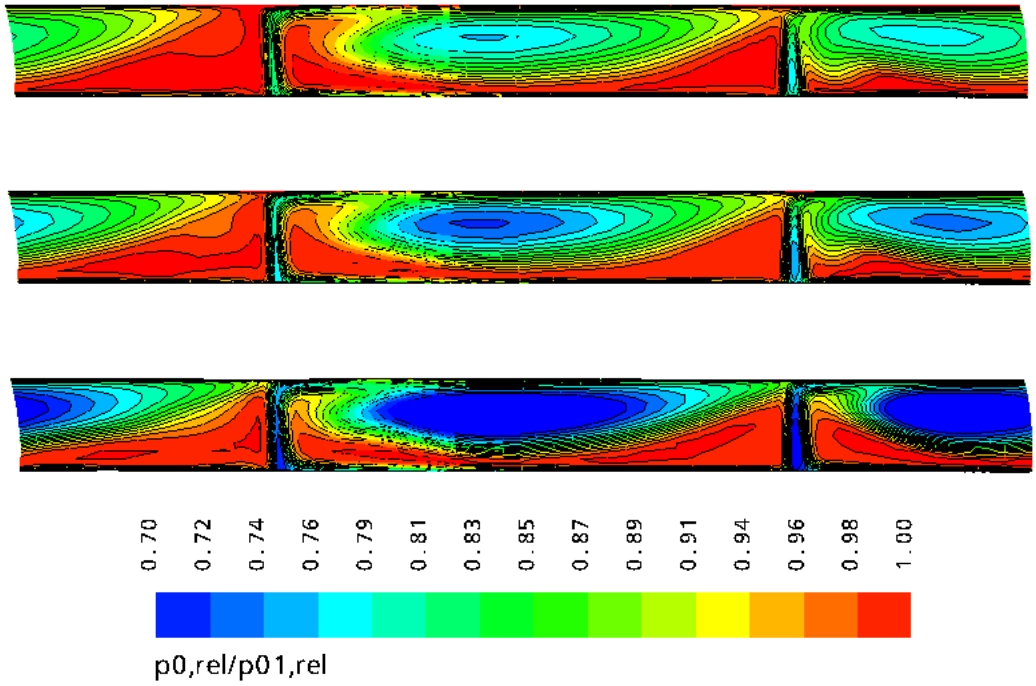

Fig. 4.1.6.24: Relative Total Pressure Ratio (Mu=1.33, impeller exit, mainblade left, splitterblade right, turning: right to left)

To indicate the influence of blade speed on tip leakage vortex the streamlines are plotted for the same mass flow rate of Q/Q_{ref}=0.93 but for different impeller speeds:

Mu=1.20 Mu=1.26 Mu=1.33

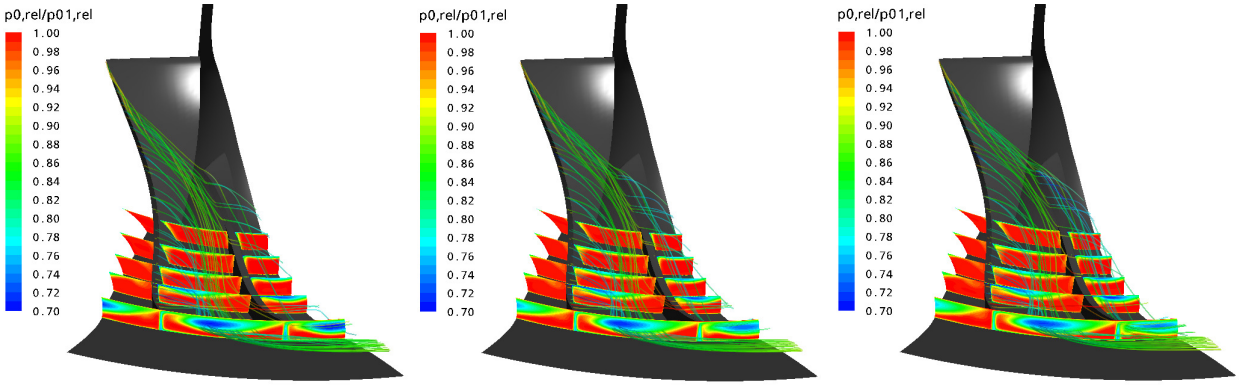

Fig. 4.1.6.25: Tip Gap Vortex (Streamlines, relative Total Pressure Ratio, Q/Q_{ref}=0.93)

With increased blade speed but constant corrected mass flow rate the amount of mass passing in front of the leading edge of the splitter blade increases whereby the extension of the tip gap vortex through the inter blade channel decreases.

A set of contour plots, again relative total pressure ratio at constant mass flow rate (Q/Q_{ref}=0.93), supports the statements above:

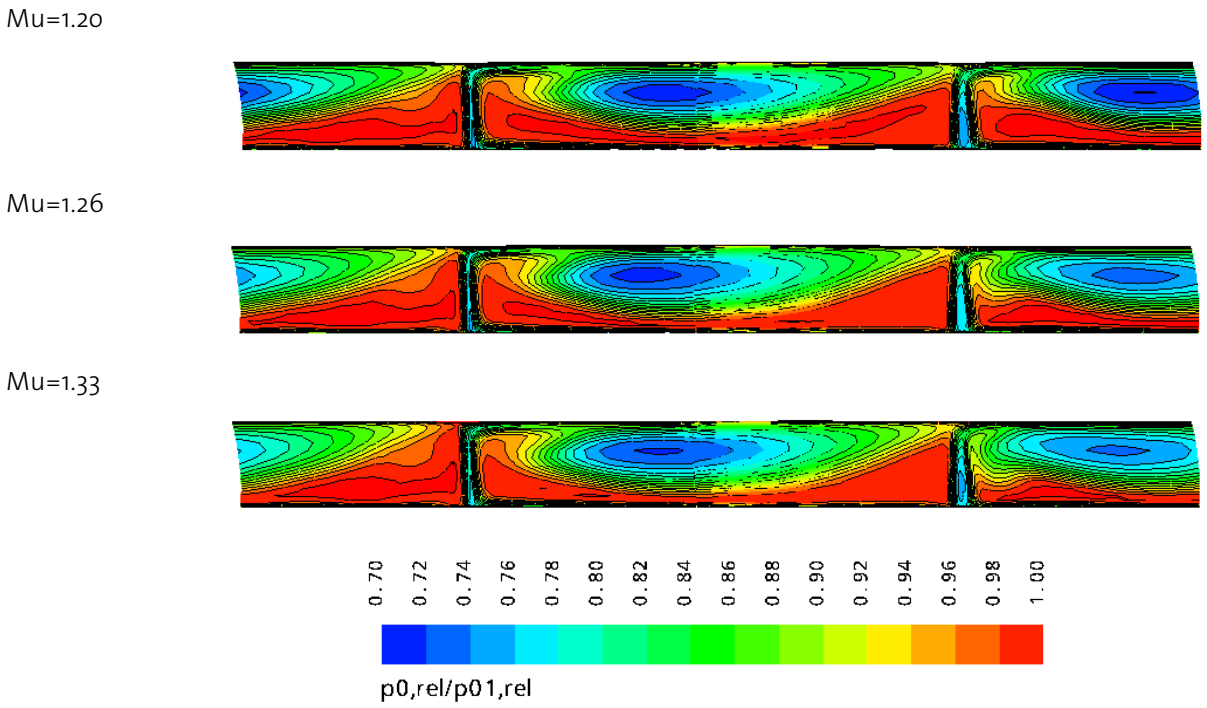

Fig. 4.1.6.26: Relative Total Pressure Ratio (Q/Q_{ref}=0.93, impeller exit, mainblade left, splitterblade right, turning: right to left)

The trend from Mu=1.20 to Mu=1.33 is obvious. The region of low relative total pressure ratio in the inter blade channel is decreasing. The vortex caused by fluid passing the shroud gap blocks a remarkable part of the channel. Due to the blockage effect of the vortical structure zones of higher relative total pressure ratios compensate in terms of mass flow conservation.

4.2 Transient CFD

In the second part of the present work the effect of inlet distortion in a centrifugal compressor is investigated. The flow field downstream the distortion generated by grids described in chapter 3.13 is measured using FRAP probes. The results of the measurement in the inlet section of the test rig are used as boundary condition for the CFD model. The unsteady CFD investigation of the centrifugal compressor provides information about the behavior of the distortion travelling through the impeller. As a source for the excitation of the impeller blades the time resolved pressure distribution on the blade surface is in the focus of the transient simulations.

4.2.1 Grid

Due to the applied distortion patterns the entire impeller grid is needed for the unsteady investigation. The impeller is implemented by simply completing the seventh part used for the steady state computations to the full 360 degrees:

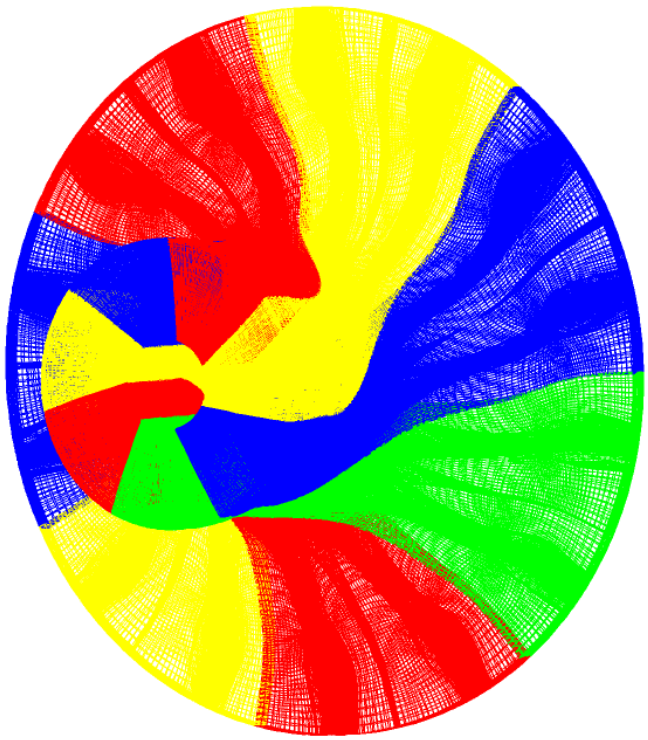

Fig. 4.2.1.1: CFD Grid (Entire Impeller)

The entire impeller grid consists of 4‘001‘200 nodes building 3‘564‘288 elements (hexahedra). A domain interface is defined in the inlet section to enable a stationary and a rotating domain due to the fact that the FRAP measured inlet boundary conditions are quantities in stationary frame of reference.

4.2.2 Boundary Conditions

The boundary conditions for the unsteady computations are equal to the steady state cases excepting the inlet boundary condition:

Inlet:	total pressure, total temperature and turbulence intensity profile (FRAP measurement)
Outlet:	static pressure (average static pressure, varied until mass flow matches measurement)
Shroud:	counter rotating wall, no slip, adiabatic
Impeller:	constant rotational speed, no slip, adiabatic

Inlet Boundary Condition Profiles:

The flow field in the inlet section of the test rig was measured with FRAP probes in a foregoing semester thesis. Due to the missing areas in the measurement plane because not accessible with the probe (white zones in the illustration below) and rudiments in the flow field of upstream installations additionally to the distortion screen (struts for the slip ring support needed for the strain gage signal transmission for example) the profiles for the CFD model are applied to the model in an idealized form which also simplifies the achievment of periodic convergency:

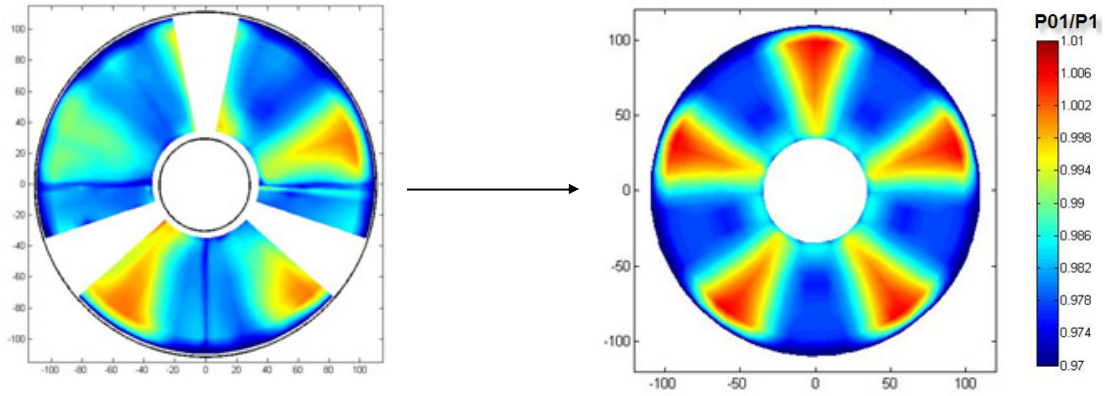

Fig. 4.2.2.1: Total Pressure Inlet Boundary Condition (Measured and Idealized) (A. Kammerer)

4.2.3 Turbulence Measurement

The performed measurements of the distorted inlet flow field with FRAP probes allow a Reynolds decomposition of the probe signal into a deterministic and a stochastic part:

$$g(t) = \tilde{g}(t) + g'(t)$$

Equation 4.2.3.1

The turbulent stresses are used to form the Reynolds stress tensor in terms of velocity fluctuations on the three spatial directions. According to Porreca (Porreca et al., 2006) the turbulence intensity is extracted from the time resolved measurements:

$$Tu = \sqrt{\frac{\overline{u'^2} + \overline{v'^2} + \overline{w'^2}}{3\tilde{c}^2}}$$

Equation 4.2.3.2

Two fundamental assumptions contained in the publication of Porreca (Porreca et al.) are not valid or can not be proved currently. On the one hand the assumption of a much smaller gradient of the fluctuating velocity component in streamwise direction compared to the other two directions to simplify the continuity equation can not be proved. A series of measurements at different streamwise positions would be needed to check for validity in an almost unaccelerated flow field.

On the other hand the continuity equation itself to integrate for the yaw component (only nonsimultanious measurement) may not be applicable due to the coarse measurement grid. It is improper to integrate for quantities with probably much smaller scales compared to the discretized spatial length scales of the measurement. A validation of the proposed procedure of Porreca (Porreca et al.) is done in an undistorted inlet flow field and points out the effect of the mentioned doubts:

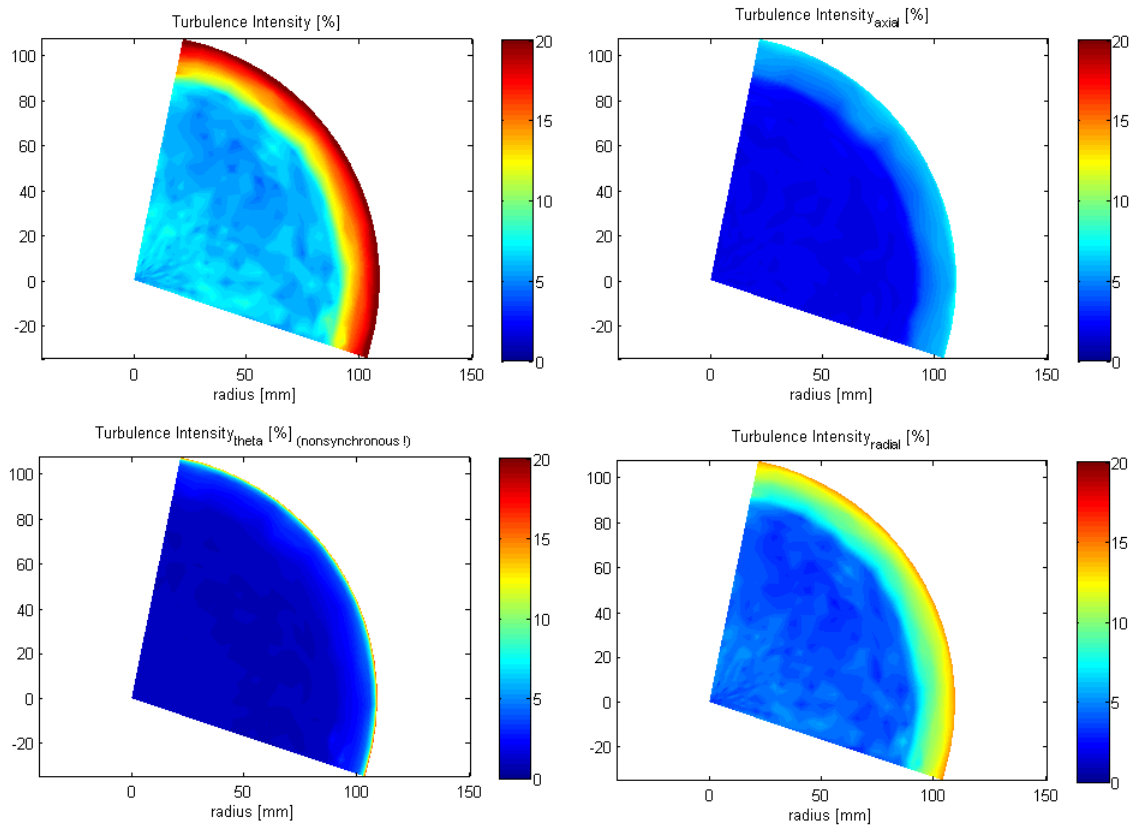

Fig. 4.2.3.3: Turbulence Intensities in Undistorted Flow Field

The turbulence intensities in the circumferential (theta) and the radial direction should have the same order of magnitude in the core of the flow field as a matter of course. The comparison of these two components shows a smoothing of the circumferential component. The value of turbulence intensity in the boundary layer is extremely high (might be an effect of probe geometry and/or pitch sensitivity) and therefore to handle with care.

The smoothing effect is quantified statistically via mean turbulence intensity and standard deviation for the present flow field:

	$\overline{Tu}$	$\pm\sqrt{Var}$
axial direction:	1.9682%	± 0.10677%
radial direction:	4.2675%	± 0.54887%
circumferential direction:	1.0785%	± 0.06243%

The statistical analysis shows a smoothing of the mean turbulence intensity by a factor of about 4 in circumferential direction compared to the radial component which is measured simultaneously and a reduction of the standard deviation by a factor of almost 9.

A refinement of the measurement points to allow the discrete integration of the continuity equation for a measurement plane of the order of $8 \cdot 10^{-3}\ \mathrm{m}^2$ is not recommended. The presented measurement of the undistorted flow field consists of about 800 measurement points. Therefore the Matlab post processing of the time resolved FRAP data requires about 100 CPU hours on a PC with an Intel "Conroe" processor.
Nevertheless, the turbulence intensity can be evaluated due to the particular measurement setup. By traversing the probe in circumferential direction in the measurement plane normal to the streamwise direction the probe fixed cylindrical coordinate system allows a simplification of the equation for the turbulence intensity. The equation for the turbulence intensity

$$Tu = \sqrt{\frac{1}{3}\left[\frac{1}{4}\left(\frac{\overline{p_1'^2}}{\tilde{p}_d^2}\right) + \left(\frac{\overline{v'^2}}{\tilde{c}^2}\right) + \overline{\beta'^2}\right]}$$

Equation 4.2.3.4

with p_1': aperiodic pressure (sensor 1)
$\tilde{p}_d$: deterministic pressure
$\tilde{c}$: deterministic absolute velocity
v': aperiodic velocity component in circumferential direction
and β': aperiodic pitch angle component

simplifies to

$$Tu^* = \sqrt{\frac{1}{3}\left[\frac{1}{4}\left(\frac{\overline{p_1'^2}}{\tilde{p}_d^2}\right) + 2 \cdot \overline{\beta'^2}\right]}$$

Equation 4.2.3.5

and is used to evaluate the FRAP measurements of the distorted inlet flow field of the compressor. The resulting turbulence intensity is then used as boundary condition at the inlet of the computational model additionally to the total pressure and total temperature profile.

The evaluation for one third of the inlet measurement plane in the test rig is presented below for a distortion screen to excite the 5. enginge order:

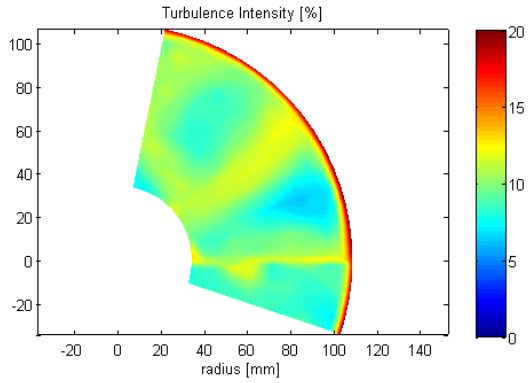

Fig. 4.2.3.6: Turbulence Intensity, Measurement Sector 1, 5. EO Screen

The idealized turbulence intensity profile (5. engine order excitation screen) is plotted below together with the total pressure profile:

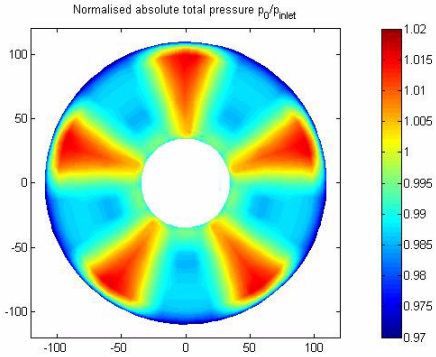

Fig. 4.2.3.7: Total Pressure Boundary Condition Profile (FRAP) (A. Kammerer)

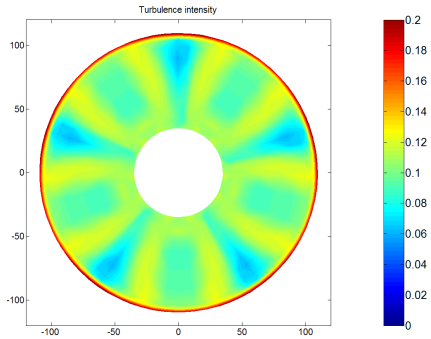

Fig. 4.2.3.8: Turbulence Intensity Boundary Condition Prof. (FRAP) (A. Kammerer)

The values at the measurement points are interpolated onto the grid nodes at the corresponding inlet surface of the computational domain. For the total temperature a constant value is used instead of a profile due to the negligible variation in the measured flow field:

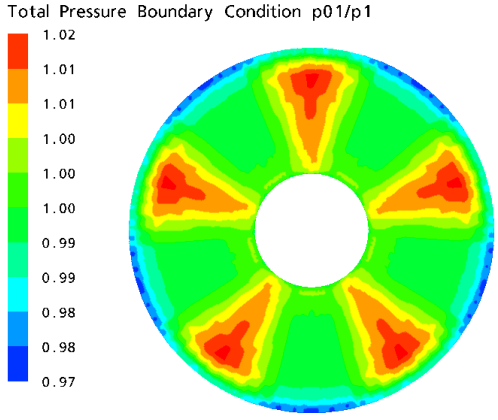

Fig. 4.2.3.9: Total Pressure Boundary Condition Profile (CFD)

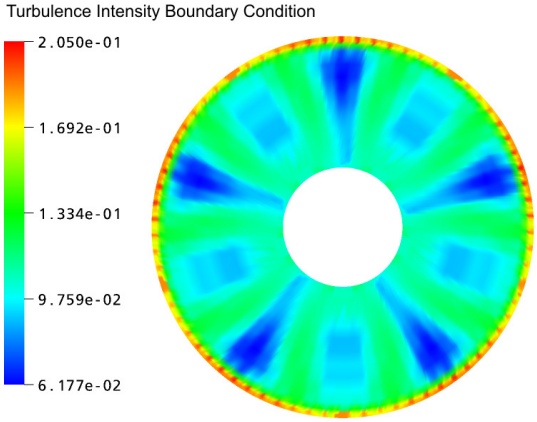

Fig. 4.2.3.10: Turbulence Intensity Boundary Condition Profile (CFD)

4.2.4 Turbulence Model and Solver Setup

As in the stationary case the $k-\varepsilon$ turbulence model is in use. In a first step an initial solution with a frozen rotor stator interface is required. The quasi steady state solution then accelerates the unsteady calculation with a transient rotor stator interface at the frame change interface. The physical time step setup is a trade-off between sampling rate of the unsteady flow properties and the computational effort. The size of the time step has to ensure a proper resolution of the periodic distortion pattern and is affected by the rotational speed of the impeller at the operating point under investigation due to a constant resolution of 77 physical impeller positions over a period of one revolution leading to 11 points between two adjacent main blades. The highest number of distortion baffles is five leading to a resolution of 15 to 16 points per distortion period at the inlet of the impeller which is high enough to record the distortion.

4.2.5 Operating Points for Transient CFD

To determine the operating points of interest for the transient investigations the Campbell diagram of the impeller main blade is required. The investigated resonance points of the main blade are marked with blue circles:

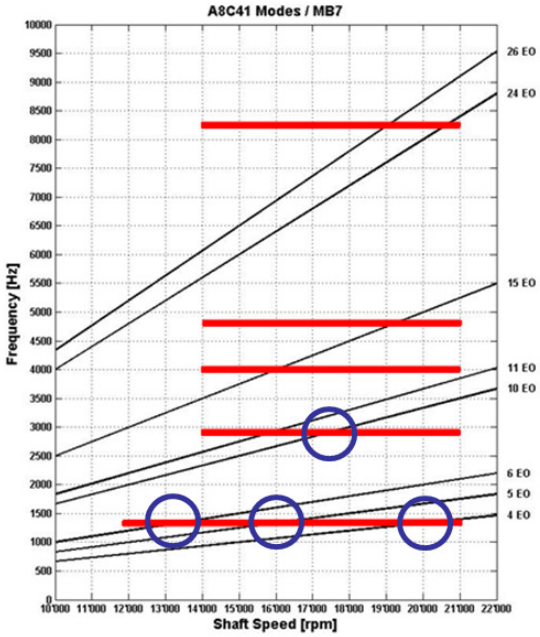

Fig. 4.2.5.1: Campbell Diagram Impeller Main Blade (A. Kammerer)

CFD simulations of the following combinations of inlet boundary conditions and rotational speeds have been done:

	13360 rpm	16250 rpm	17340 rpm	20700 rpm
idealized p_{01} boundary condition:	X	X	X	X
idealized p_{01} & Tu boundary condition:		X		
real p_{01} boundary condition:		X		

4.2.6 Convergence Quantification

Solver Residuals:

As for the steady state simulations the residuals are the most important measure of convergence. The RMS residuals below show representatively the order of magnitude of the residuals for the transient cases:

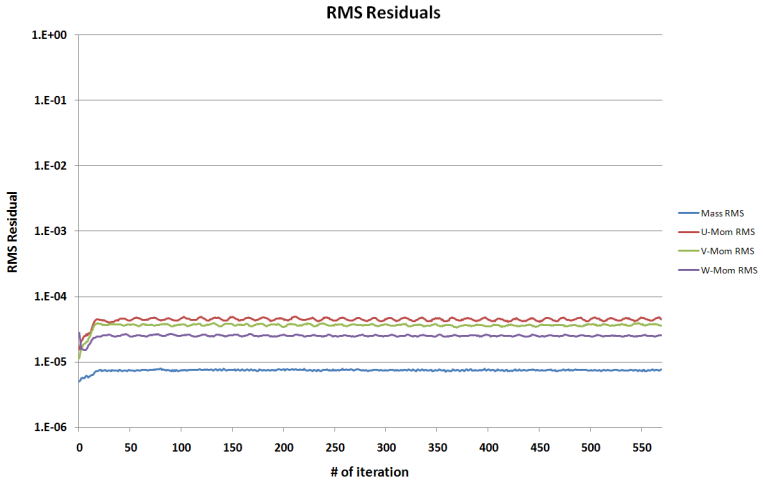

Fig. 4.2.6.1: RMS Residuals (Transient CFD)

The level of the residuals remains constant over the whole range of iteration steps. At the beginning a slight rise appears due to the fact that the initial solution was a quasi steady state case with a frozen rotor stator interface.

Mass Imbalance:

The mass imbalances in the unsteady CFD simulations are of the order of 10^{-5} which is extremely low for transient investigations:

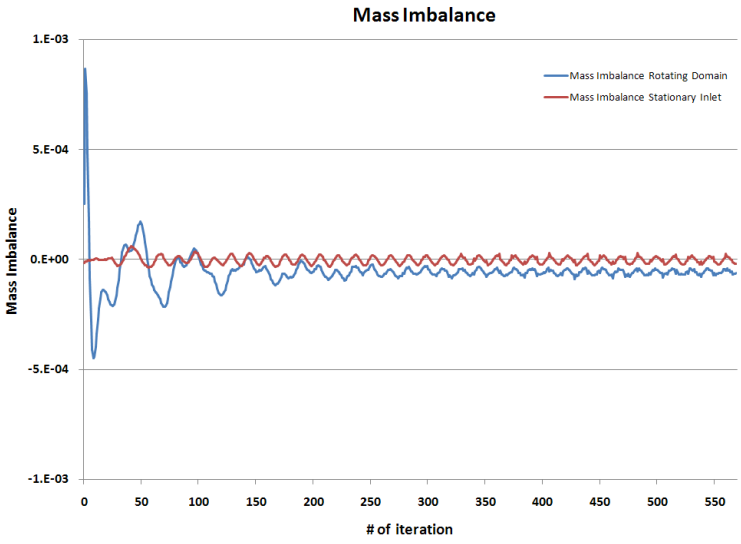

Fig. 4.2.6.2: Mass Flow Imbalance

The red curve shows the imbalance of the inlet section which is a stationary domain. The blue curve is the mass imbalance of the impeller. The imbalances as well as the residuals imply a certain periodicity. An other convergence quantification for the transient investigations which is of the same importance as the solver residuals is the periodicity of the solution due to the periodic distortion pattern at the inlet of the domain.

Periodic Convergence:

To record the periodicity of the solution several monitoring points are implemented on the surface of the main blade:

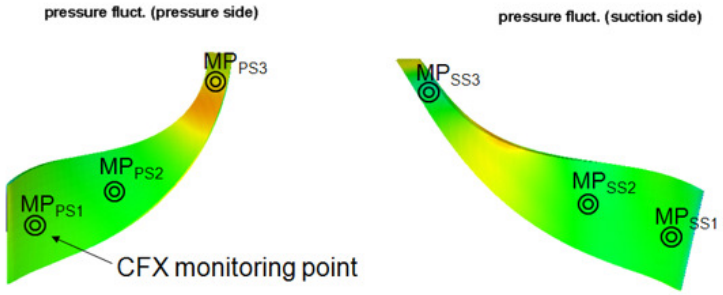

Fig. 4.2.6.3: Monitoring Points on Main Blade

The monitoring points record the time resolved blade pressure. In the publication of Dickmann (Dickmann et al., 2006) the periodicity is quantified graphically by connecting the peaks in the signal and looking for straightness without a quantification of the periodicity. Dickmann (Dickmann et al., 2006) checked for periodic convergence by monitoring the unsteady blade power which causes a certain averaging (and therefore smoothing) of the unsteady signal.

In contrast to Dickmann (Dickmann et al., 2006) the periodicity in the present work is quantified by statistically correlating the unsteady pressure signal of the monitoring points on the main blade surface of two consecutive impeller revolutions. This procedure provides a real quantification of the periodic convergence by correlating flow properties at discrete locations in the domain without any averaging or smoothing process. The diagram below shows characteristic pressure signal development during a transient CFD run. The location of the monitoring points corresponds to the figure one page before:

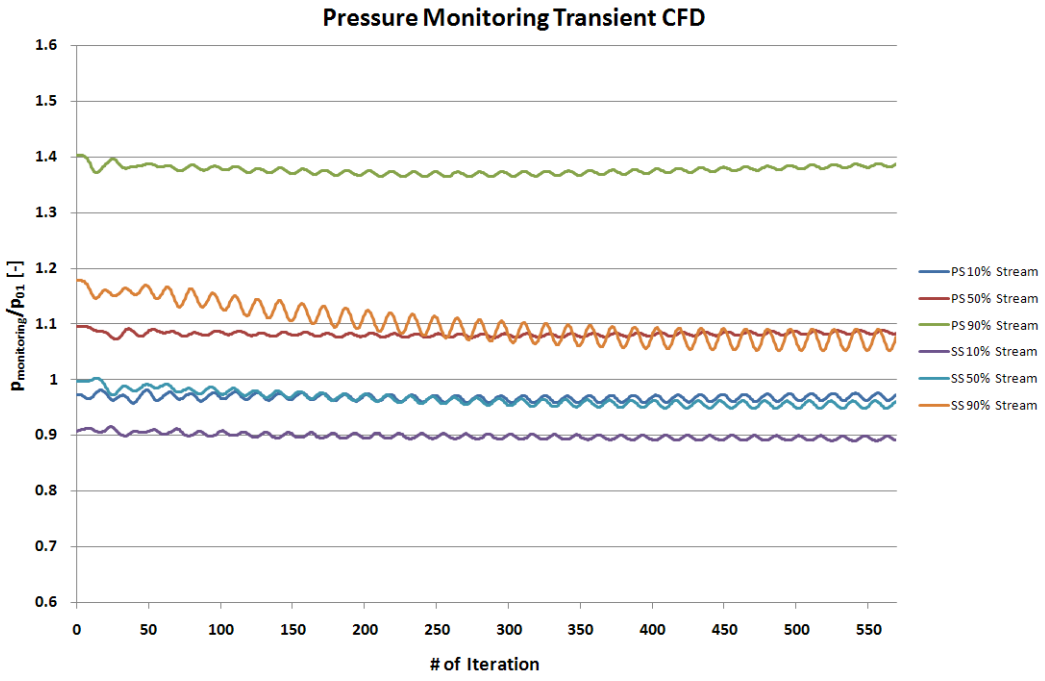

Fig. 4.2.6.4: Pressure Monitoring in Transient CFD Run

The resulting correlation coefficient of two consecutive impeller revolutions provides a convergence quantification of the periodic pressure signal on the main blade surface:

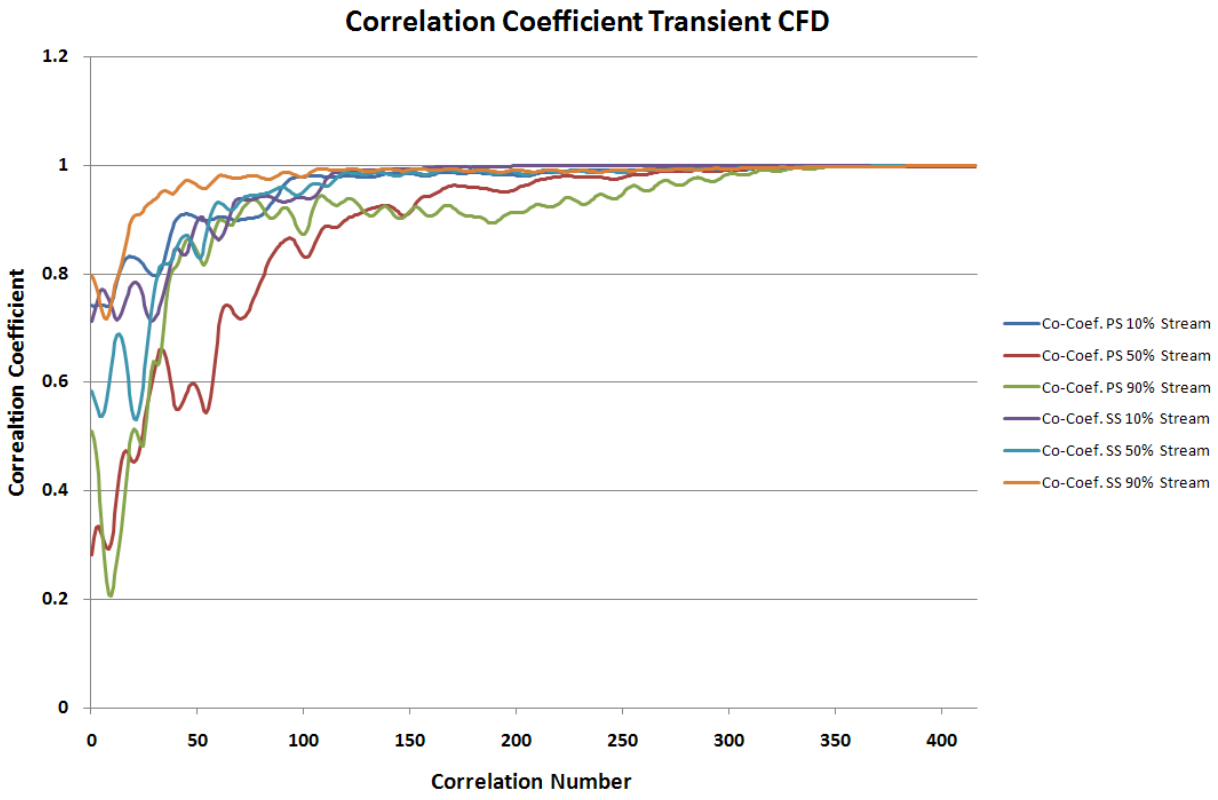

Fig. 4.2.6.5: Correlation Coefficient for Transient CFD Run

The demanded correlation coefficient in the present work for periodic convergence must be at least 99%. The values at the end of the diagram in the figure above are:

pressure side, 10% streamwise location:	99.9299%
pressure side, 50% streamwise location:	99.6755%
pressure side, 90% streamwise location:	99.9623%
suction side, 10% streamwise location:	99.9160%
suction side, 50% streamwise location:	99.9016%
suction side, 90% streamwise location:	99.8777%

If the required value for each correlation coefficient is reached the unsteady CFD results are recorded at each physical impeller position over one revolution. The unsteady simulations with the mentioned convergence criteria and the need for high quality initial solutions for the transient runs with a grid of about 4 million nodes requires high computational power and causes long runtimes for each operating point under investigation. A good initial solution needs about 15 CPU days and the transient run to reach periodic convergence requires about 84 CPU days.

4.2.7 Validation

The validation of the transient investigation is not as simple as in the steady state cases. Once the mass flow in the numerical simulation corresponds to the measured mass flow in the rig by adjusting the back pressure in the CFD model the resulting velocity profile at the inlet boundary condition plane can be compared to the measured FRAP profile:

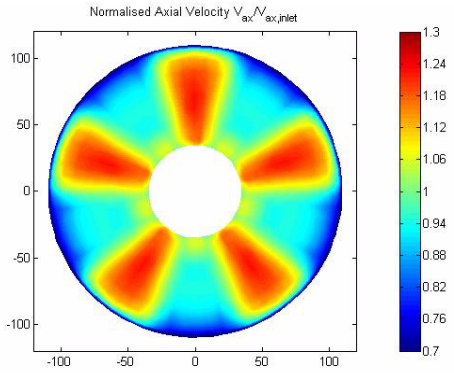

Fig. 4.2.7.1: Normalized Axial Velocity (FRAP) (A. Kammerer)

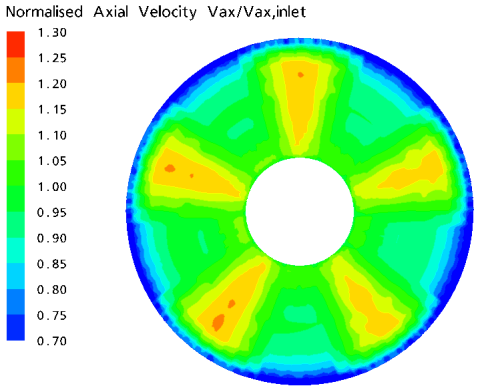

Fig. 4.2.7.2: Normalized Axial Velocity (CFD)

The profiles look different in a first view due to the different color coding. The FRAP profile is made with Matlab while the profile for the CFD case is made in the ANSYS CFX post processor. If one compares the numerical values the difference is in the range of 0.5% (maximum: 2.5%). The model therefore is assumed to be a good approximation of the reality.

4.2.8 Influence of Turbulence Intensity Boundary Condition

To quantify the influence of the turbulence intensity boundary condition at the inlet two simulations at 16250rpm are done. The only difference between the two cases is the turbulence intensity distribution. One case uses an average turbulence intensity of 5% over the whole inlet area. The second case contains the turbulence intensity distribution extracted from the FRAP measurements as explained in chapter 4.2.3. The simulations do not indicate any differences in the resulting flow field. To quantify the difference between the two cases the same procedure used to quantify the periodic convergence is applied on the 6 blade pressure monitoring points:

pressure side, 10% streamwise location:	99.979%
pressure side, 50% streamwise location:	99.993%
pressure side, 90% streamwise location:	99.909%
suction side, 10% streamwise location:	99.953%
suction side, 50% streamwise location:	99.986%
suction side, 90% streamwise location:	99.966%

Due to the high consistency of the compared results the transient investigations use an average turbulence intensity of 5% as inlet boundary condition to simplify the whole procedure.

4.2.9 Flow through Impeller

The intention of this chapter is to characterize the flow through the centrifugal impeller and to track the inlet distortion convecting through the device. The figure below shows the trace of the distortion pattern through the impeller. The color coding illustrates the ratio between relative total pressure divided by the relative total pressure at the inlet. The red zones at the inlet are zones of high relative total pressure ratio and the orange regions show the inlet flow distortion. The blue spots show the tip leakage vortex:

Fig. 4.2.9.1: Inlet Distortion Convecting through Impeller (Relative Total Pressure Ratio)

Due to the large pressure and velocity gradients through the impeller the tracking of the inlet distortion is not trivial. The relative total pressure provides the possibility to visualize the pattern of low relative total pressure. As a matter of course the relative total pressure in the distorted inlet flow is lower compared to the undistorted flow. The relative total pressure of the fluid while convecting through the impeller is constant in an ideal system. It is therefore possible to identify the zones of relative total pressure loss (boundary layer, vortical structures, inlet distortion, etc.).

A descriptive possibility to visualize the trace of the distortion through the blading is a blade to blade view at midspan:

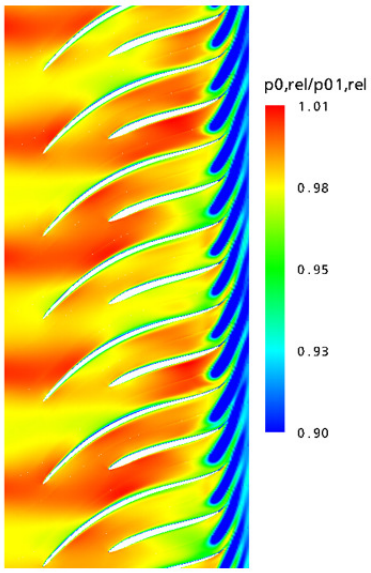

Fig. 4.2.9.2: 16250rpm, 5.EO, Q/Q_{ref}=0.73

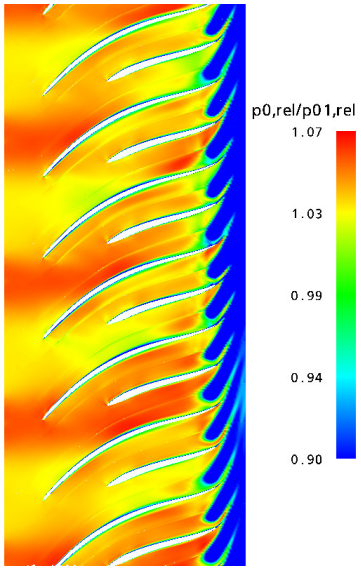

Fig. 4.2.9.3: 20700rpm, 4.EO, Q/Q_{ref}=0.98

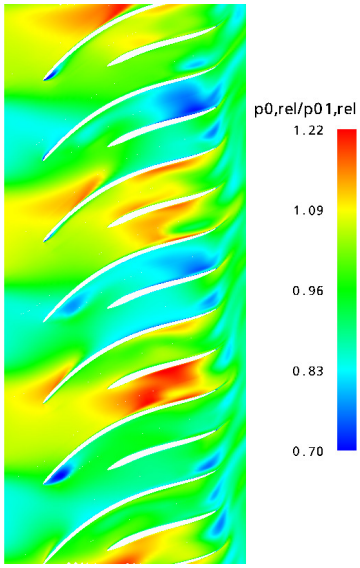

Fig. 4.2.9.4: 13360rpm, 3.EO, Q/Q_{ref}=0.58

Three different distortion screen geometries are in use for the unsteady analysis as illustrated in chapter 3.13. The comparison above clarifies the varying spatial extension of the distortion pattern and explains the need for the entire impeller in the transient CFD simulation due to the asymmetric allocation over the seven main blade pitches. It is not possible to set up a model containing only a fraction of the whole impeller with periodic boundary interfaces as in the steady state computations where only the seventh part of the impeller is implemented.

The figure on the left shows the excitation of the first bending mode with the 5. engine order distortion at 16250 rpm. On the middle the 4. EO distortion screen excites the first bending mode at 20700 rpm. It is hard to see differences in the illustrations except of the tip leakage vortex (blue zones) which is stronger at higher rotational speed and higher mass flow rate. The blade to blade view on the right illustrates the relative total pressure coefficient for a 3. engine order distortion screen that excites the 1st bending mode of the main blade with the first harmonic (6. EO) at 13360rpm. An interesting feature is visible in the view at 13360 rpm on the pressure side of the second main blade from the bottom. The blue zone shows a separation caused by the inlet distortion and is then convected through the impeller.

As mentioned in chapter 4.2.2 the total pressure profile is applied in an idealized form to allow a simple identification of the periodicity to get a certain experience concerning unsteady simulations with the software in use. About three months experience in setting up and monitoring time resolved simulations in ANSYS CFX allowed to run a case with inlet total pressure profile as it is measured in the test rig with FRAP probes:

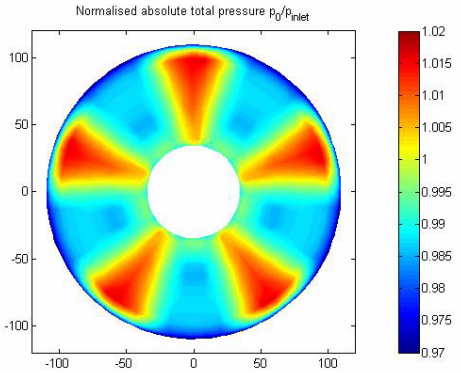

Fig. 4.2.9.5: Idealized Inlet Total Pressure Profile (A. Kammerer)

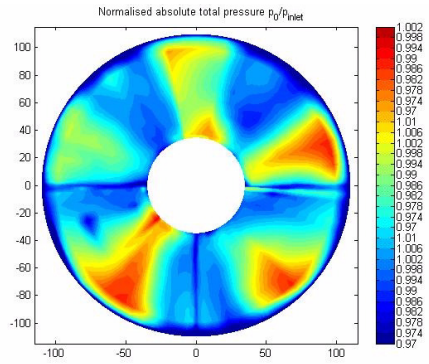

Fig. 4.2.9.6: „Real“ Inlet Total Pressure Profile (A. Kammerer)

A certain idealization procedure still has to be done due to the fact that, as mentioned earlier, not the whole measurement plane in the test rig is accessible because of struts supporting the inlet duct of the rig. The following comparison shows the relative total pressure coefficient for the same screen geometry (5. EO):

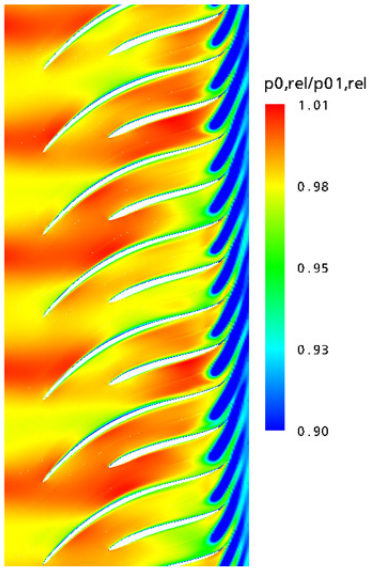

Fig. 4.2.9.7: 16250rpm, 5.EO, Q/Q_{ref}=0.73

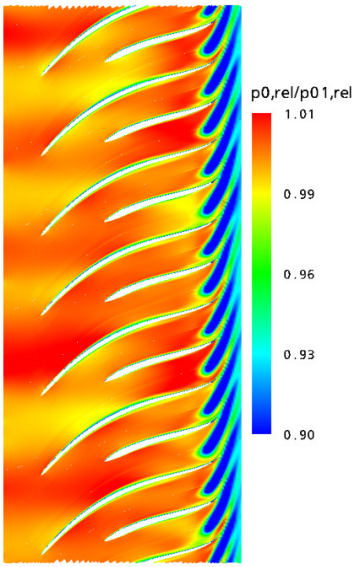

Fig. 4.2.9.8: 16250rpm, 5.EO, Q/Q_{ref}=0.73

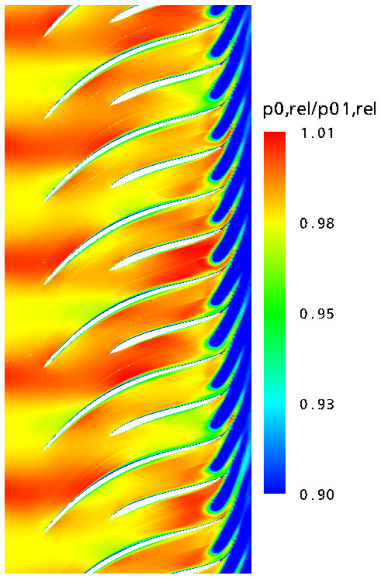

Fig. 4.2.9.9: 17340rpm, 5.EO, Q/Q_{ref}=0.80

The contours on the left and in the middle illustrate exactly the same operating point. The only difference is the inlet total pressure boundary condition. The blade to blade view on the left is the result of the idealized inlet total pressure boundary condition profile. The contour in the middle shows the resulting relative total pressure ratio for the „real“ total pressure profile measured with FRAP probes. One can see that the idealized case shows continuous distribution of the distortion pattern at the inlet compared to the „real“ one. The distorted regions at the inlet (yellow regions) have lower relative total pressure ratio niveau for the idealized case. On the right the same distortion screen excites the second main blade mode via first harmonic (10. engine order) again with an idealized total pressure profile at the inlet.

4.2.10 Unsteady Blade Pressure

A major objective of the present work is the unsteady pressure distribution on the blade surface. The time varying pressure distribution on the blade caused by the inlet distortion may excite modes of the blades. It is an advantage of the numerical investigation compared to the test rig measurements that one can run the system at resonance without the risk to destroy anything in the rig.
To understand the excitation of the blades it is important to know the magnitude and location of the unsteady load. The first operating point under investigation is at 16250rpm and is the resonance point of the first bending mode of the main blade excited by the fifth engine order distortion screen.

16250 rpm, 5. EO:

To get a first idea of the pressure distribution on the suction and pressure side of the main blade the pressure fluctuation is plotted on the main blade surface. The Reynolds decomposition of the unsteady pressure avoids the difficulty to identify the distortion due to the comparatively strong pressure gradient through the blading by just plotting the fluctuating part of the pressure signal. The figure below shows the unsteady pressure distribution for one particular time step:

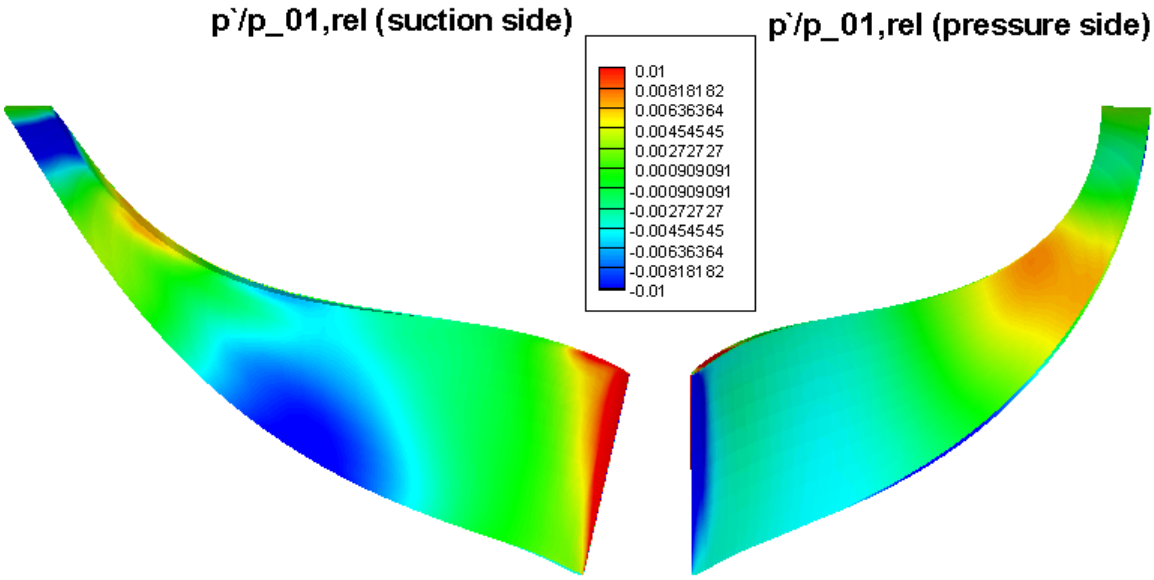

Fig. 4.2.10.1: p‘(t) /$p_{01,rel}$ on Main Blade Surface (16250 rpm, 5. EO)

The orange zone on the pressure side of the blade shows a positive pressure fluctuation compared to the local time mean pressure arising from an undistorted inlet flow field region. The blue areas on the suction side of the main blade have negative pressure fluctuation resulting from a distorted zone in the inlet of the compressor.

The path- time diagram offers the possibility to illustrate the distortion convecting along the blade surface by plotting the fluctuating part of the pressure versus streamwise location at 50% span and time axis:

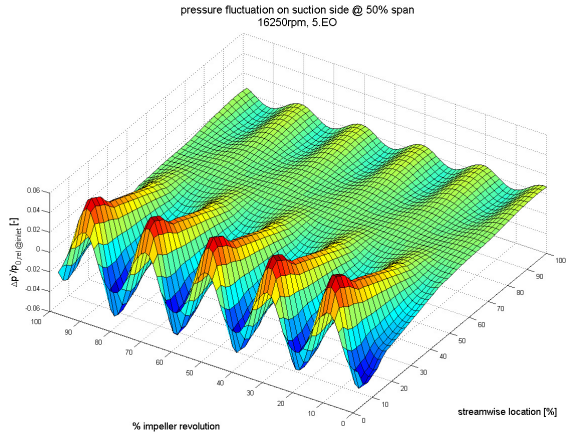

Fig. 4.2.10.2: Path- Time Suction Side (16250rpm)

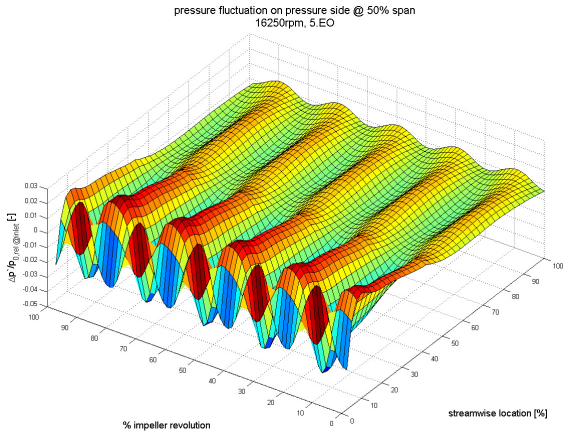

Fig. 4.2.10.3: Path- Time Pressure Side (16250rpm)

More information about the effect of the unsteady pressure field on the main blade can be gained by building the difference pressure side minus suction side:

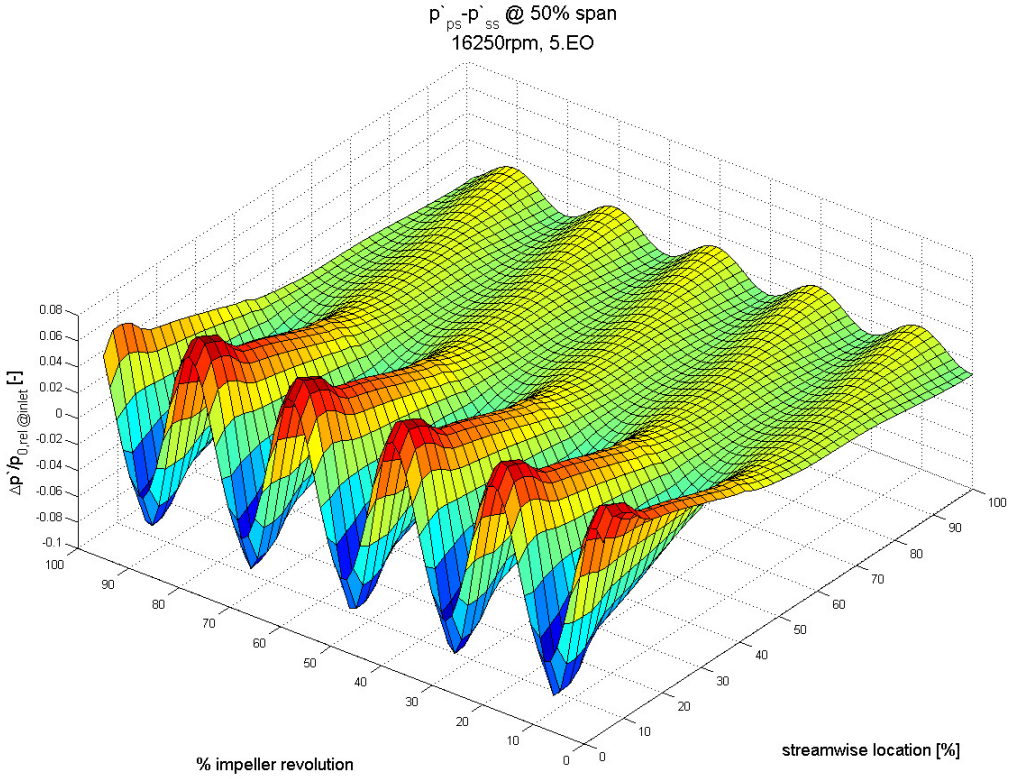

Fig. 4.2.10.4: Path- Time Pressure Side minus Suction Side (16250rpm)

The integral of the pressure fluctuation over the blade area equals the dynamic load caused by the distorted inlet flow field. One can see that the distortion convects through the impeller with almost constant speed. The amplitude gets weaker from the leading edge of the main blade to the leading edge of the splitter blade. The alternating direction of the dynamic load at the leading edge may excite the blade if the frequency of the excitation hits the natural frequency of the blade.

To illustrate the amplitude of the periodic excitation the pressure fluctuation is plotted over one impeller rotation:

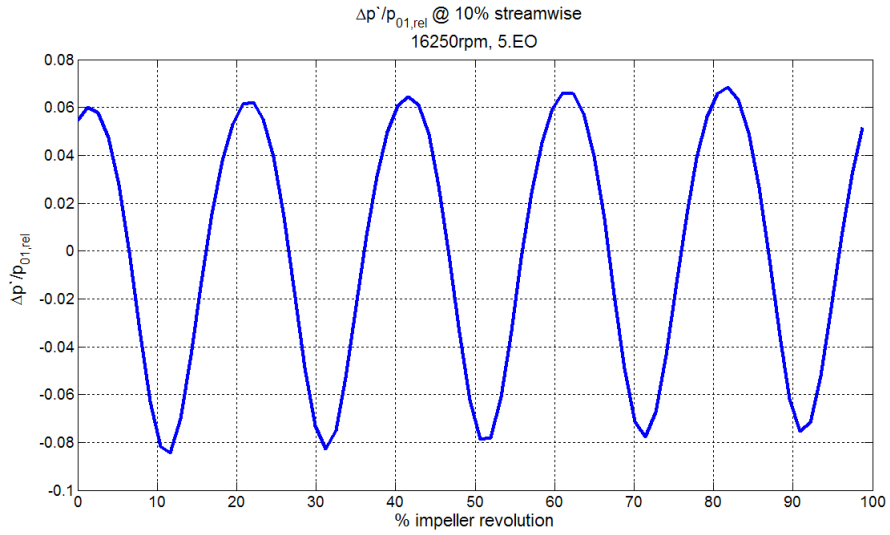

Fig. 4.2.10.5: $\Delta p'/p_{01,rel}$ (16250rpm, 10% streamwise direction on mainblade)

The signal clearly shows the 5. EO excitation and the peak to peak amplitude is about 14% of the average relative total pressure at the inlet of the compressor. It is important to point the fact that there is no phase shift between the fluctuation on the pressure and suction side.

The Fourier transform of the unsteady pressure fluctuation at midspan in streamwise direction on both the pressure and suction side shows the development of the distortion convecting through the impeller:

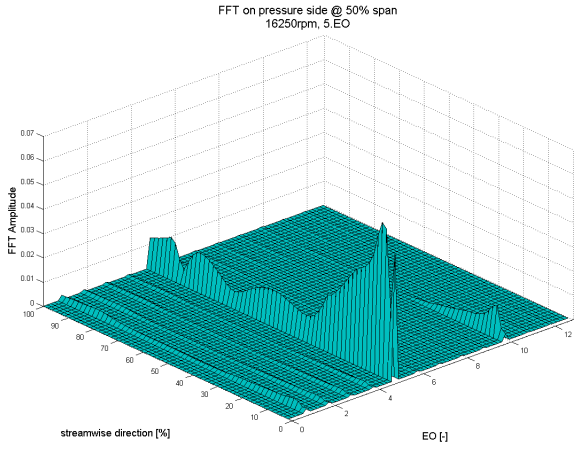

Fig. 4.2.10.6: FFT, 16250rpm, Pressure Side Main Blade, 50% Span

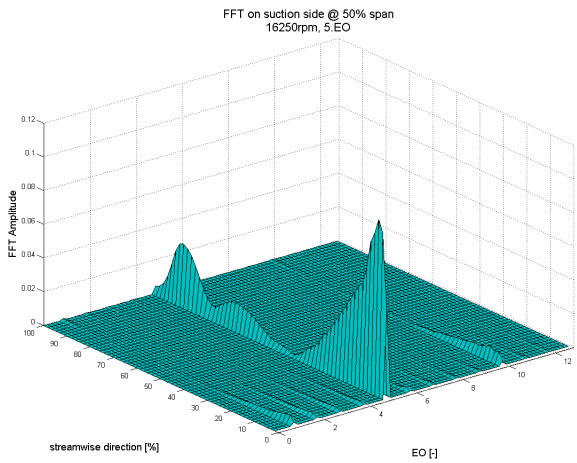

Fig. 4.2.10.7: FFT, 16250rpm, Suction Side, Main Blade, 50% Span

As expected the excitation is very strong at the leading edge of the main blade. The first harmonic appears only very weak at the front of the blade. The amplitude of the first harmonic is about 15% of the amplitude of the fundamental frequency.

The nonuniform development of the amplitude in the frequency domain at midspan from leading to trailing edge demands for an illustration of the distribution of the amplitude on the blade surfaces:

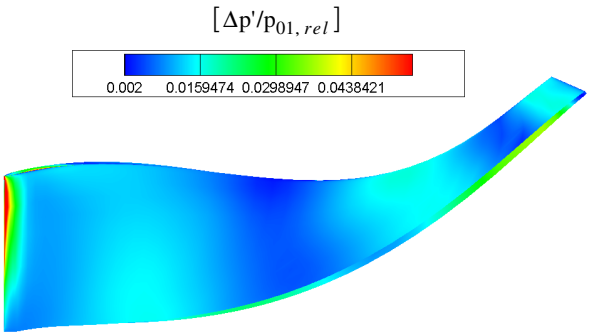

Fig. 4.2.10.8: FFT Amplitude, 12625orpm, Pressure Side Main Blade

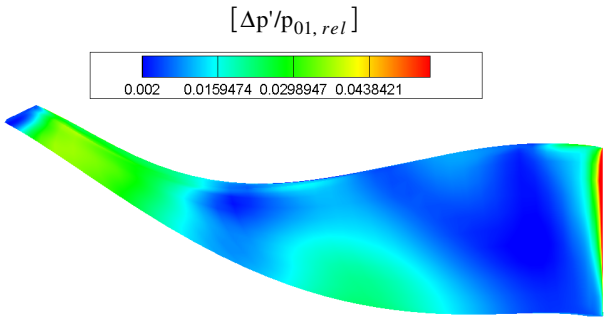

Fig. 4.2.10.9: FFT Amplitude, 12625orpm, Suction Side, Main Blade

The red zones are the regions of the highest amplitude of the signal in the frequency domain. But there are huge areas on the surfaces with very low amplitude and therefore very weak dynamic load.

The next operating point under investigation is at 13360 rpm with a 3. EO distortion screen. The first harmonic excites the first bending mode of the main blade.

13360 rpm, 3. EO:

The path- time diagrams offer a detailed view on the dynamics through the impeller:

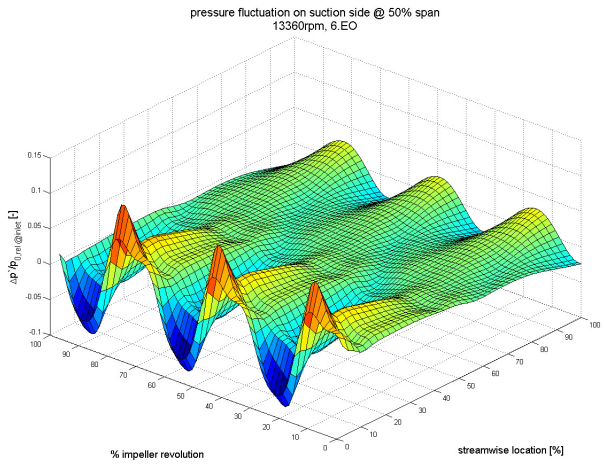

Fig. 4.2.10.10: Path- Time Suction Side (13360rpm)

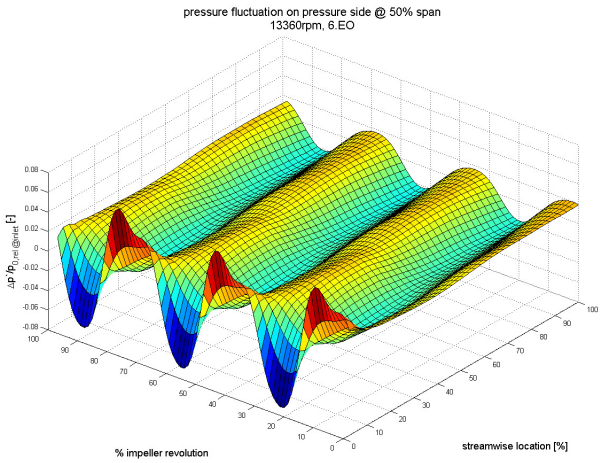

Fig. 4.2.10.11: Path- Time Pressure Side (13360rpm)

The difference of pressure side minus suction side illustrates the dynamic load onto the main blade:

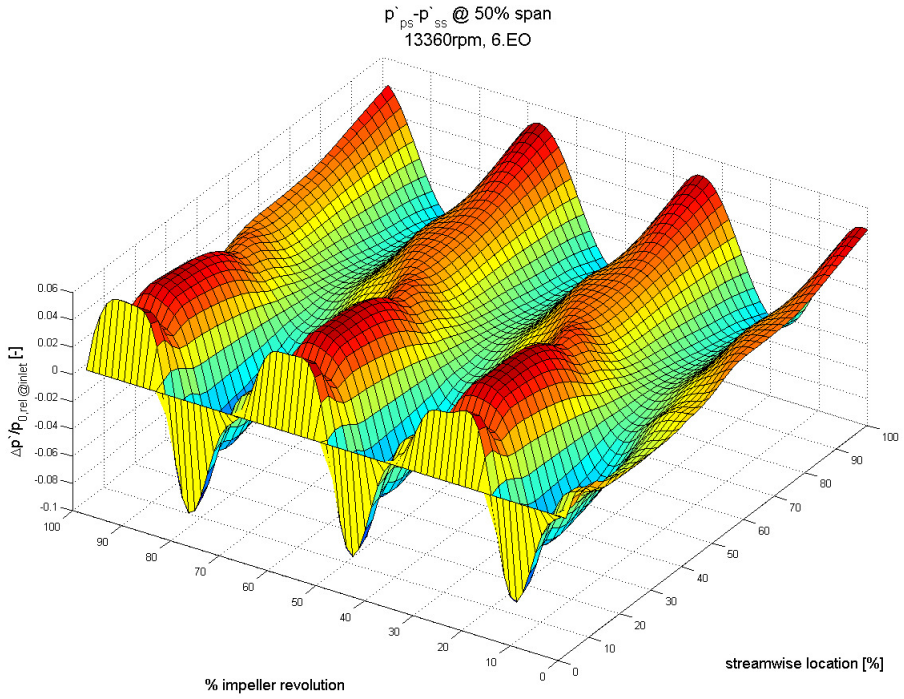

Fig. 4.2.10.12: Path- Time Pressure Side minus Suction Side (13360rpm)

The intention of the distortion screen with three distortion baffles is to excite the first main blade mode via first harmonic. The signal at the leading edge indicates the content of the first harmonic quite clearly. To get a better idea about the evolution of the fluctuating pressure difference at the leading edge the signal at 10% streamwise direction is plotted over one impeller revolution:

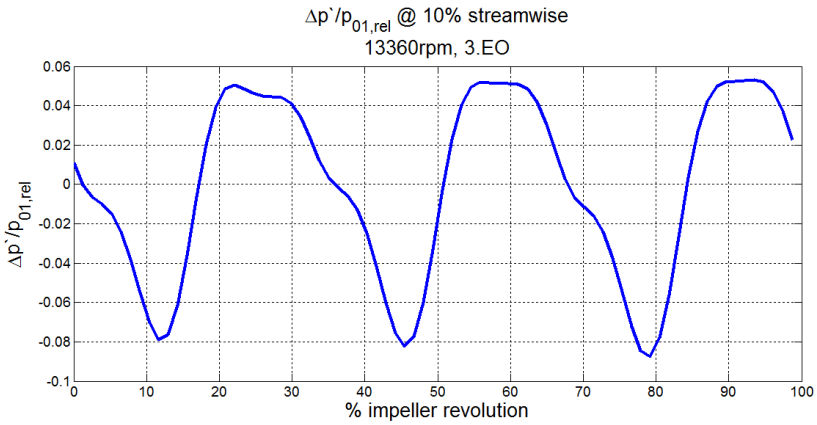

Fig. 4.2.10.13: Δ p‘/$p_{01,rel}$ (13360rpm, 10% streamwise direction on mainblade)

The Fourier transform of the unsteady pressure fluctuation at midspan in streamwise direction on both the pressure and suction side shows the development of the distortion convecting through the impeller:

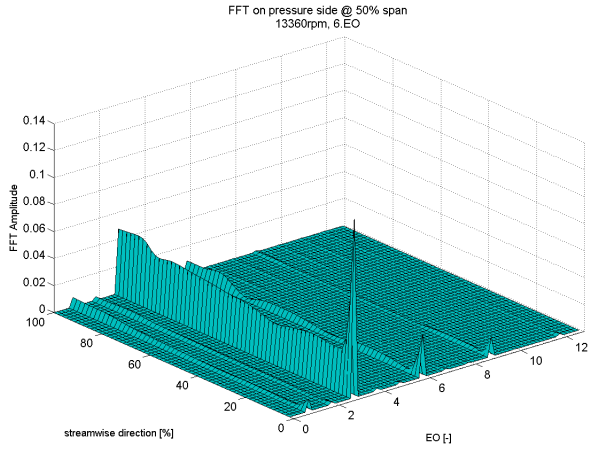

Fig. 4.2.10.14: FFT, 13360rpm, Pressure Side Main Blade, 50% Span

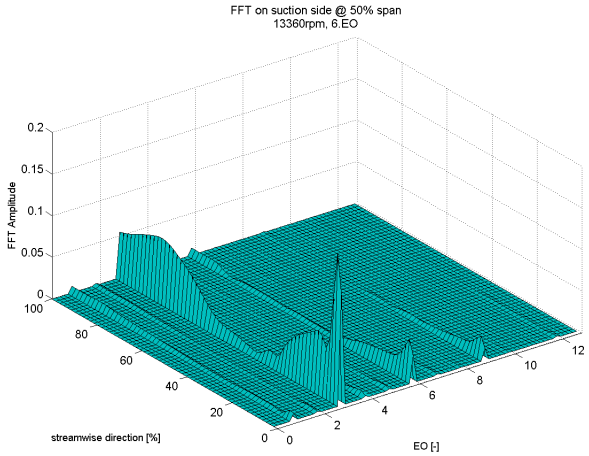

Fig. 4.2.10.15: FFT, 13360rpm, Suction Side, Main Blade, 50% Span

As expected the excitation is again very strong at the leading edge of the main blade. The first harmonic appears quite strong at the front of the blade. The FFT signal right at the leading edge shows the relation of the 3. EO compared to the harmonics:

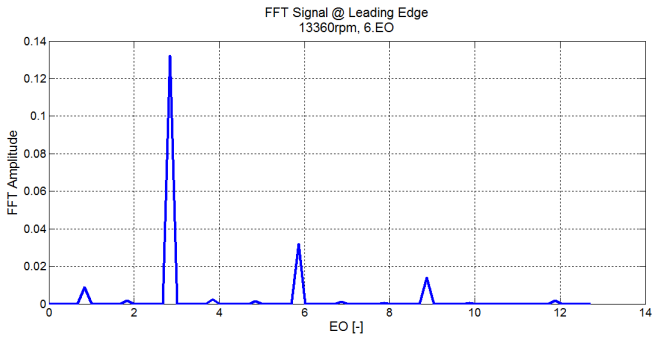

Fig. 4.2.10.16: FFT, Leading Edge Main Blade (13360rpm)

The amplitude of the 6. EO excitation is about 3.7 times smaller than the 3. EO peak. The contour of the FFT amplitude on the main blade surface of the fundamental frequency illustrates the distribution over the blade surface:

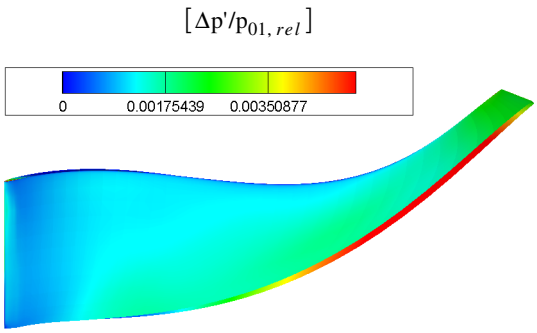

Fig. 4.2.10.17: FFT Amplitude, 13360rpm, Pressure Side Main Blade

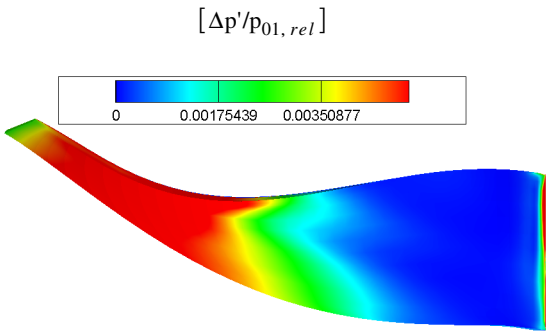

Fig. 4.2.10.18: FFT Amplitude, 13360rpm, Suction Side Main Blade

The blue regions with very low amplitude on both sides of the blade are noticeable but the amplitudes at the leading edge and in the rear part of the suction side are very high.

The next operating point under investigation is at 17340 rpm with a 5. EO distortion screen. The first harmonic excites the second bending mode of the main blade.

17340 rpm, 5. EO:

The fluctuating part of the unsteady pressure distribution on the blade surface is plotted for one time step below:

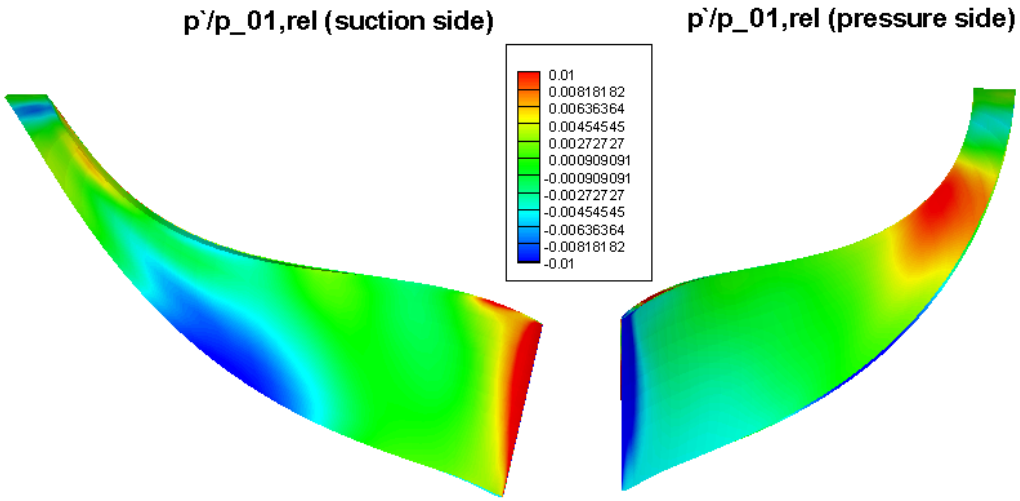

Fig. 4.2.10.19: p'(t)/$p_{01,rel}$ on Main Blade Surface (17340 rpm, 5. EO)

The red zone on the pressure side is a rudiment of an undistorted inlet flow field. One can see that the leading edge passes a distorted zone (blue leading edge on pressure side). On the suction side the blue area is again a low relative total pressure pattern caused by a distorted inlet flow field. It is conspicuous that the distorted area convects over the suction side at a niveau close to the hub. The reason might be the tip leakage vortex pushing the flow field from the shroud to the hub.

The path- time diagrams offer a detailed view on the dynamics through the impeller:

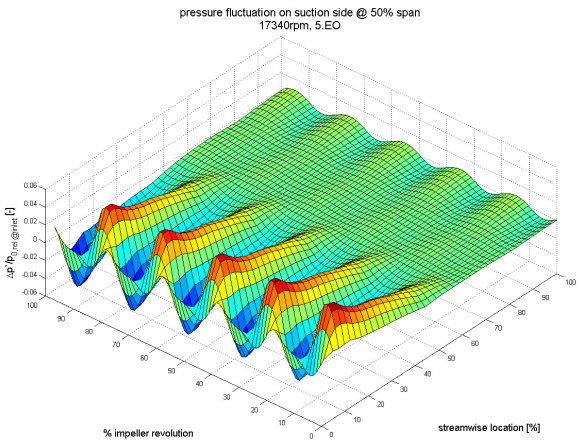

Fig. 4.2.10.20: Path- Time Suction Side (17340rpm)

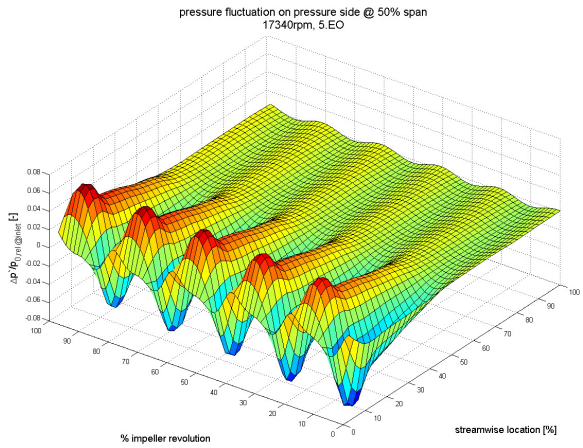

Fig. 4.2.10.21: Path- Time Pressure Side (17340rpm)

The difference of pressure side minus suction side illustrates the dynamic load onto the main blade:

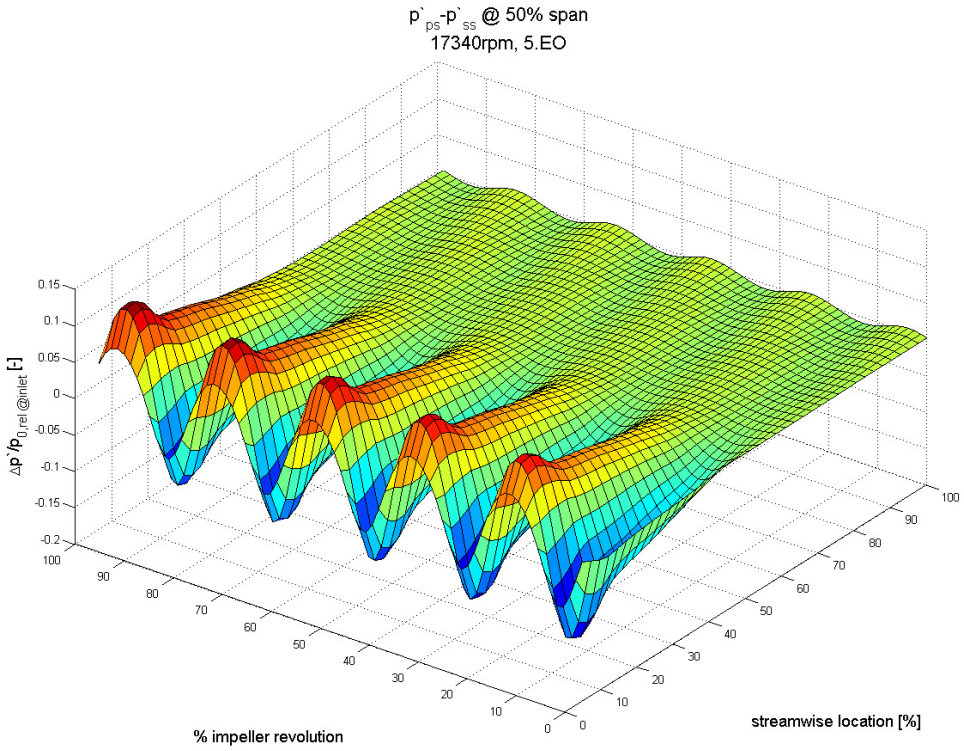

Fig. 4.2.10.22: Path- Time Pressure Side minus Suction Side (17340rpm)

The intention of the distortion screen with five distortion baffles is to excite the second main blade mode via first harmonic. The signal at the leading edge does not indicates the content of the first harmonic.

To get a better idea about the evolution of the fluctuating pressure difference at the leading edge the signal at 10% streamwise direction is plotted over one impeller revolution:

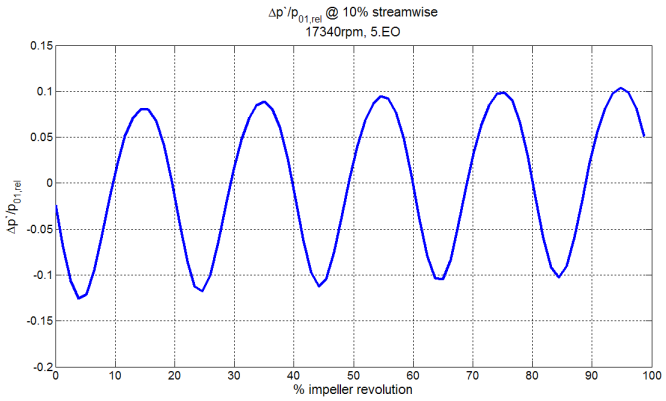

Fig. 4.2.10.23: Δ p'/$p_{01,rel}$ (17340rpm, 10% streamwise direction on mainblade)

The slight shift is the result of a not completely converged solution. An additional impeller revolution would be sufficient to lose the drift. The relevant quantities are not affected by this effect.

The Fourier transform of the unsteady pressure fluctuation at midspan in streamwise direction on both the pressure and suction side shows the development of the distortion convecting through the impeller:

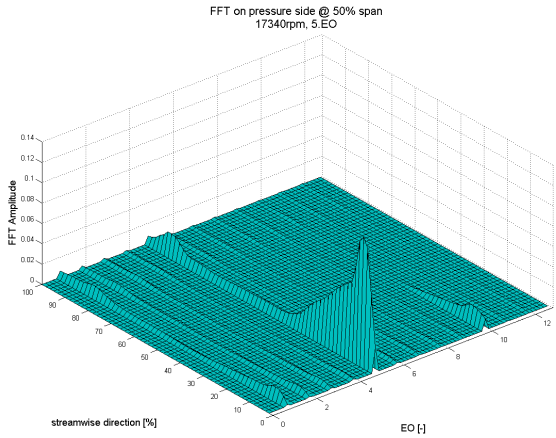

Fig. 4.2.10.24: FFT, 17340rpm, Pressure Side Main Blade, 50% Span

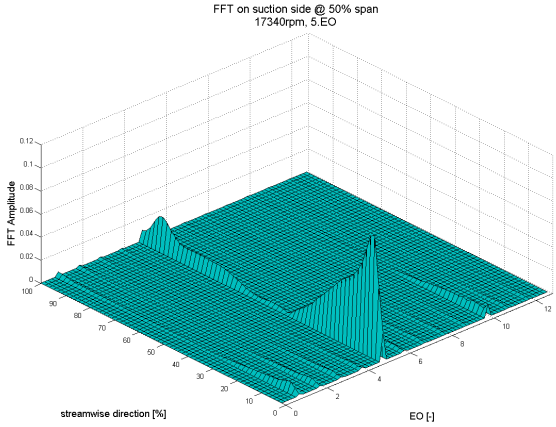

Fig. 4.2.10.25: FFT, 17340rpm, Suction Side, Main Blade, 50% Span

The excitation is very strong at the leading edge of the main blade. The first harmonic appears only very weak at the front of the blade. The contour of the FFT amplitude on the main blade surface illustrates the distribution over the blade surface:

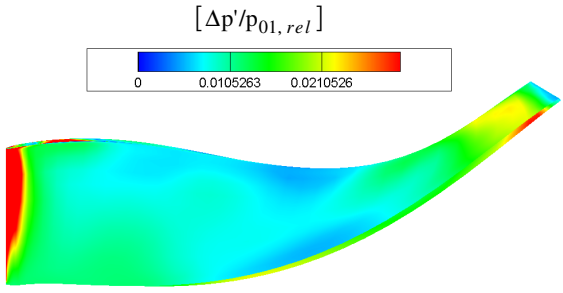

Fig. 4.2.10.26: FFT Amplitude, 17340rpm, Pressure Side Main Blade

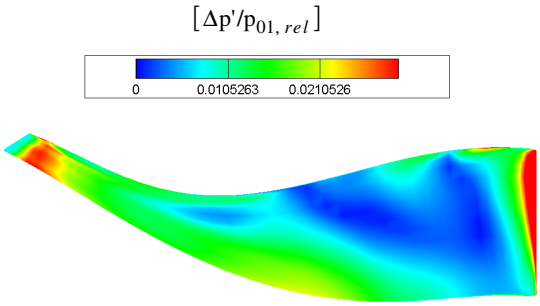

Fig. 4.2.10.27: FFT Amplitude, 17340rpm, Suction Side Main Blade

The last operating point under investigation is at 20700 rpm with a 4. EO distortion screen that excites the first bending mode of the main blade.

20700 rpm, 4. EO:

The fluctuating part of the unsteady pressure distribution on the blade surface is plotted for one time step below:

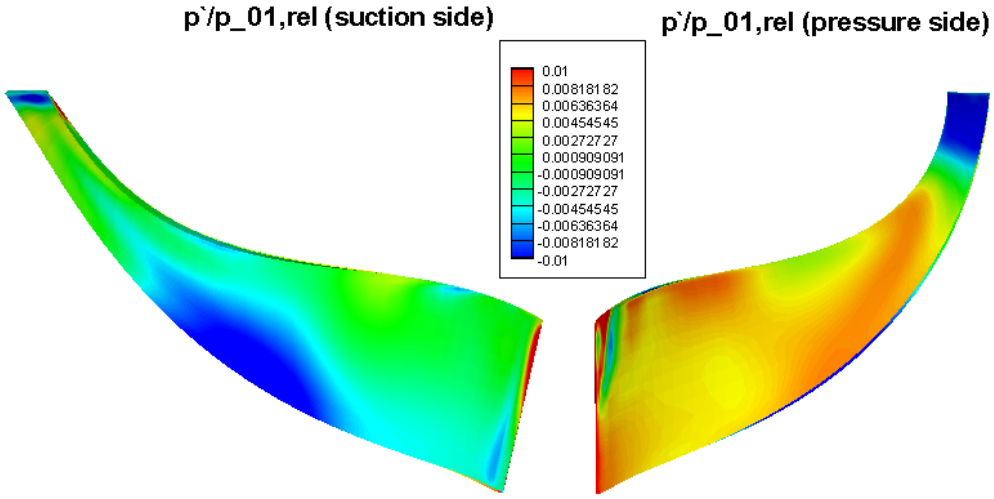

Fig. 4.2.10.28: $p'(t)/p_{01,rel}$ on Main Blade Surface (20700 rpm, 4. EO)

The broad orange area on the pressure side is an undistorted zone of the inlet flow field. At the trailing edge a distorted zone is leaving the impeller. On the suction side the blue area is again a low relative total pressure pattern caused by a distorted inlet flow field.

The path- time diagrams offer a detailed view on the dynamics through the impeller:

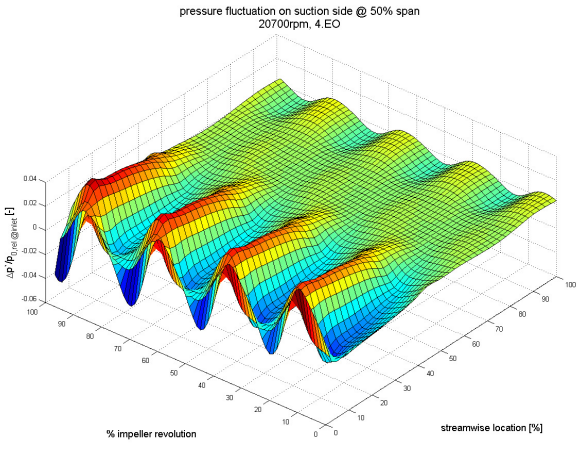

Fig. 4.2.10.29: Path- Time Suction Side (20700rpm)

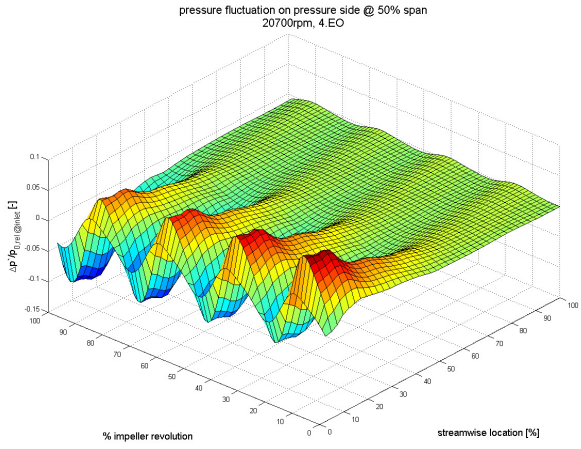

Fig. 4.2.10.30: Path- Time Pressure Side (20700rpm)

The difference of pressure side minus suction side illustrates the dynamic load onto the main blade:

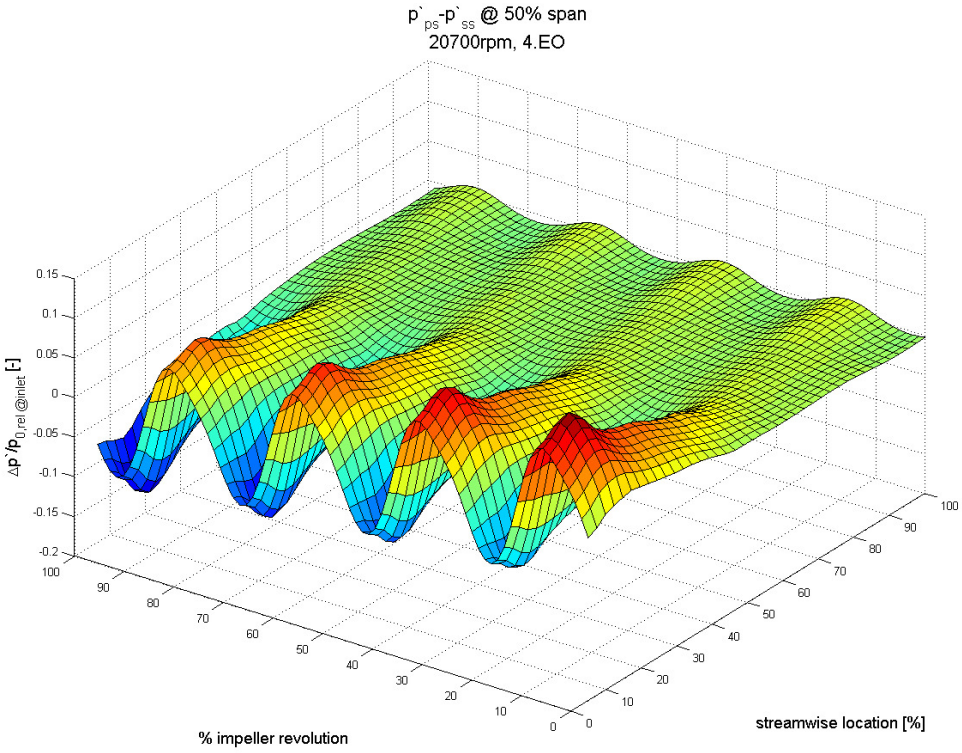

Fig. 4.2.10.31: Path- Time Pressure Side minus Suction Side (20700rpm)

The intention of the distortion screen with four distortion baffles is to excite the first main blade mode. To get a better idea about the evolution of the fluctuating pressure difference at the leading edge the signal at 10% streamwise direction is plotted over one impeller revolution:

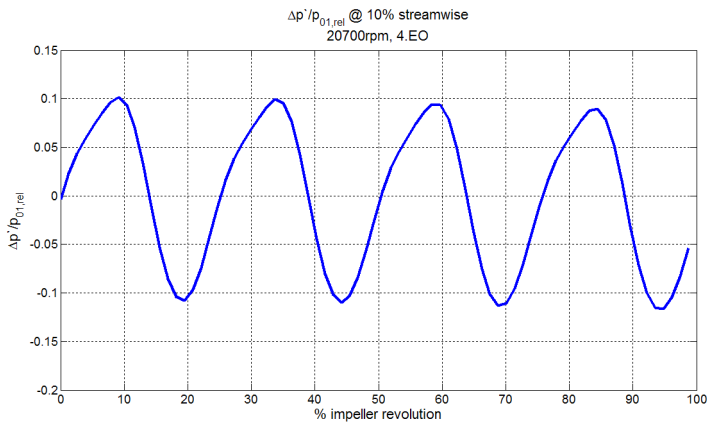

Fig. 4.2.10.32: Δ p‘/$p_{01,rel}$ (20700rpm, 10% streamwise direction on mainblade)

The slight shift is the result of a not completely converged solution. An additional impeller revolution would be sufficient to lose the drift. The relevant quantities are not affected by this effect.

The Fourier transform of the unsteady pressure fluctuation at midspan in streamwise direction on both the pressure and suction side shows the development of the distortion convecting through the impeller:

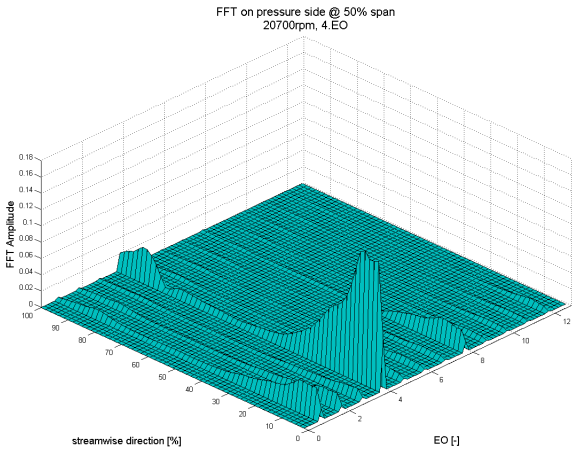

Fig. 4.2.10.33: FFT, 20700rpm, Pressure Side Main Blade, 50% Span

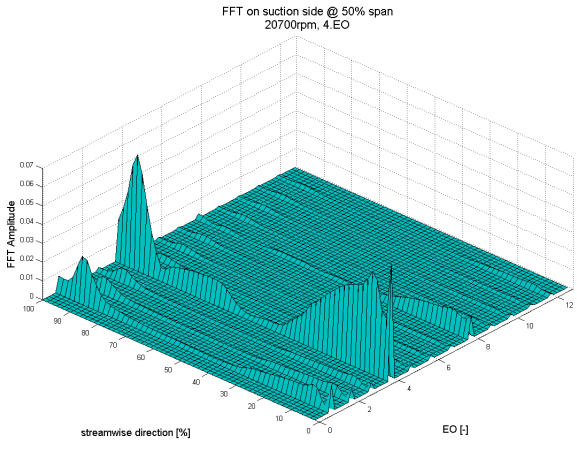

Fig. 4.2.10.34: FFT, 20700rpm, Suction Side, Main Blade, 50% Span

The excitation is very strong at the leading edge of the main blade. The high amplitude at the rear part of the main blade on the suction side is conspicuous. The contour of the FFT amplitude on the main blade surface illustrates the distribution over the blade surface:

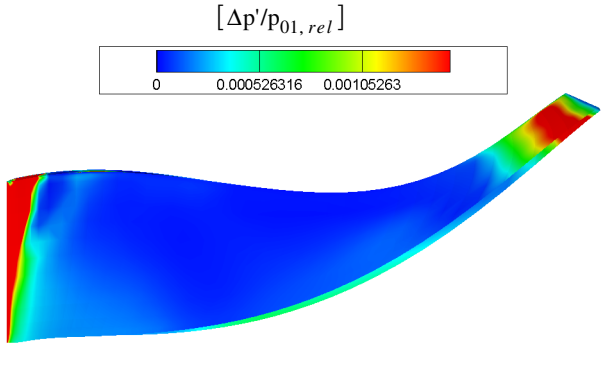

Fig. 4.2.10.35: FFT Amplitude, 20700rpm, Pressure Side Main Blade

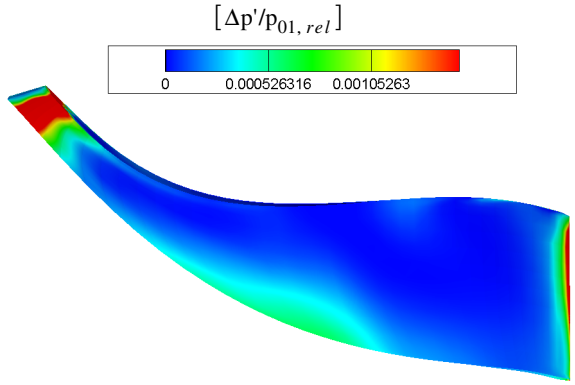

Fig. 4.2.10.36: FFT Amplitude, 20700rpm, Suction Side Main Blade

The extension of the blue regions with very low amplitude on both sides of the blade is extremely large. The reason for such a large extension might be the relatively high rotational speed. The high amplitudes not only at the leading edge but also in the rear part of the blade are clearly visible as indicated in the FFT signal along midspan.

The last investigation is done with non- idealized inlet total pressure profile at 16250rpm. The solver residuals as well as the mass imbalance are of the same order of magnitude as in the investigations with idealized profiles.

The unsteady pressure signals at the solver monitoring points look different due to the slightly asymmetric profile in circumferential direction:

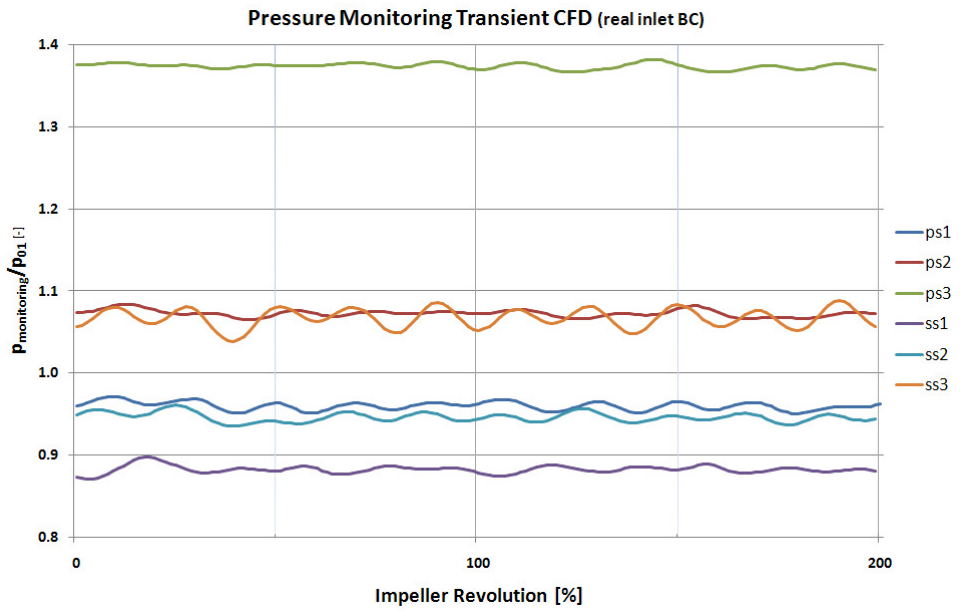

Fig. 4.2.10.37: Pressure Monitoring in Transient CFD (16250rpm, two impeller revolutions, unidealized total pressure profile)

The path- time diagrams show the same trend as in the idealized case but with different distribution for the distortion from screen to screen:

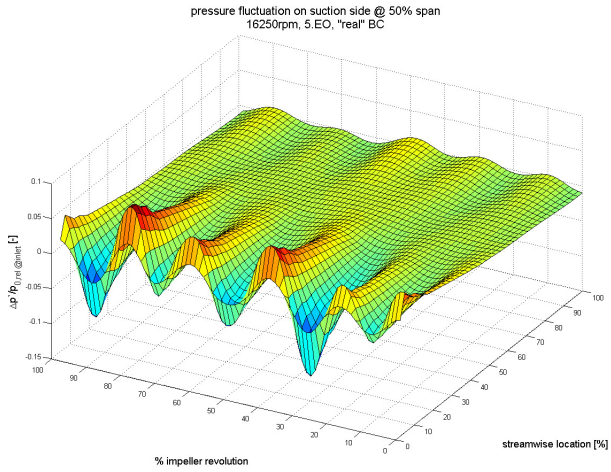

Fig. 4.2.10.38: Path- Time Suction Side (16250rpm, „real“)

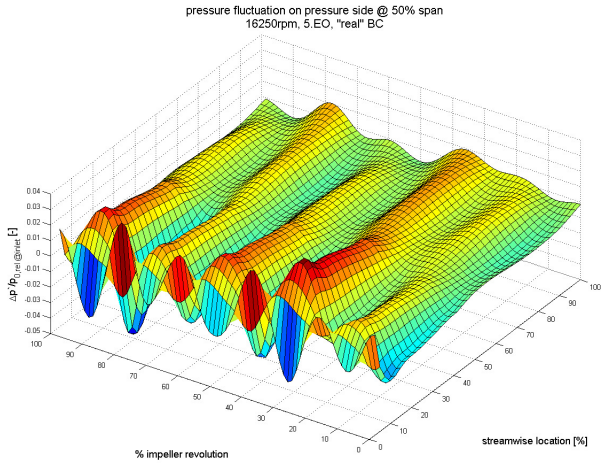

Fig. 4.2.10.39: Path- Time Pressure Side (16250rpm, „real“)

The difference of pressure side minus suction side illustrates the dynamic load onto the main blade:

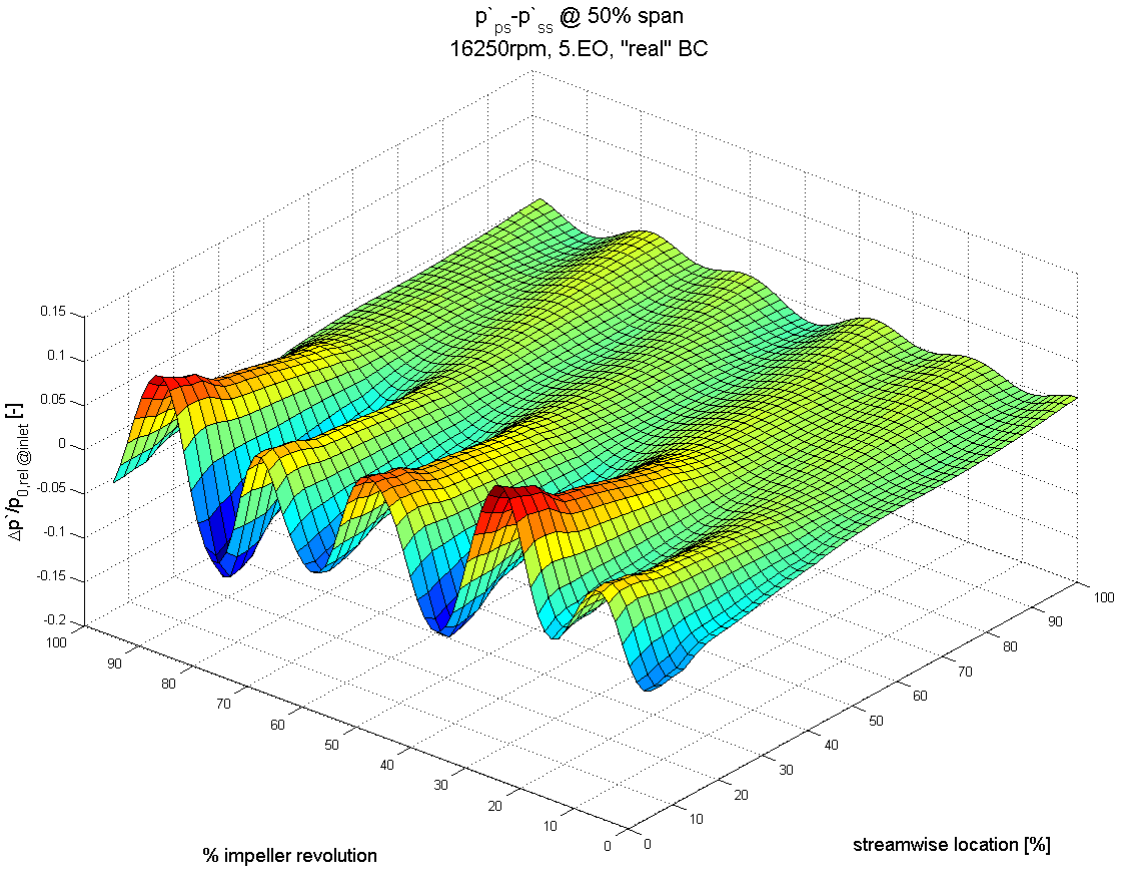

Fig. 4.2.10.40: Path- Time Pressure Side minus Suction Side (16250rpm, „real“)

The development of the distortion convecting through the impeller shows good consistence compared to the idealized case.

The evolution of the fluctuating pressure difference at the leading edge at 10% streamwise direction is plotted over one impeller revolution:

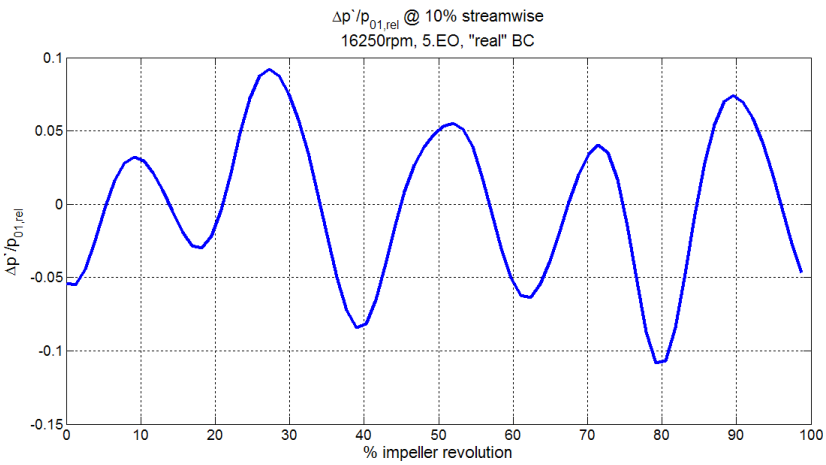

Fig. 4.2.10.41: Δ p‘/$p_{01,rel}$ (16250rpm, „real“, 10% streamwise direction on mainblade)

The Fourier transform of the unsteady pressure fluctuation at midspan in streamwise direction on both the pressure and suction side shows the development of the distortion convecting through the impeller:

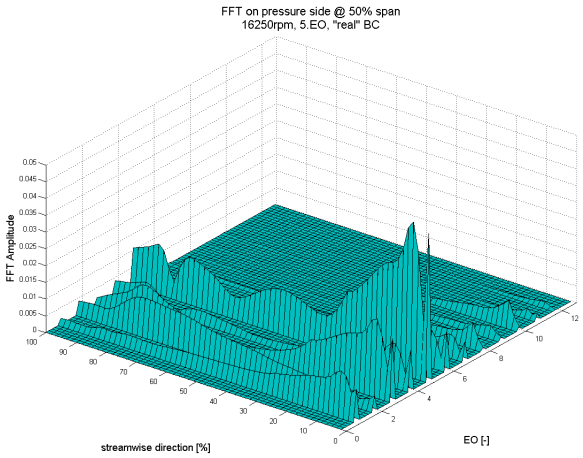

Fig. 4.2.10.42: FFT, 16250rpm, „real“, PS Main Blade, 50% Span

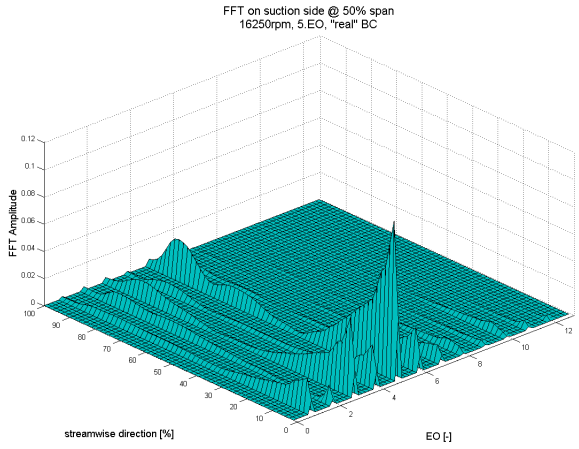

Fig. 4.2.10.43: FFT, 16250rpm, „real“, SS, Main Blade, 50% Span

As expected the signal in the frequency domain is no more clean as in the idealized case but the excitation still is very strong at the leading edge of the main blade. Lower engine orders appear quite strong at the leading edge of the blade. The contour of the FFT amplitude on the main blade surface illustrates the distribution over the blade surface:

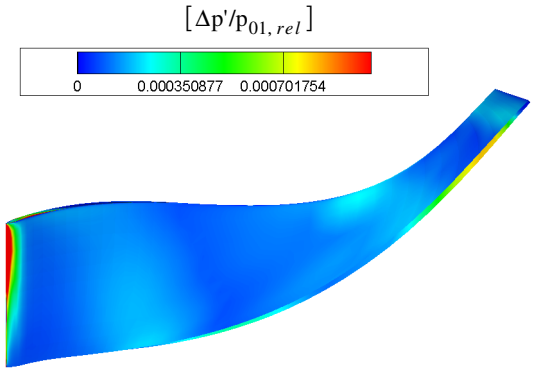

Fig. 4.2.10.44: FFT Amplitude, 16250rpm, „real“, PS Main Blade

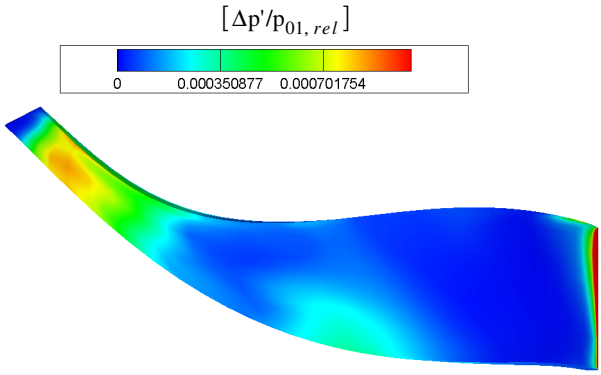

Fig. 4.2.10.45: FFT Amplitude, 16250rpm, „real“, SS Main Blade

The comparison with the idealized case show very good consistence of the resulting distribution of the FFT amplitude on the main blade surface:

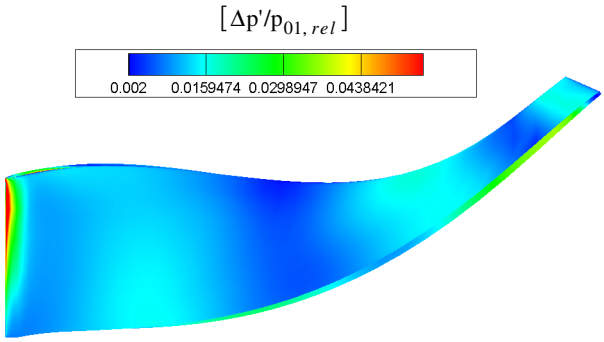

Fig. 4.2.10.46: FFT Amplitude, 16250rpm, ideal, PS Main Blade

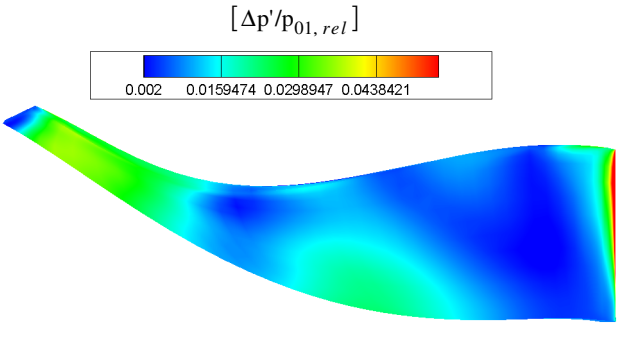

Fig. 4.2.10.47: FFT Amplitude, 16250rpm, ideal, SS Main Blade

A comparison between the investigated cases shows the effect of the velocity difference at the inlet of the computational domain (which accords to the FRAP measurement plain in the RIGI test rig) on the pressure fluctuation on the main blade surface at 10% span:

case:	$\frac{\Delta V_{inlet}}{\overline{V_{inlet}}}$	$\frac{\Delta p'}{p_{0,\,rel,\,inlet}}$
13360 rpm	~ 0.40	~ 0.13
16250 rpm	~ 0.24	~ 0.14
17340 rpm	~ 0.19	~ 0.20
20700 rpm	~ 0.15	~ 0.22

The comparison is to handle with care due to the fact that all the parameters such as mass flow rate, pressure ratio, etc. vary for all the cases. An investigation at constant rotational speed with variable mass flow rate would be more meaningful.

5. Conclusions

The impeller grid used for the numerical investigation is of high quality. For future investigation one can think of a reduction of the number of nodes without a significant loss in quality of the results to accelerate the solver process and to reduce the amount of computational power. The detailed validation of the model on the base of steady state simulations showed good consistence with the test rig performance. The deviations in performance are of the order of 2% over the whole compressor map. The stationary computations showed good convergence rates and extremely low mass imbalances of the order of 10^{-6}. An additional stationary domain in the impeller model for the diffuser section would allow an amelioration of the convergence niveau by reducing numerical instabilities due to the small angles between relative flow direction and domain boundary in the present rotating diffuser exit. The comparison of the total pressure distribution at the exit of the impeller from hub to shroud with FRAP measurements confirmed the prediction of the CFD results. The vortical structure caused by tip leakage flow occurs stronger in the numerical solution than in the measurements. The reason might be an overprediction of total pressure loss in the CFD model or a underprediction in the FRAP measurements due to the highly fluctuating flow field at the exit of the impeller affecting accuracy of the FRAP results. The qualitative description of the flow pattern through the impeller for several operating points via relative and absolute Mach number provides information about the fluid dynamics within the centrifugal compressor. A main focus concentrates on the tip leakage vortex. The results show the trend to stronger vorticity with increased mass flow rate at constant blade speed. The comparison at constant mass flow rate but increased blade speed indicated a higher amount of tip leakage fluid of the main blade shroud gap passing the leading edge of the splitter blade. The vorticity in the inter blade channel therefore decreases with increased rotational speed at constant mass flow rate. The FRAP measurements in the distorted inlet flow field allowed the extraction of the turbulence intensity as additional inlet boundary condition profile for the CFD model. To get information about accuracy of the predicted turbulence intensity with FRAP probes a validation with alternative measurement techniques such as hot wire probes should be performed. The comparison of the results with implemented turbulence intensity profile at the inlet to the case with average turbulence intensity of 5% over the whole inlet of the model showed no significant change of the unsteady blade pressure distribution. Six time resolved cases at four different operating points were performed. The transient CFD simulations show good periodic convergence quantified via correlation of discrete nodes on the main blade surface monitoring unsteady blade pressure. The amount of computational power makes the unsteady solution process extremely time consuming. Due to the fact that the simulation of the entire impeller is needed the solver can only run in a parallel mode. At least four nodes on the Linux cluster are therefore necessary to handle the large model. The tracking of the distortion through the impeller provides a basic understanding of the interaction with the impeller blades. The spectral analysis of the unsteady pressure distribution on the main blade provides information about the dynamic load caused by the inlet distortion. The comparison between idealized total pressure profile as inlet boundary condition and the „real“ FRAP measured profile at exactly the same operating point showed good consistence and allows future investigation with idealized total pressure profiles which accelerates the setup of transient CFD solver input files.

6. Future Work

The steady state CFD results over the whole range of operating points provides a basis for future post processing of the huge amount of data. For further investigation one may reduce the number of grid points due to the fact that the y^+ values are not at the upper limit for the solver software in use to accelerate the process.
An additional stationary domain in the computational model for the diffuser section would reduce numerical instability caused by small angles between relative flow direction and domain boundary using a rotating frame of reference for the diffuser outlet.

The unsteady CFD investigation is done for only four operating points. It might be interesting to vary several parameters such as mass flow rate and pressure ratio but the whole procedure is extremely time consuming due to the large model and the relatively slow convergence rate of centrifugal compressor models.
The software used for the present work offers the possibility to couple the fluid model with the structure of the impeller. The implementation of a model containing the fluid- structure interaction may provide interesting and detailed knowledge about the excitation of the impeller blades due to inlet flow distortion. The resulting reaction of the impeller structure might be used to compare the strain gage measurements with the numerical model.
The unsteady pressure distribution on the blades of the CFD model allows a comparison with the planned pressure measurements on the main blades of the impeller in the test rig. The numerical results may simplify Albert Kammerers task to find a model for the forcing function of the blade vibrations.

The turbulence intensity measured with FRAP probes and used as inlet boundary condition in the CFD model has to be validated with other measurement techniques such as hot wires due to the fact that there is no indication about the accuracy the FRAP results.

7. References

Abhari, R.S., Prof. Dr., Lecture Notes *Aerospace Propulsion*, SS 2006 ETH Zurich

Abhari, R.S., Prof. Dr., Lecture Notes *Turbomachinery Design*, WS 2005/2006 ETH Zurich

Ainsworth, R.W., **Miller**, R.J., **Moss**, R.W., **Thorpe**, S.J., *Unsteady pressure measurement*, Measurement Science and Technology, Vol. 11, 2000

ANSYS Europe Ltd., *User Guide*, 2007

Ariga, I., **Kasai**, N., **Masuda**, S., **Watanabe**, I., **Watanabe**, Y., *The Effect of Inlet Distortion on the Performance Characteristics of a Centrifugal Compressor*, ASME paper No. 82-GT-92, 1982

Bosman, C., **Jadayel**, O.C., *A quantified study of rothalpy conservation in turbomachines*, Int. J. Heat and Fluid Flow, 17, No. 4, 410-17, 1996

Brouchkaert, J.F., **Sieverding**, C.H., **Manna**, M., *Development of a fast response 3- hole pressure probe*, The 14th Symposium on Measuring Techniques in Transonic and Supersonic Flows in Cascades and Turbomachines, Limerick, 1998

Came, P., *The development, application and experimental evaluation of a desing procedure for centrifugal compressors*, AGARD Conference Proc. No. 282, 1978

Came, P.M., **Herbert**, M.V., *Design and experimental performance of some high pressure ratio centrifugal compressors*, AGARD Conference Proc. No. 282, 1980

Campbell, W., *Protection of Steam Turbine Disk Wheels*. ASME paper 120, 1924

Clements, W.W., **Artt**, D.W., *The influence of diffuser channel length to width ratio on the efficiency of a centrifugal compressor*, Proc. Instn. Mech. Engrs, 202, No. A3, 163-9, 1988

Cumpsty, N. A., *Compressor Aerodynamics*, 2004

Dickmann, H.-P., **Secall Wimmel,** T., **Szwedowicz**, J., **Filsinger**, D., **Roduner**, C.H., *Unsteady Flow in a Turbocharger Centrifugal Compressor: Three- Dimensional Computational Fluid Dynamics Simulation and Numerical and Experimental Analysis of Impeller Blade Vibration*, ASME, 2006

Dixon, S.L., *Fluid Mechanics, Thermodynamics of Turbomachinery*, 1998

Emmons, H.W., **Kronauer**, R.E., **Rocket**, J.A., *A survey of stall propagation- experiment and theory*, ASME, Series D, 81, 1959

Engeda, A., **Kim**, Y., **Aungier**, R., **Direnzi**, G., *The Inlet Flow Structure of a Centrifugal Compressor Stage and its Influence on the Compressor Performance*, J. of Fluids Engineering, Vol. 125, 2003

Epstein, A.H., *High frequency response measurements in turbomachniery*, VKI Lecture Series, Rhode-Saint- Genèse, 1985

Gizzi, W.P., *Dynamische Korrekturen für schnelle Strömungssonden in hochfrequent fluktuierenden Strömungen*, PhD Thesis ETH Nr. 13482, 2000

Gorla, R.S.R., **Khan**, A.A., *Turbomachinery Design and Theory*, 2003

Gossweiler, C., *On Probes and Measuring Techniques for Fast- Response Flow Measurement Using Piezo- Resistive Pressure Transducers*, PhD Thesis ETH Nr. 10253, 1993

Greitzer, E.M., **Nikkanen**, J.P., **Haddad**, D.E., **Mazzawy**, R.S., **Joslyn**, H.D., *A fundamental criterion for the application of rotor casing treatment*, J. Fluid Eng., 101, 204-262, 1979

Greitzer, E.M., **Tan**, C.S., **Graf**, M.B., *Internal Flows - Concepts and Applications*, 2004

Grotjans, H., **Menter**, F.R., *Wall functions for general application CFD codes*, 1998

Horlock, J.H., *Axial Flow Compressors,* 1958

Kerrebrock, J.L., *Aircraft Engines and Gas Turbines*, 1992

Kleiser, L., Lecture Notes *Turbulent Flows*, WS 2005/2006 ETH Zurich

Kupferschmied, P., **Köppel**, P., **Gizzi**, W.P., **Gyarmathy**, G., *Time- resolved flow measurements with fast-response aerodynamic probes in turbomachines*, Measurement Science an Technology, Vol. 11, Issue 7, Article 318, 2000

Launder, B.E., **Spalding**, D.B., *The numerical computation of turbulent flows*, 1974

Lymann, F.A., *On the conservation of rothalpy in turbomachines*, J. of Turbomachinery, 115, 520-6, 1993

Moore, J. , **Moore**, J.G., **Timmis**, P.H., *Performance evaluation of centrifugal compressor impellers using three- dimensional viscous flow calculations*, J. Eng. Gas. Turbines Power, 106, 475-81, 1984

Pfau, A., **Schlienger**, J., **Kalfas**, A.I., **Abhari**, R.S., *Introducing the New Virtual Four Sensor Fast Response Aerodynamic Probe (FRAP)*, The 16th Symposium on Measuring Techniques in Cascades and Turbomachines, Cambridge, Sept. 2002

Pfau, A., **Schlienger**, J., **Kalfas**, A.I., **Abhari**, R.S., *Unsteady, 3-dimensional Flow Measurements Using a Miniature Virtual 4- sensor Fast Response Aerodynamic Probe (FRAP)*, Draft for Proceedings of ASME Turbo Expo, 16-19 June 2003, Atlanta, Georgia

Porreca, L., **Hollenstein**, M., **Kalfas**, A.I., **Abhari**, R.S., *Turbulence Measurements and Analysis in a Multistage Axial Turbine*, 2006

Rodgers, C., **Sapiro**, L., *Design considerations for high pressure ratio centrifugal compressors*, ASME 72-GT-91, 1972

Schleer, M., **Mokulys**, T., **Abhari**, R.S., *Design of a high pressure- ratio centrifugal compressor for studying Reynolds number effects*, IMechE London, 2003

Schleer, M., PhD Thesis, *Flow Structure and Stability of a Turbocharger Centrifugal Compressor*, 2006

Senoo, Y., **Kita**, Y., **Ookuma**, K., *Measruement of two dimensional periodic flow with a cobra probe*, J. Fluids Engineering, p295, 1973

Smith, G.D.J., **Cumpsty**, N.A., *Flow phenomena in compressor casing treatment*, J. Eng. Gas Turbines and Power, 106, 532-41, 1984

Withfield, A., **Baines**, N.C., *Design of Radial Turbomachines*, 1990